OXIDATIVE PRESSURE LEACHING OF CHALCOCITE BY INCO Ltd.'s

SECOND STAGE LEACH PROCESS

by

BENJAMIN R. SAITO

B.A.Sc., The University of British Columbia, 1991

A THESIS SUBMITTED IN PARTIAL FULFILLMENT OF

THE REQUIREMENTS FOR THE DEGREE OF

MASTER OF APPLIED SCIENCE

in

THE FACULTY OF GRADUATE STUDIES

(Department of Metals and Materials Engineering)

We accept this thesis as conforming
to the required standard

THE UNIVERSITY OF BRITISH COLUMBIA
August 1995
© Benjamin R. Saito

In presenting this thesis in partial fulfilment of the requirements for an advanced degree at the University of British Columbia, I agree that the Library shall make it freely available for reference and study. I further agree that permission for extensive copying of this thesis for scholarly purposes may be granted by the head of my department or by his or her representatives. It is understood that copying or publication of this thesis for financial gain shall not be allowed without my written permission.

Department of _Metals & Materials Eng._

The University of British Columbia
Vancouver, Canada

Date _AuGust 29, 1995_

DE-6 (2/88)

Abstract

The INCO Ltd. Copper Refinery Electrowinning Department (CRED) in Copper Cliff, Ontario, Canada, processes a Cu, Ni, Co, Fe, As, S and precious metals containing residue produced by the INCO Pressure Carbonyl (IPC) plant. This residue is treated in two successive leaching stages. The First Stage batch leach extracts most of the Ni, Co, Fe and As. During the Second Stage batch leach process, the oxidative pressure leaching of a predominantly Cu_2S feed is effected under acid deficient conditions. The main process objective is to preferentially extract the copper, leaving behind a residue rich in precious metals. Several physico-chemical parameters hinder the copper extraction by limiting oxygen mass transfer. Part I of this investigation focuses specifically on the impact of temperature and total arsenic content.

Laboratory experiments were conducted at temperatures ranging from 100 to 135°C with different plant feed solids having arsenic concentrations ranging from 0.37 to 1.4 wt.%. Additional tests were performed with controlled arsenic additions to the feed electrolyte. The results showed that conditions of high temperature and high arsenic were detrimental to overall copper extraction rates. Suppression of leach kinetics was attributed to the formation of high viscosity basic copper sulphate slurries which inhibited oxygen mass transfer. High viscosity slurries resulted from the preferred precipitation of sub-micron acicular basic copper sulphate crystals over large platelet-shaped crystals. The observed effects were believed attributable to two main factors: elevated supersaturation levels from increased initial rates of chalcocite leaching, and the formation of a heterogeneous nucleation substrate, possibly, basic copper arsenate, $Cu_2AsO_4(OH)$.

In part II of this investigation, the oxygen mass transfer/mixing performance of the Second Stage leach process was examined. This was done in scaled-model tests (125 L). Improvements in surface aeration rates through changing impeller systems were sought. Results from the scaled model tests showed that converting from the current dual axial down-draft impeller system to a radial disk impeller system resulted in improvements in mass transfer rates by as high as 200% at 221 rpm. For a dual radial disk system, mass transfer rate increases came at the expense of significantly higher power draw. For a radial(top)/axial system, high mass transfer rates were achieved with only marginal power draw increase. Fill level sensitivity tests revealed that the axial impeller system was

most sensitive to overfilling, resulting in near zero mass-transfer rates from only a +5% increase in fill height above the scaled normal fill height. Similar decreases in mass-transfer rates for both radial impeller systems came after +10% increase. Based on the test-work performed, the radial/axial system was judged to be the most successful in overall k_La and power draw performance.

The internal cooling coil system was found to offer a partial baffling effect, sufficient to prevent gross swirling yet low enough prevent central vortex collapse. This condition was believed to be critical in achieving high gas-liquid mass transfer performance in the scaled model.

Table of Contents

Part II: Gas-Liquid Mass Transfer and Mixing Studies in a Scaled Model of the Second Stage Leach Autoclave

List of Figures

List of Tables

List of Symbols and Abbreviations used in Part I

Symbols

A	-	Surface area	(m^2)
a	-	Specific interfacial area	(m^{-1})
a_i	-	Activity of species i	-----
$C_p{}^o$	-	Constant pressure standard heat capacity	$(J\text{-}mol^{-1}K^{-1})$
d_n	-	Distance from crystal face to centre	(m)
ΔG	-	Gibbs free energy change	(J)
ΔG^*	-	Free energy of a particle of critical nucleus size (nucleation activation energy)	(J)
ΔG_S	-	Gibbs free energy change - surface area creation contribution	(J)
ΔG_V	-	Gibbs free energy change - volume creation contribution	(J)
ΔG_v	-	Gibbs free energy change - per unit volume created	$(J\text{-}m^{-3})$
$\Delta G^o{}_f$	-	Standard Gibbs free energy of formation	$(J\text{-}mol^{-1})$
J	-	Nucleation rate	$(mol\text{-}s^{-1})$
K, K'	-	General constants	-----
K_{eq}	-	Equilibrium constant	-----
K_{sp}	-	Solubility product	-----
P	-	Pressure	(atm)
R	-	Gas constant (8.314)	$(J\text{-}mol^{-1}K^{-1})$
r	-	Particle radius	(m)
r^*	-	Critical nucleus size	(m)
S_s	-	Supersaturation	-----
S^o	-	Standard entropy	$(J\text{-}mol^{-1}K^{-1})$
$\overline{V}$	-	Molar volume	$(m^3\text{-}mol^{-1})$
T	-	Temperature	(K)
Z	-	Sign and magnitude of charge on species	-----

Abbreviations

BCAs - Basic copper arsenate

BCS - Basic copper sulfate

IAP - Ion activity product

PGM - Platinum group metals

PM - Precious metals

SHE - Standard hydrogen electrode

Greek symbols

ξ - Number of ions per formula unit

γ - Interfacial tension   *(N-m^{-1})*

Φ - Heterogeneous nucleation catalysis factor

θ - Interfacial contact angle

Subscripts

c - crystal

l - liquid

s - substrate

hom - homogeneous

het - heterogeneous

List of Symbols and Abbreviations used in Part II

Symbols

a	-	Specific gas-liquid interfacial area	(m^{-1})
B	-	Baffle width	(m)
C	-	Impeller clearance from tank bottom	(m)
C_i^*	-	Concentration of i at interface	$(mol\text{-}m^{-3})$
C_i^b	-	Concentration of i in bulk	$(mol\text{-}m^{-3})$
C_i	-	Concentration of species i	$(mol\text{-}m^{-3})$
D	-	Impeller diameter	(m)
D_A	-	Diffusivity of species A	$(m^2\text{-}s^{-1})$
d_B	-	Bubble diameter	(m)
g	-	Gravitational constant	$(m\text{-}s^{-2})$
H	-	Velocity head	$(m^2\text{-}s^{-2})$
H_I	-	Liquid height above impeller	(m)
K_G	-	Mass transfer parameter (equivalent to $k_L a$)	(s^{-1})
k	-	Mass transfer coefficient	$(m\text{-}s^{-1})$
k_L	-	Liquid phase mass transfer coefficient	$(m\text{-}s^{-1})$
N	-	Impeller rotational speed	(s^{-1}) or (rpm)
N_C	-	Critical impeller speed for surface aeration	(s^{-1})
N_{CD}	-	Critical impeller speed for complete gas dispersion	(s^{-1})
N_R	-	Critical impeller speed for gas recirculation	(s^{-1})
P_{O2}		Partial pressure of oxygen	(atm)
P'	-	Dimensionless quantity	-----
Q	-	Liquid flow rate	$(m^3\text{-}s^{-1})$
Q_G	-	Gas flow rate	$(m^3\text{-}s^{-1})$
$R_i, \dot{n}$	-	Mass transfer flux	$(mol\text{-}m^{-3}s^{-1})$
S	-	Inter-impeller separation distance (multiple impeller system)	(m)

s	-	Fractional rate of surface renewal	(s^{-1})
T	-	Tank diameter	(m)
Tq	-	Torque	$(N\text{-}m)$
v	-	Impeller tip speed	$(m\text{-}s^{-1})$
Z	-	Liquid height above tank bottom	(m)

Abbreviations

AD	-	4-bladed 45° axial down-draft impeller system	
ME	-	Mole O_2 - energy ratio	$(mol\text{-}J^{-1})$
RA	-	Radial disk(top) - axial down-draft impeller system	
RR	-	Dual 6-bladed radial disk impeller system	
CC	-	Autoclave model configuration (cooling coils)	
UB	-	Unbaffled tank configuration	
4B	-	Standard 4 vertical baffled tank configuration	

Greek Symbols

α	-	Impeller efficiency factor for surface aeration	----
δ	-	Film layer thickness	(m)
μ	-	Dynamic viscosity	$(kg\text{-}m^{-1}s^{-1})$
Π	-	General proportionality constant	----
ρ	-	Density	$(kg\text{-}m^{-3})$
σ	-	Gas-liquid interfacial tension	$(N\text{-}m^{-1})$
τ	-	Shear stress	$(kg\text{-}m^{-1}\text{-}s^{-2})$
θ	-	Exposure time period in penetration theory	(s)
ε_G	-	Gas holdup	----
ω	-	Angular velocity	$(rad\text{-}s^{-1})$

Dimensionless Groups

N_{Fr} - Froude number $\qquad \left(\dfrac{N^2 D}{g} \right)$

N_H - Velocity head number $\qquad \left(\dfrac{N_P}{N_Q} \right)$

N_P - Power number $\qquad \left(\dfrac{P}{N^3 D^5 \rho} \right)$

N_Q - Flow number $\qquad \left(\dfrac{Q}{N D^3} \right)$

N_{Re} - Reynold's number $\qquad \left(\dfrac{N D^2 \rho}{\mu} \right)$

N_{We} - Weber number $\qquad \left(\dfrac{N^2 D^3 \rho}{\sigma} \right)$

Ha - Hatta number $\qquad \dfrac{1}{k_L} \sqrt{ \dfrac{2}{m+1} K_{mn} D_A C_A^{m-1} C_B^n }$

Acknowledgements

There are so many people that I would like to thank for providing me with the resources needed to complete this thesis. First and foremost, I would like to thank my family for everything they have done for me. I cannot describe the amount of support I have received from them. I would also like to thank the students, faculty and staff of the MMAT department of UBC for their support, ideas and above all else, friendship. Special thanks to all my Hydromet pals for their consulting advice on both professional and personal matters and above all, the comic relief that they have provided. You have made it a pleasure for me to come in, day-in and day-out.

I would like to thank INCO Ltd. for sponsoring this research and I am especially grateful to Dr. Eberhard Krause, Norm Nissen and Paula Tyroler for all their input into this project. I would also like to thank the technical staff at both Copper Cliff and J. Roy Gordon research laboratories for their excellent analytical work.

I have saved mention to last, the three people to whom I am most grateful. I would like to thank Ish Grewal for his invaluable help in starting the ball rolling. I would also like to thank Chantal Clément of INCO who was to me, a supervisor, a co-worker and most importantly, a good friend. Lastly, my supervisor, Dr. David Dreisinger, who has provided me with academic, financial and moral support for as long as I have known him. You have shown me more patience and understanding than any student deserves and, definitely, can ever hope to receive. It is you that I thank the most.

Chapter 1

Introduction

In the recovery of metallic values from sulfide sources, pyrometallurgical or hydrometallurgical process routes are available. Pyrometallurgical routes have historically been preferred owing to faster process kinetics, higher production capacities and lower production costs. However, global enforcement of increasingly strict environmental regulations regarding sulfur dioxide and metal vapour emissions are negating such benefits. In addition, the treatment of low grade and complex ores as well as from secondary metal resources such as mattes have not proven feasible using conventional pyrometallurgical practices. Pyrometallurgical processes are also largely unspecific, often making separation of individual metals from a system of chemically similar species very difficult. Hydrometallurgical routes can offer superior selectivity and greater versatility in ore and concentrate treatment. Hydrometallurgical processes do not produce atmospheric pollution, particularly with respect to low grade or "dirty" concentrates. As the science and technology of hydrometallurgical processes advances, hydrometallurgical methods of metal extraction is certain to become more widespread in use, and perhaps replace pyrometallurgy in some fields. Recent examples of technology succession in the metallurgical industry include the start-up of the world's first hydrometallurgical plant for zinc extraction (1980 - Cominco Ltd., Trail, BC), based on Sherritt's zinc pressure leach process [1], and the increased practice of biological heap leaching in the recovery of copper from sulfide ores in Chile [2].

1.1 Oxidative Pressure Leaching of Metal Sulfides

"Oxidative pressure leaching" is the branch of hydrometallurgical processes which effects the extraction of metallic values using an oxidizing gas at elevated pressures. Because of the elevated pressures, operation at temperatures exceeding the normal boiling point of aqueous solutions are frequently encountered. This enables the synergistic benefits of high temperatures and reactant gas partial pressures on extraction kinetics to be exploited. From reaction rate theory, a $10°C$ increase in reaction temperature results in a near two-fold increase in conversion rate for an activation controlled process. Moreover, increasing the gas partial pressure increases the reaction rate by the same factor for a first-order reaction. As a result, reactor size may be downsized

substantially while still achieving desired throughput rates. The leaching of some refractory sulfides that would not be economically feasible due to immeasurably slow extraction rates or thermodynamic constraints under ambient conditions may, therefore, be profitably treated through elevated pressure leaching operations. Another advantage, encountered in the oxidative pressure leaching of Cu_2S or ZnS feeds with sulfuric acid, is the ability to select the degree of sulfur oxidation by proper choice of process conditions. Thus, oxidative pressure leaching can oxidize sulfide sulfur to elemental sulfur or sulfate.

For oxidative pressure leaching processes, the oxidizing gas is continually consumed in the leach reaction. Therefore, a continuous supply of gas into the slurry system is needed to maintain the necessary oxidizing potentials to effectively sustain desired leach kinetics. Because of the high temperatures involved, reaction kinetics are generally fast and oxygen consumption rates are high. This is true for most sulfide mineral leaching operations, especially total sulfur oxidation (to sulfate) processes where the stoichiometric requirement is extremely high (2 tonnes of O_2 per tonne S oxidized). Consumption rates as high as 35 g-mole-min^{-1}m^{-3} have been observed in some industrial processes. At such high rates, oxidation mass transfer is often rate controlling and optimization of gas-liquid mass transfer performance is crucial for process objectives.

Peters [3] has offered the following four general mechanisms to describe oxidative leach processes using oxygen gas. These are described briefly below and illustrated in Figure 1.1.

1. Oxygen introduced in gaseous form, dissolves, and directly reacts with the particle at the particle-solution interface (Figure 1.1a).

2. Dissolved oxygen reacts homogeneously with an aqueous reduced species (R) which results in the formation of a *surrogate oxidant* species (R$^+$) which then effects the oxidation process at the mineral surface (Figure 1.1b). If high concentrations of the reduced (and thus surrogate oxidant) species are present significant increases in leaching rates may be incurred. This is the mechanism describing ferric-ferrous leaching systems, such as Cominco Ltd.'s Zinc Pressure Leach process [4].

3. Oxygen reacts at the gas-liquid interface with a reducing agent formed from the mineral leaching process to form a surrogate oxidant which then reacts with the mineral (Figure 1.1c). This

is a possible model for the Arbiter ammonia leach for the treatment of copper concentrates [5] in which the reduced species is the cuprous-ammine complex, $Cu(NH_3)_2^+$ and the surrogate oxidant is the cupric-ammine species, $Cu(NH_3)_2^{2+}$.

4. Oxygen reacts in the gas phase to generate a gaseous surrogate oxidant species that has a higher solubility than oxygen (Figure 1.1d). This mechanism has been proposed by Peters [3] to account for the nitric acid catalysis of the oxygen pressure leaching of *pyrite* (FeS_2) and *arsenopyrite* (FeAsS) feeds. Nitric acid is consumed to produce reduced N-O species which are re-oxidized by oxygen to regenerate a soluble oxidant (probably *nitrosyl*, NO^+).
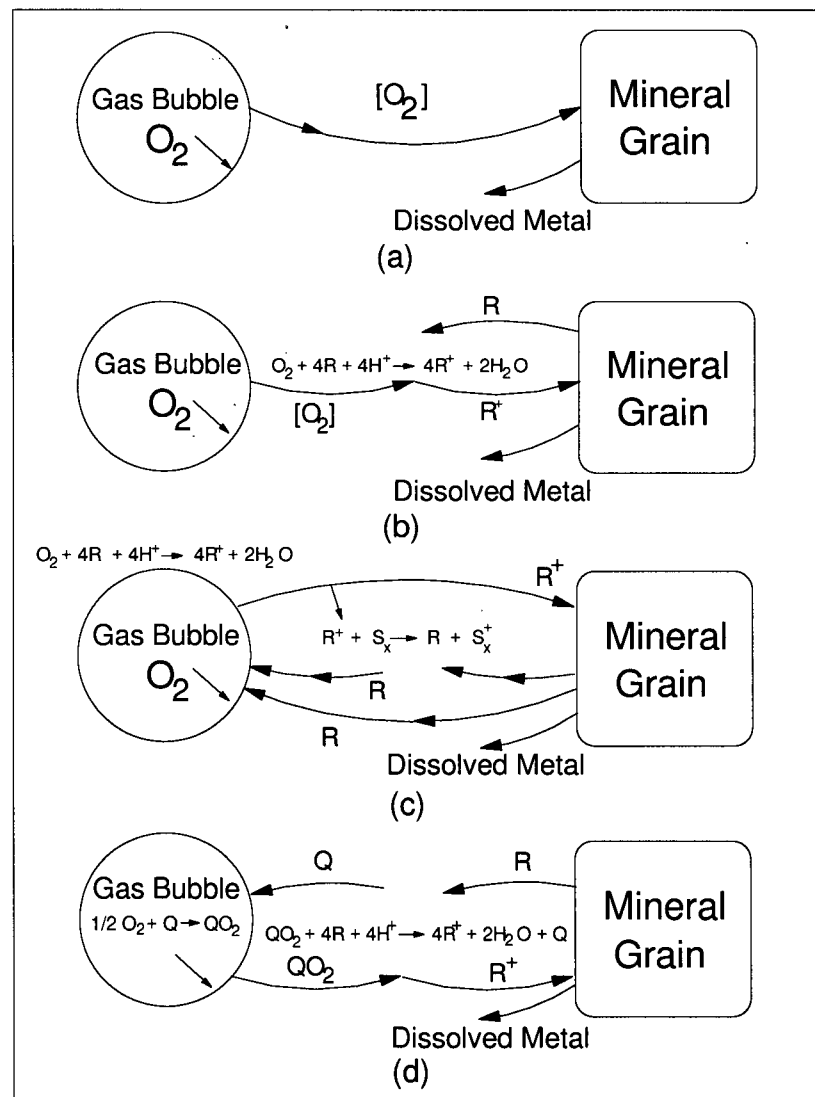
Figure 1.1   Models for oxygen absorption during oxidative leaching processes [3].

An industrial operation which practices oxidative pressure leaching is INCO Ltd's Second Stage leach process. In this process, copper is leached from a copper sulfide residue under conditions of total sulfur oxidation. This thesis examines aspects of the Second Stage leach process kinetics and is divided into two parts. Part I investigates the impact of physico-chemical variables on leach behaviour. Specifically the effect of leach temperature and feed arsenic concentration will be studied. Part II investigates the gas-liquid mass transfer and mixing characteristics of the Second Stage leach process. Each part is divided into 3 main chapters: 1) Literature Review; 2) Experimental Method and 3) Results and Discussion. Research objectives are discussed at the beginning of the Experimental Methods chapters. Conclusions and industrial significance of this work are presented at the end of the Result and Discussion chapters. The final section of this document will summarize the work done in both parts of the investigation and offer recommendations for further work.

PART I:

Effect of Temperature and Feed Arsenic Content on Leaching Behaviour

Chapter 2

Background and Literature Review

2.1   Overview of CRED Operations

INCO Ltd.'s Copper Refinery Electrowinning Department (CRED) in Copper Cliff, Ontario, is a hydrometallurgical operation which processes copper-rich sulfidic residues produced by the INCO Pressure Carbonyl (IPC) process. The residue contains: 55-60 wt.% Cu (predominantly Cu_2S), 9-12 wt.% Ni, 6-8 wt.% Co, 3-5 wt.% Fe, 0.5-2 wt.% As, and 45-75 oz/ton precious metals (platinum group metals, Au and Ag). Two successive batch leach unit operations extract the base metals, leaving behind a residue rich in precious metals. A simplified flowsheet for the operations is illustrated in Figure 2.1 and described briefly below. A detailed description of the CRED flowsheet is provided by Tyroler et al. [6].
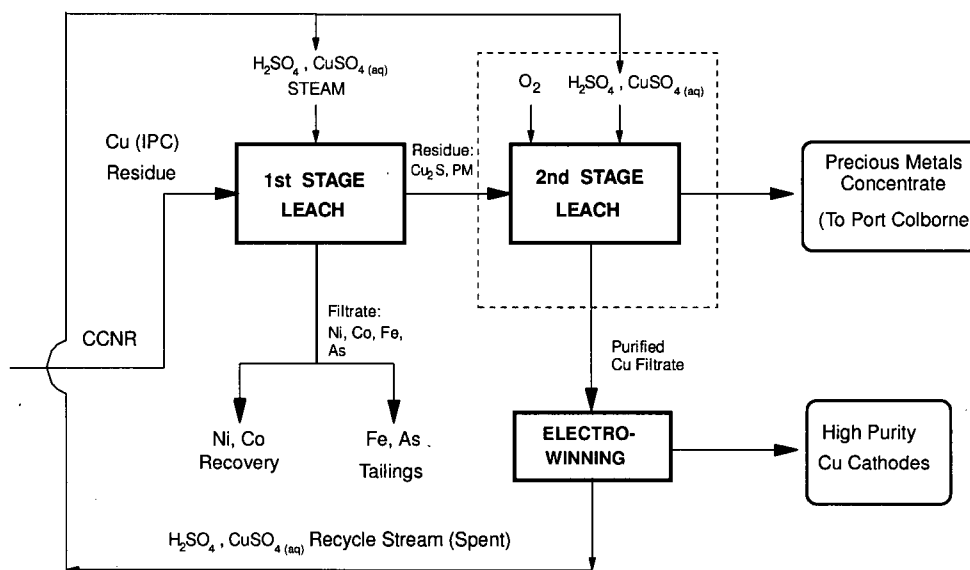
Figure 2.1   Simplified flowsheet of INCO CRED operations.

In the First Stage leach, nickel, cobalt, iron and arsenic are selectively extracted over copper and precious metals, down to a combined level of less than 4 wt.%. The leach operates under metathetic conditions at a temperature and steam pressure of 160°C and 593 kPa (86 psig) respectively. Diluted spent copper electrolyte (containing approximately 150 g/L H_2SO_4, and 30 g/L Cu) serves as lixiviant. The extracted Ni and Co values are recovered as carbonates; the Fe and As are co-precipitated with gypsum to produce an environmentally stable gypsum-ferric hydroxide-ferric arsenate precipitate which is sent to a tailings pond. The resulting residue provides the feed for the second leaching process.

In the Second Stage leach, copper is extracted through pressure oxidation with oxygen, leaving a residue rich in precious metals. The leach is carried out in diluted recycled spent copper electrolyte. The leach operates at a temperature of 115°C and a total gauge pressure of 1034 kPa (150 psig) including 966 kPa (140.2 psig) O_2. Acid deficient conditions are employed which results in the total oxidation of sulfide to sulfate, eliminating elemental sulfur production. Consequently copper precipitates from solution in the early stages of the leach as the basic copper sulfate species (BCS), *antlerite*, $CuSO_4 \cdot 2Cu(OH)_2$, buffering the solution pH between 2 and 3. Thereafter, leaching proceeds in the presence of these precipitates until completion. To complete copper extraction, the slurry is subjected to a BCS redissolution stage by the addition of a mixed spent electrolyte and fresh concentrated sulfuric acid solution. The result is a pregnant copper solution and a precious metals residue. After purification to remove selenium and tellurium, the pregnant liquor is electrowon to produce high purity cathodes and the precious metals concentrate is sent for refining at the Port Colborne Refinery.

The Second Stage leach is the final stage of the base metal-precious metals separation process. The success of the leach operation is critical not only for the recovery of copper but also, for the refining of the high valued precious metals content.

2.1.1   Current Operating Parameters of the Second Stage Leach

The Second Stage leach is carried out in one of two plain carbon-steel autoclaves lined with 316 stainless steel. The maximum capacity of each vessel is 38 000 L. A schematic representation of the autoclave system is shown in Figure 2.2.

Manway

Oxygen
Inlet

Fill Level

3.5

2.5

1.9

Cooling
Coil

1.0

0.80

1.75

Dimensions in m
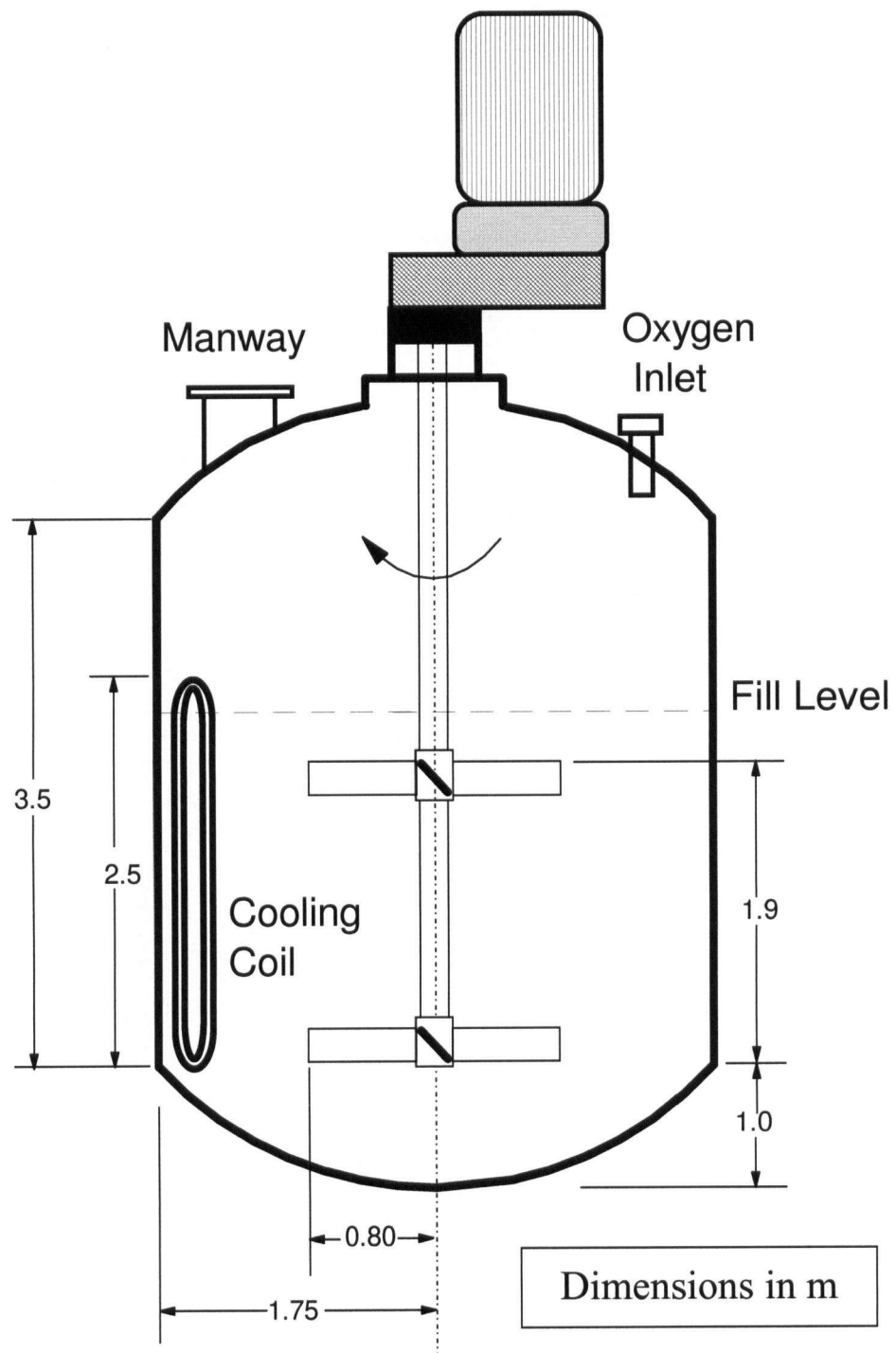
Figure 2.2   The Second Stage leach autoclave.

The feed charge is comprised of 25-30 wt.% First Stage residue with the balance being diluted spent electrolyte. The First Stage residue contains: 70-75 wt.% Cu, 15-20 wt.% S, 4 wt.% (Ni + Co + Fe + As) and trace precious metals. The diluted spent electrolyte contains: 20-30 g/L Cu, 90 g/L H_2SO_4, 2-3 g/L Fe, 1-2 g/L As. The charge is prepared in a batch make-up tank prior to introduction to the Second Stage autoclave. After preparation, the feed slurry is pumped into the Second Stage autoclave to an operating volume of approximately 30 000 L. The initial temperature of the slurry is roughly 70°C. Oxygen gas is top blown into the vessel until pressurized. The operating temperature of 115°C is achieved through the heat generated by the highly exothermic total oxidative leaching process. Temperature control is achieved thereafter by cooling water regulation through a double-meandering cooling coil system located inside the autoclave.

The oxygen demand of the leach is provided solely by impeller incorporation of plenum oxygen gas into the slurry. Oxygen sparging is not currently practiced. The impeller system employed is a 45° pitched down-draft system operating at 68 rpm.

2.2 Difficulties in the Second Stage Leach Process - Extended Leach Behaviour

The Second Stage leach has been operating under current conditions since 1975. It has been found that the process is usually completed within 4-6 hours for acceptable copper extraction yields (> 97%). Approximately 20% of plant leaches require extended reactor residence times, from 8 to 20 hours. Several collaborative INCO-UBC investigations have focussed on improving leach conditions.

2.2.1 Investigation of Reaction Pathway and Leaching Kinetics

Grewal et al.[7] (paper based on Grewal [8]) investigated the reaction pathway and kinetics of the Second Stage leach process by performing a series of interruptive leach experiments on the laboratory scale. A 2L Parr titanium autoclave was used. X-Ray diffraction was used to identify solid products of the leach.

2.2.1.1 Reaction Pathway

Under typical plant conditions, the reaction pathway was found to follow the general mechanisms described by reactions 2.1 to 2.3, essentially in sequential order. The fourth reaction

occurred out of sequence, but only to a minor extent. The reactions were originally proposed in a preliminary model of the leach process by Dreisinger and Peters [9].

1. Chalcocite leaching in the presence of acid, copper sulfate

$$Cu_xS_{(s)} + (x-1)H_2SO_4 + \frac{1}{2}(x-1)O_2 \rightleftharpoons CuS_{(s)} + (x-1)CuSO_{4(aq)} + (x-1)H_2O \qquad (2.1)$$
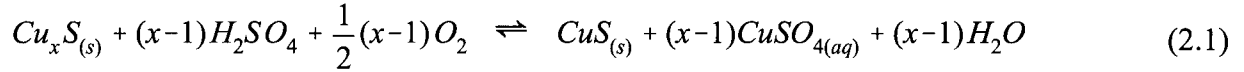
2. Chalcocite leaching after acid depletion, antlerite precipitation

$$Cu_xS_{(s)} + \frac{3}{2}(x-1)O_2 + (x-1)H_2O \rightleftharpoons \frac{1}{2}(3-x)CuS_{(s)} + \frac{1}{2}(x-1)(CuSO_4 \cdot 2Cu(OH)_2)_{(s)} \qquad (2.2)$$
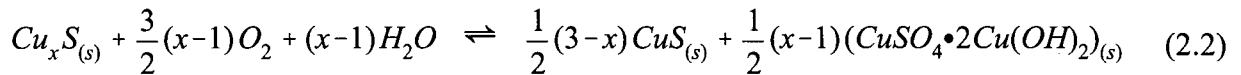
3. Covellite leaching after acid depletion

$$CuS_{(s)} + 2O_2 \rightleftharpoons CuSO_{4(aq)} \qquad (2.3)$$

4. Covellite leaching in the presence of excess acid

$$CuS_{(s)} + H_2SO_4 + \frac{1}{2}O_2 \rightleftharpoons CuSO_{4(aq)} + H_2O + S^\circ \qquad (2.4)$$
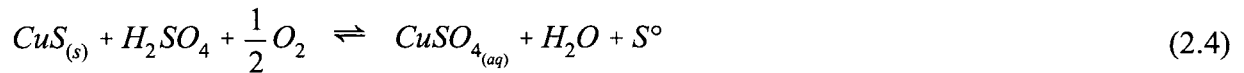
In the above, x refers to the average molar ratio of Cu:S in the initial solids and is typically close to 2 indicative of a predominantly chalcocite feed.

As shown in Figure 2.3, chalcocite to covellite conversion (50% copper leaching, 200 g Cu in solids) required only 20% of the total oxygen consumption. This was expected based on the $Cu:O_2$ stoichiometry shown in reactions 2.1 and 2.3. Covellite leaching was responsible for the remaining 80% of the total oxygen consumption. Basic copper sulfate precipitation (rxn. 2.2) occurred during the initial stages of chalcocite-covellite conversion, between 5 and 20% oxygen consumption. The end point of BCS precipitation coincided with the onset of covellite leaching which is a non-acid consuming copper leach reaction.
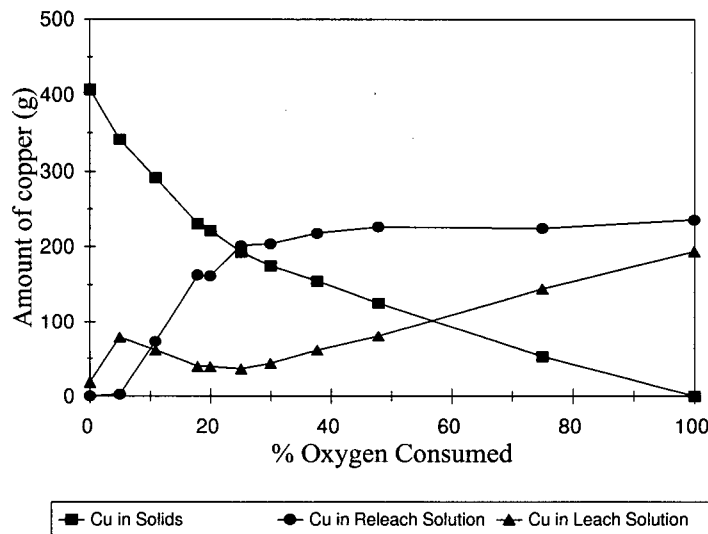
Figure 2.3   Distribution of copper in the leach products as a function of oxygen consumption [7].

2.2.1.2 Reaction Kinetics

It was determined that chalcocite to covellite leaching and basic copper sulfate precipitation (rxns. 2.1 & 2.2) were completed within the first 30 minutes of leaching. Covellite leaching (rxn. 2.3) was slower, yet full conversion was still completed in roughly four hours. All individual reaction mechanisms involved in the leach were, therefore, found to be not rate limiting. It was concluded that extended leach behaviour was not caused by a chemical reaction control mechanism under existing operating conditions.

A leach without iron present in the electrolyte was also performed. Since iron in the feed solids was very low-only 0.08 wt.%, the total feed iron concentration was near-zero. It was found that a reduction in the oxygen consumption rate occurred beyond 15% of total consumption. Leach kinetic sensitivity to agitation rate was also noticed. Slurry viscosity was observed to be higher than in leaches containing iron in the electrolyte. Unfortunately, no quantitative viscosity information was given. Copper extraction decreased from nearly 100% down to 96.7%, after 6 hours of leaching, which is just below the acceptable level. Finer sized BCS precipitates were produced from this leach. Based on these observations, a gas-liquid mass-transfer rate controlling mechanism was proposed. However, no reasonable explanation of this phenomena was offered.

Since iron-containing recycled spent electrolyte is used as lixiviant in the Second Stage leach process, the absence of iron represented an unrealistic condition in plant practice. Therefore, iron absence was not considered to be the principal cause of extended leach behaviour. However, similar observations of high viscosity slurry association with extended leach occurrence during plant operations, supported the proposed gas-liquid mass transfer rate-controlling mechanism.

2.2.2 The Effect of BCS Morphology and Viscosity on Leaching

Clément et al.[10] examined causes of gas-liquid mass transfer limitations and established a linkage between the physico-chemical variables of feed solids composition, slurry viscosity and copper extraction rate. First Stage residues having high Cu:S ratios or high arsenic contents were observed to yield high viscosity slurries and require longer leach times. Specifically, residues with Cu:S ratios in excess of 5.0[1] (weight basis) and arsenic contents above 0.9 wt.% were characteristic of problematic feeds. The classification of Cu:S ratios and arsenic contents of First Stage residues are presented below:

Table 2.1 - Classification of Cu:S and arsenic levels in Second Stage feed solids [10]

Classification[†]	Cu:S Ratio (wt:wt)	Arsenic content (wt.%)
Low	< 4.0	<0.5
Medium	4.2-4.6	0.5-0.9
High	> 5.0	> 0.9

[†]Cu:S ratios from 4.0-4.6 and arsenic levels below 0.9 wt.% are deemed as typical feed compositions.

2.2.2.1 Effect of Cu:S ratio

High Cu:S ratio First Stage residues originate from excessive sulfur removal in the converting process at the Copper Cliff Nickel Refinery. This is not a common occurrence; therefore, to perform a systematic study, First Stage residues were spiked to the desired Cu:S ratios with

---

[1] The Cu:S ratio for stoichiometric Cu_2S is 3.96 (weight basis)

elemental copper prior to oxidative leaching. Cu:S ratios ranging from 3.8 to 6.0 were obtained in this manner.

Figure 2.4(a) shows that increasing Cu:S ratios of the feed solids resulted in increased viscosity of the resulting basic copper sulfate slurry. The amount of basic copper sulfate precipitated was found to be directly related to the Cu:S ratio of the initial feed. Very little change in BCS precipitate morphology with Cu:S ratio was observed. Therefore, it was evident that the increase in viscosity was attributed to higher BCS concentration and not particle morphology factors in this case. As shown in Figure 2.4(b), the leaching of higher Cu:S ratio feeds resulted in poorer extraction rates which was attributed to decreased oxygen mass transfer rates.

As ≤ 0.5 wt. %   As ≤ 0.5 wt.%
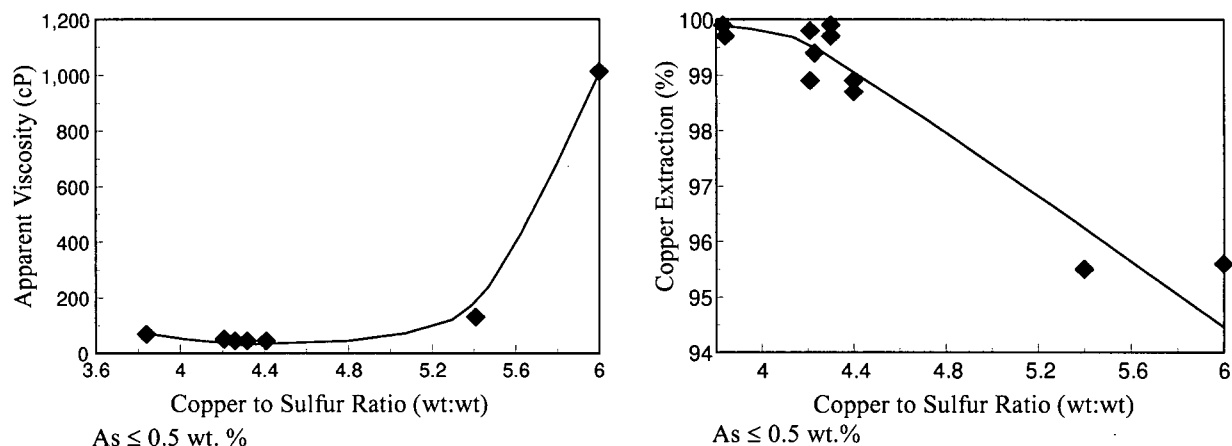
(a) Slurry viscosity as a function of Cu:S   (b) Copper extraction as a function of Cu:S

Figure 2.4   The effect of Cu:S ratio on Second Stage leach characteristics [10].

2.2.2.2 Effect of Arsenic

Over 70% of First Stage residues having greater than 0.9 wt.% arsenic have been observed to exhibit long leach behaviour [10]. High arsenic feed solids originate from one of two deficiencies during First Stage leach operation: 1) leach liquor copper depletion and 2) incomplete IPC residue leaching due to insufficient batch residence times or due to acid deficiency. Copper depletion results in a change in system oxidation potential which causes a reprecipitation of leached arsenic. This is the more common source of high arsenic feed solids. Incomplete First Stage leaching results in

higher values of unleached arsenic, along with elevated values of unleached nickel, cobalt and iron. The third source of arsenic in the Second Stage leach circuit is recycled spent electrolyte used as leach lixiviant. Approximately 1-2 g/L in the diluted spent electrolyte feed originates from arsenic extracted during previous Second Stage batch leaching operations.

Clément et al.[10] investigated the effect of feed solids arsenic by leaching residues having arsenic levels between 0.36 to 1.6 wt.%, with minimal variation of Cu:S ratio (4.0 to 4.4). Leach experiments were performed on the laboratory-scale (Parr 2L autoclave). Figure 2.5 shows an inverse relationship between arsenic level and copper extraction for leaching at 115°C at 600 rpm agitation rate.
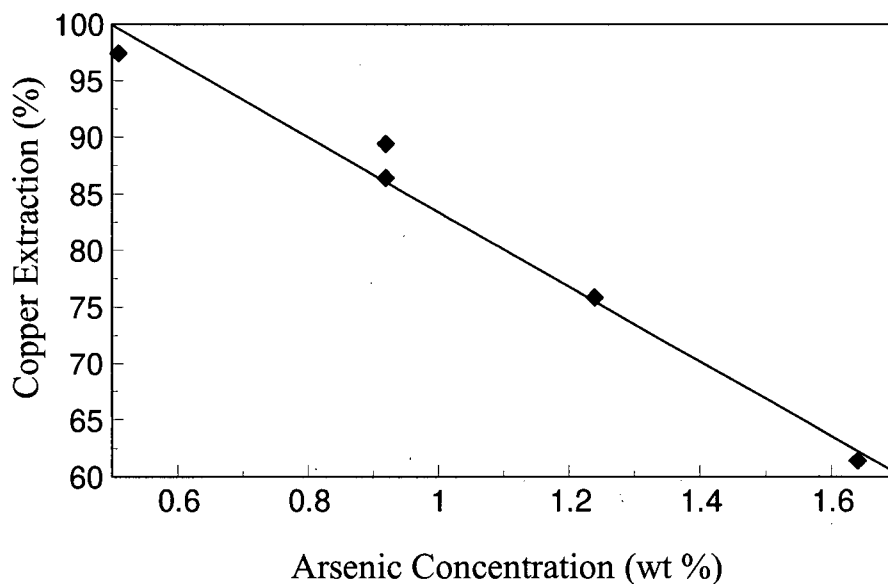
Figure 2.5   The effect of feed solids arsenic content on copper extractions at 600 rpm [10].

Morphology examination of the leach products revealed definite changes in BCS particle concentration, size and shape with increasing arsenic levels. Modification of BCS crystal habit from large, well-defined platelets to small acicular (needle-like) particles were observed. An increase in slurry viscosity and decrease in copper extraction accompanied the modification.

2.2.3 Summary of Previous Work

Grewal *et al.* [7] demonstrated that the Second Stage leach reaction mechanisms (reactions 2.1 to 2.3) were essentially sequential in nature and kinetically fast. Based on leach kinetic sensitivity to agitation rate and extended leach behaviour association with high viscosity slurries, a gas-liquid mass transfer rate controlling mechanism was proposed. Clément *et al.* [10] linked high viscosity BCS slurry production to high Cu:S ratios (> 5.0) and high As contents (> 0.9 wt.%) in the feed solids. High Cu:S ratio increased the quantity of BCS produced whereas high As produced a BCS particle morphology change from platelet to acicular shape.

2.3 The Copper-Sulfur-Water System

The stable species belonging to the copper-water system under ambient conditions are presented in Pourbaix's Atlas of potential-pH diagrams [11]. In solutions containing sulfate, the Cu-H_2O system is modified; several new stable species appear, most notably basic copper sulfate compounds.

Stability studies of basic copper sulfate compounds have been done by several researchers [12-16]. Two principal mineral BCS species have been identified: *brochantite*, $CuSO_4 \bullet 3Cu(OH)_2$, and antlerite, $CuSO_4 \bullet 2Cu(OH)_2$. The relative stabilities of these species are highly dependent on conditions of pH, $Cu:SO_4^{2-}$ molar ratio and temperature. Geologically, the occurrence of the two BCS species, with respect to $Cu-SO_4^{2-}-H_2O$ solid phases, have been reported as follows [12]: *chalcanthite* ($CuSO_4 \bullet 5H_2O$), antlerite, brochantite and *tenorite* (CuO), in order of increasing distance from the copper sulfide source (corresponding to decreasing sulfate ion concentration and increasing pH).

2.3.1 Ambient Temperature Studies

Burstorff and van Muylder [13] produced an E-pH diagram of the Cu-S-H_2O system depicting a brochantite stability range between pH 2.6 and 8.1 for unit activities of Cu^{2+} and SO_4^{2-}. Above pH 8.1, CuO was stable. The diagram was incomplete because the antlerite phase was neglected.

Recently, Pollard [12] has found antlerite to be stable only above 30°C. At 25°C, a metastable dihydrate of antlerite, $CuSO_4\cdot2Cu(OH)_2\cdot2H_2O$ was produced; however this species was found to dehydrate rapidly to antlerite once out of solution. Log activity-pH diagrams at 25 and 35°C which included the metastable dihydrate species were subsequently produced (Figure 2.6).
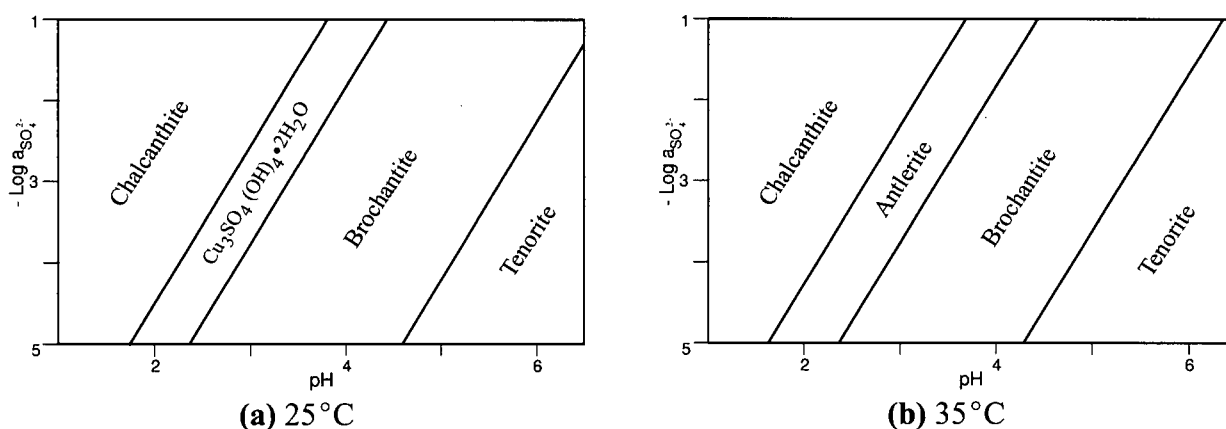
Figure 2.6   Stabilities of solid phases in the copper-sulfate-water system at various temperatures, as a function of pH and sulfate activity [12].

It was also noted that the formation of both the dihydrate and antlerite at ambient temperatures were only achievable if the molar ratio of OH:Cu in solution were carefully controlled to not exceed 1.33. Exceeding this ratio resulted in rapid conversion to brochantite.

2.3.2   Elevated Temperature Studies

At elevated temperatures, a shift in the basic copper sulfate stability region to lower pH values is observed [14,15].

Kametani and Aoki [14] investigated the $Cu-S-H_2O$ system at 90°C and identified specific conditions under which antlerite and brochantite were precipitated at this temperature. Brochantite was formed at a pH of 3.8 from a 0.1M Cu^{2+} and 1M SO_4^{2-} solution. On increasing the copper concentration to 1M with the same sulfate concentration, antlerite was precipitated instead, at a pH

of 2.7.

Kwok and Robins [15] evaluated the thermodynamics of the Cu-S-H_2O system at temperatures up to 200°C. E_h-pH and log activity-pH diagrams depicting the effects of increasing temperatures were generated based on available thermodynamic data and employing the method of Criss and Cobble for Gibbs free energy of formation of ionic species at elevated temperatures [16]. The E_h-pH diagrams at 25 and 100°C reproduced below (Figure 2.7 and 2.8) show an expansion of antlerite stability at the expense of brochantite and the hydrated cupric sulfate species with increasing temperature.

The thermal precipitation of antlerite was also investigated; precipitation was attributed to the combined effects of decreased antlerite solubility (Line A) and increased solution pH (Line B) with increased temperature. As shown in Figure 2.9, a precipitation temperature of 122°C was found experimentally which coincided closely with the calculated value.

Letowski [17] investigated the effect of temperature from 100-200°C on the hydrolysis of copper sulfate solutions to form BCS from initial copper concentrations ranging between 0.01 to 1M. The extent of hydrolysis was found to be greatly affected by precipitation temperature - a decrease in solution copper concentration was found to be 20-40% higher at 200 versus 100°C. TGA and XRD analyses were used to identify the solid hydrolysis product as antlerite.
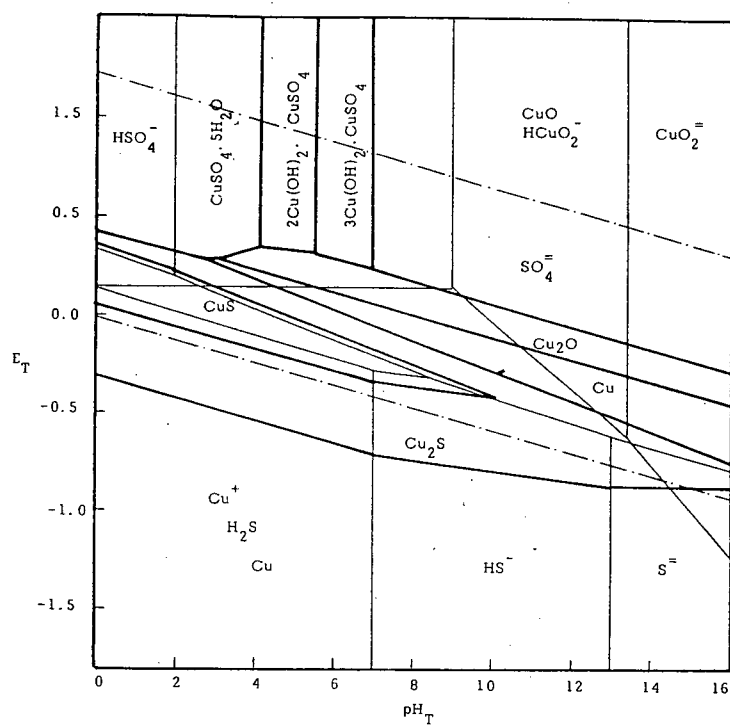
Figure 2.7   E-pH diagram at 25 °C for the Cu-S-H$_2$O system. Diagram drawn for unit activities for all species [15].
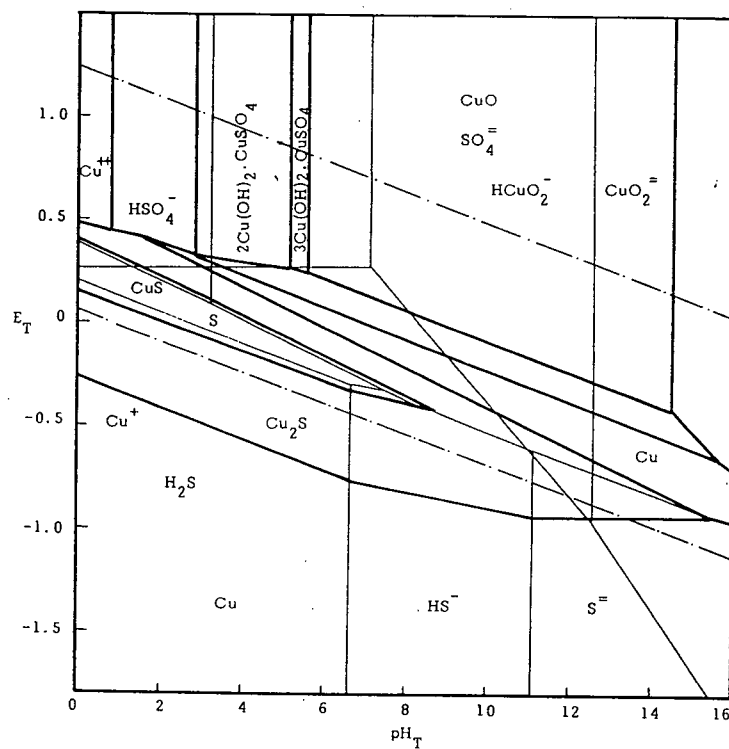
Figure 2.8   E-pH diagram at 100 °C for the Cu-S-H$_2$O system. Diagram drawn for unit activies for all species [15].
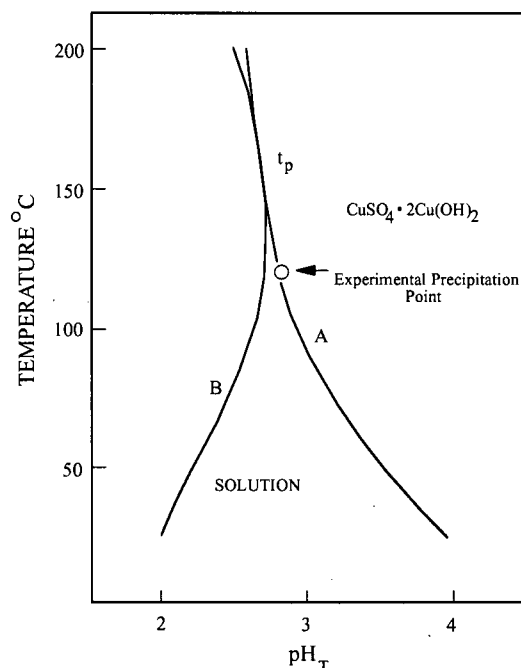
Figure 2.9 Calculated curves for the thermal precipitation of antlerite from a 0.1m CuSO₄/0.01m H₂SO₄ solution. Line A represents the change in antlerite precipitation pH with temperature. Line B represents the change in solution pH with temperature [15].

2.3.3 Potential-pH Diagrams at 115°C and 135°C

Potential-pH diagrams of the $Cu-S-H_2O$ system at unit species activities were created for temperatures pertinent to this investigation. These are shown in Figures 2.10 and 2.11. The thermodynamic data employed were obtained through interpolation of data provided by Kwok and Robins [15] and King [18], and application of the Criss and Cobble method [16]. These are tabulated in Appendix I-A. The HSC software package provided the plotting routine.

The diagram shows that the leaching of Cu_2S in acidic media to form cupric and bisulfate sulfur requires potentials above 400 mV_{SHE}. Under the acid deficient conditions of Second Stage leaching, the acid consuming Cu_2S leach mechanism (rxn. 2.1) results in the precipitation of antlerite -- shown stable between pH 2 to 5. The average BCS slurry pH observed in Grewal's work [8] was 2.8.
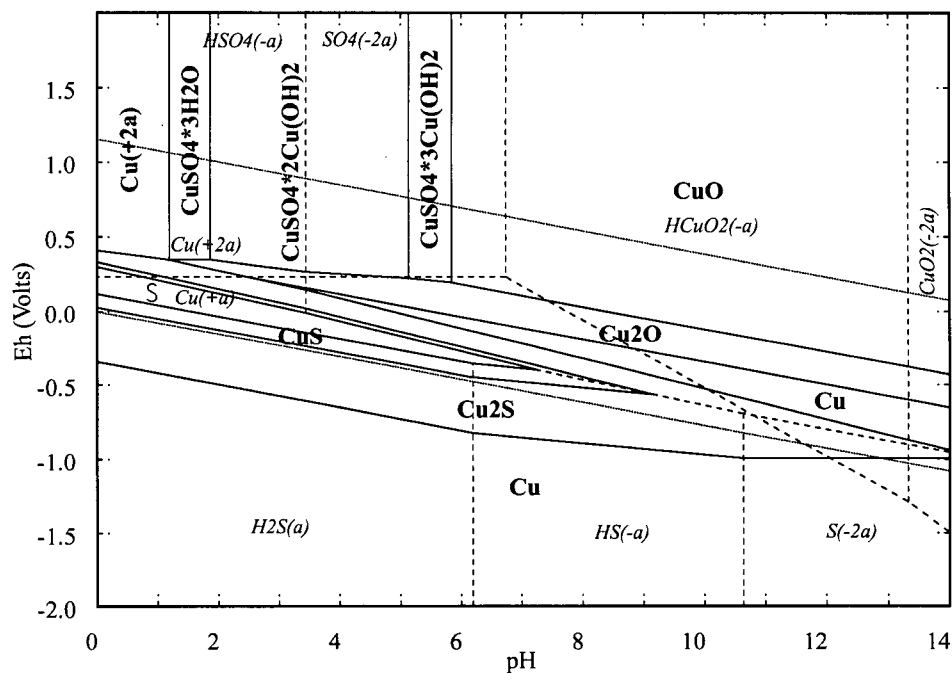
Figure 2.10 E-pH diagram for the Cu-S-H₂O system at 115°C.
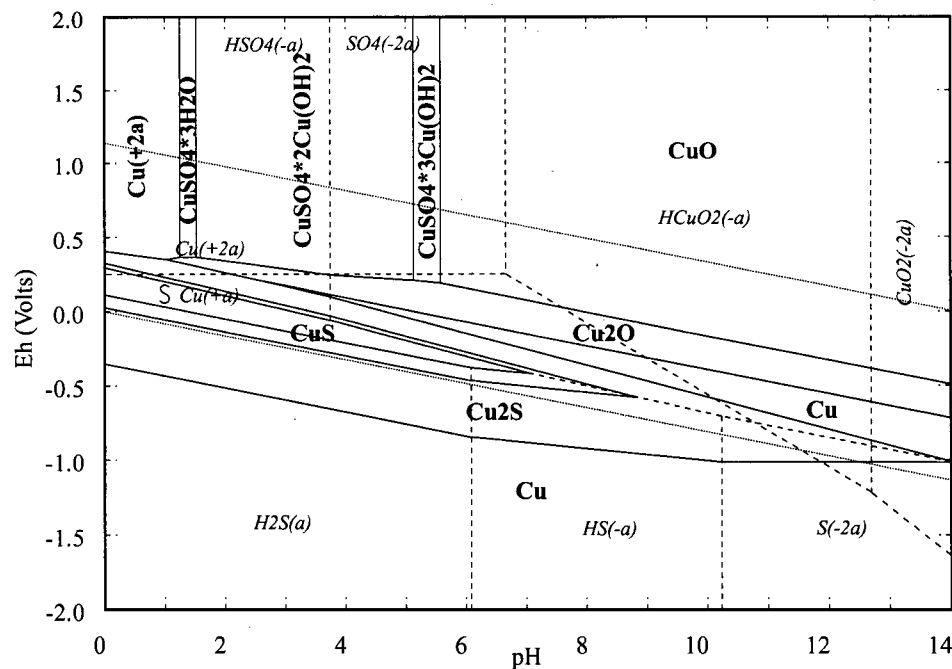
Figure 2.11 E-pH diagram for the Cu-S-H₂O system at 135°C.

2.3.4   Natural Occurrence and Physical Properties of Antlerite ($CuSO_4 \cdot 2Cu(OH)_2$)

Antlerite formations are mainly derived from the oxidation of copper sulfides. Deposits are found in the oxidized zones of copper veins, typically in arid environments. Antlerite commonly occurs as secondary minerals on chalcocite, or as vein infillings from the low temperature reprecipitation of leached copper. The most extensive deposit was discovered in 1925 at Chuquicamata, Chile. Other known deposits are located in Kennecott, Alaska and Bisbee, Arizona.

The structure of antlerite contains Cu in two types of octahedral coordination: $CuO(OH)_5$ and $CuO_3(OH)_3$, which are linked with the sulfate tetrahedra [19]. The crystals are usually tabular on the {010} planes. Schematics of the unit cell and equilibrium crystal shape are given in Figure 2.12. Additional properties are summarized in Table 2.2. The crystallographic properties were obtained from the Powder Defraction File (PDF) #7-407 [20].

Figure 2.12   Orthorhombic unit cell and equilibrium crystal shape of antlerite (see also Appendix I-F).

Table 2.2 - Additional properties of antlerite [15,19]

Physical/Thermodynamic		Crystallographic (PDF # 7-407)		
Molecular Wt. (g/mol)	354.7	Structure	Orthorhombic	
Specific Gravity	3.9	Cell Dimensions (Å)	a	b	c
			8.25	12.01	6.04
$\Delta G^{\circ}_{f,298}$ (kJ/mole)	-1447	Strong Lines	dÅ	I	h k l
			4.86	100	1 2 0
			2.57	85	1 2 2
			2.68	75	3 1 0

2.4 Precipitation from Aqueous Solutions

Because of the importance of basic copper sulfate precipitate characteristics on Second Stage leaching, a review of the fundamental aspects of precipitation was done to shed light on the underlying causes of morphology discrepancies between normal and problematic leach slurries. This section reviews precipitation fundamentals with emphasis on factors affecting the physical properties of precipitates.

2.4.1 Thermodynamics of Precipitation

2.4.1.1 Solubility of Ionic Salts

The equilibrium solubility of a binary ionic salt is represented by the following reaction:

$$M_x A_y + (xb + yc)H_2O \ \leftrightarrows \ x(M^{z+} \bullet bH_2O) + y(A^{z-} \bullet cH_2O) \tag{2.5}$$
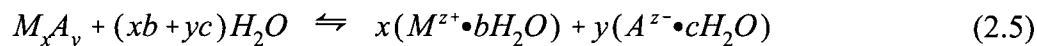
where b and c are the number of hydration water molecules associated with the cation (M) and anion (A) species respectively. In precipitation systems, equilibrium solubility is generally described in terms of the solubility product K_{sp}:

$$K_{sp} = K_{eq}[(a_{M_x A_y}) \bullet (a_{H_2O})^{(xb+yc)}] = [(a_M)^x (a_A)^y]_{eq} \tag{2.6}$$

The term $(a_M)^x (a_A)^y$ is referred to as the *ion-activity product* (IAP) for any state of saturation.

From equation 2.6, the activities of both the solid phase and the solvent influence the solubility product of an ionic salt. It is generally assumed that these activities are constant and set equal to unity, defining the standard state condition. However, the activity of water is dependent on the degree of ion hydration and may be assumed equal to unity only under dilute ionic concentrations.

Deviations from unit solid phase activity result from changes in purity, solid-aqueous interfacial tension (γ) and particle size [21]. Interfacial tension is governed by the degree of structural mismatch of the components across the interface. Factors which influence the interfacial tension of a specific precipitate system include: precipitate crystallinity, lattice density, lattice imperfections and surface heterogeneity. Factors that lead to higher interfacial tension increase

- 23 -

solid phase activity and the propensity for solid solubilization.

The effect of particle size on solid phase activity becomes significant as particle size decreases below 1 µm [22]. Particles of nuclei-size order have higher activities than large particles of the same compound, owing to the higher surface area per unit volume of smaller particles, which is a source of free energy on dissolution. The effect of particle size and interfacial tension on solubility is described by the Gibbs-Thomson equation:

$$\ln\left(\frac{K_{sp(r)}}{K_{sp}}\right) = \frac{2\gamma\overline{V}}{rRT} \tag{2.7}$$

where $K_{sp(r)}$ is the solubility product for a particle of radius r and $\overline{V}$ is the molar volume of the species.

2.4.1.2 Supersaturation

The creation of a stable solid phase requires an activation energy barrier to be surmounted. Physically, this is observed by the exceeding of the equilibrium solubility product without new phase formation, owing to the higher solubility of smaller particles. The degree of supersaturation S, represents the difference in chemical potential between a supersaturated system and a stable saturated system and is expressed by:

$$S_s = [(IAP/K_{sp})^{1/\xi}]_{T,P} \tag{2.8}$$

where ξ is the number of ions per formula unit. The highest degree of supersaturation achievable without spontaneous nucleation is termed the *metastable limit*, a limit largely dependent on the presence of foreign impurities in the system. The various zones of supersaturation are depicted in Figure 2.13 and described below.

1. Stable (undersaturated) zone. Spontaneous precipitation is impossible.

2. Metastable (supersaturated) zone. Spontaneous precipitation is improbable, but crystal growth would occur on existing crystal seeds.

3. Labile (supersaturated) zone. Spontaneous precipitation is highly probable, but not inevitable.

Ion Activity Product (IAP)

Labile Zone

Metastable Zone

a

Stable (Undersaturated)
Solution Zone

c

Temperature
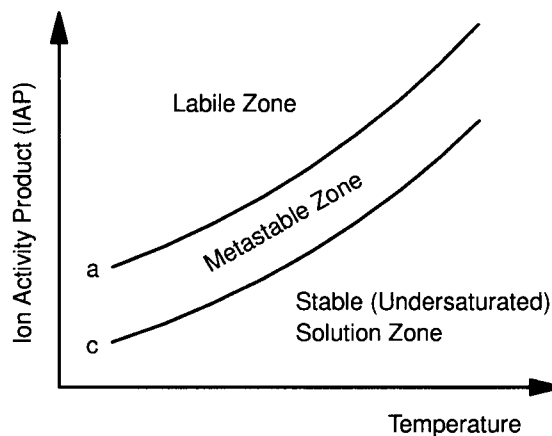
Figure 2.13   The three zones of supersaturation. Line a represents the metastable limit. Line c the represents equilibrium solubility limit [23].

2.4.2   Precipitation Mechanisms

The principal mechanisms governing precipitation processes are: 1) nucleation, 2) crystal growth, 3) ageing (Ostwald-ripening) and 4) agglomeration. The latter two are termed *secondary processes*, occurring after precipitate formation.

2.4.2.1 Nucleation

The nucleation of particles may initiate from either: homogeneous nucleation, or heterogeneous nucleation. The prevalent mechanism depends primarily on the supersaturation level and the presence of foreign substrates present in the system.

I) Homogeneous Nucleation

Precipitation by homogeneous nucleation occurs under conditions of high supersaturation. Minimization of foreign solid substrates also promotes this mechanism. Solute clusters are formed by the interaction of ions or ion pairs; interaction follows the law of statistical mechanics, with probability of interaction a strong function of the degree of supersaturation and temperature. If the supersaturation is increased to a sufficient level, local composition fluctuations above the mean value may be high enough to attain stable nucleus development [24].

a) <u>Nucleation Energetics</u>

The homogeneous nucleation of a solid phase is governed by a volume free energy term (ΔG_V) and a surface free energy term (ΔG_S). For a spherical particle of radius r:

$$\Delta G_{hom} = \frac{4}{3}\pi r^3 \Delta G_v + 4\pi r^2 \gamma \tag{2.9}$$

where ΔG_V is a measure of the free energy change due to bond formation and crystallization enthalpy. In a supersaturated solution, ΔG_V is a negative value and provides the driving force for nucleation.

$$\Delta G_v = -\left(\frac{RT\ln S_s}{\overline{V}}\right) \tag{2.10}$$

Since the free energy change in creating a new surface ($\Delta G_S = A \bullet \gamma$) is always a positive value, the formation of a new phase represents an energy balance between volume energy and surface creation terms. Spontaneous nucleation is achieved when a cluster exceeds a critical size r^*, calculated from the maxima of Equation 2.9.

$$r^* = \frac{-2\gamma}{\Delta G_v} \tag{2.11}$$

Any further addition to the cluster above the critical size will result in a net decrease in free energy and the formation of a stable solid nucleus. The critical size for many sparingly soluble salt systems has been observed to be on the order of tens of angstroms [25]; however, as shown by the above equations, the critical size is largely dependent on the supersaturation. The free energy of a particle of critical size represents its maximum free energy value; this value represents the activation energy required for spontaneous homogeneous nucleation.

$$\Delta G_{hom}^* = \frac{16\pi\gamma^3}{3(\Delta G_v)^2} = \frac{4\pi\gamma(r^*)^2}{3} \tag{2.12}$$

The activation energy required for homogeneous nucleation is therefore, one-third the value of the surface free energy for a spherical particle of critical size.

b) Homogeneous Nucleation Rate

The rate of homogeneous nucleation J_{hom}, is governed by an Arrhenius relation of the form:

$$J_{hom} = K \exp\left(\frac{-\Delta G_{hom}^*}{RT}\right) = K \exp\left(\frac{-16\pi\gamma^3 \overline{V^2}}{3R^3 T^3 (\ln S_s)^2}\right) \qquad (2.13)$$

The coefficient K is a measure of aggregation efficiency and appears to be a function of the ionic diffusion coefficient, temperature and supersaturation [21,25]. The value of 10^{39} m^3 s^1 is a reasonable approximation [25]. The above equations illustrate the extreme sensitivity of nucleation rate to supersaturation.

II) Heterogeneous Nucleation

Precipitation may be induced at significantly lower degrees of supersaturation than required for homogeneous nucleation by foreign substrates present in the system. Foreign substrates may be reaction vessel surfaces or particulate matter, both amorphous or highly crystalline. Heterogeneous nucleation involves the following initial steps:

1) transport of ion or ion-pairs through the bulk solution

2) adsorption on the foreign substrate

3) surface diffusion

4) desolvation of species

5) clustering at active sites.

a) Nucleation Energetics

If the formation of a crystal-substrate interface is energetically favoured over the formation of a crystal-solution interface, a lower activation energy is needed for particle nucleation on the substrate and heterogeneous nucleation will be favoured. The decrease in activation energy due to the presence of a foreign substrate is given by:

$$\Delta G_{het}^* = \phi \, \Delta G_{hom}^* \tag{2.14}$$

where ϕ is a function of the contact angle between the crystal-foreign substrate interface, θ (Figure 2.14) analogous to the wetting angle in solid-liquid systems.

$$\phi = (2 - 3\cos\theta + \cos^3\theta)/4 \tag{2.15}$$

$$\cos\theta = \frac{\gamma_{sl} - \gamma_{cs}}{\gamma_{cl}} \tag{2.16}$$

The subscripts c, l, and s in Equation 2.16 and Figure 2.14 refer to the crystal, liquid and substrate respectively. The limits for θ are summarized in Table 2.3.
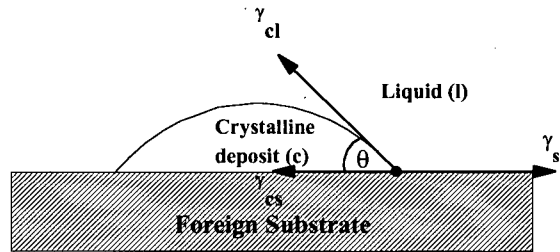
Figure 2.14   Contact angle for crystal-substrate system.

Table 2.3 - Contact angle limits

Contact Angle (θ)	ϕ	Comments
180°	1	Achieved when $\gamma_{sl} \ll \gamma_{cs}$. Tendency to form a crystal/substrate interface is not favoured. Homogeneous nucleation occurs at a high critical supersaturation level.
$0 < \theta < 180°$	$0 < \phi < 1$	Heterogeneous nucleation occurs preferentially. Activation energy requirement decreases as contact angle approaches 0°-- for increasing γ_{sl} and decreasing γ_{cs}.
0°	0	Crystal and substrate are identical. Direct growth occurs without new nuclei formation. Sometimes referred to as *secondary nucleation* [24].

b) <u>Substrate Catalysis Factors</u>

Substrates exhibiting higher values of γ_{sl} and lower values of γ_{cs} will have lower activation energy barriers for heterogeneous nucleation. Highly ordered lattice substrates such as ionic crystals tend to have higher substrate-liquid interfacial tensions than amorphous substrates. Conversely, ionic crystal/ionic substrate interfaces tend to have lower values of interfacial tension compared to amorphous substrates. Foreign ionic crystalline fragments of similar lattice type would therefore be expected to act as highly active heterogeneous nucleation sites for the precipitation of ionic salts, with increasing catalytic ability for increasing lattice matching [26]. This was evidenced by Newkirk and Turnbull's work on the nucleation of ammonium iodide on various mica substrates [27]. A progressive increase in critical supersaturation level above equilibrium saturation was demonstrated from 0.66% for muscovite (1.16% lattice disregistry vs. NH_4I) to 1.17% for biotite (3.40% lattice disregistry).

Identical crystal-substrate systems yield lowest values of γ_{cs}; however, substrates that behave isomorphously with the crystal lattice will also have very low values of γ_{cs}, and will induce nucleation at very low supersaturation levels [28]. Isomorphous substitution of atoms is promoted with increasing similarity between atom size and bond type. Dutrizac *et al.* [29] found that arsenate

ions may isomorphously substitute for sulphate ions up to 4 wt. % during the precipitation of alkali jarosites. Ugarte and Monhemius [30] found SO_4^{2-} to be present in precipitated scorodite, $FeAsO_4 \cdot 2H_2O$, most likely within the scorodite lattice. This suggests that some metal sulfates and arsenates possess similar lattice arrangements and could act as preferential nucleants for one another. Mullin [28] states that many phosphate compounds will nucleate solutions of arsenates. Griffin and Jurinak [31] have found that calcium phosphate will adsorb and nucleate on calcite substrates as hydroxylapatite, $Ca_{10}(OH)_2(PO_4)_6$, by a polynucleation mechanism.

Favourable nucleation sites on a given substrate are points where strong adsorption occur. Preferential sites include: ledges, kinks, notches and holes in increasing adsorption propensity owing to increasing area of crystal-substrate contact (Figure 2.15). Holes, which allow maximum contact between nucleus and substrate are the most active adsorption sites and may be effective nucleants even with poor matching of crystal-substrate lattices [21].

Figure 2.15 Adsorption sites [21].
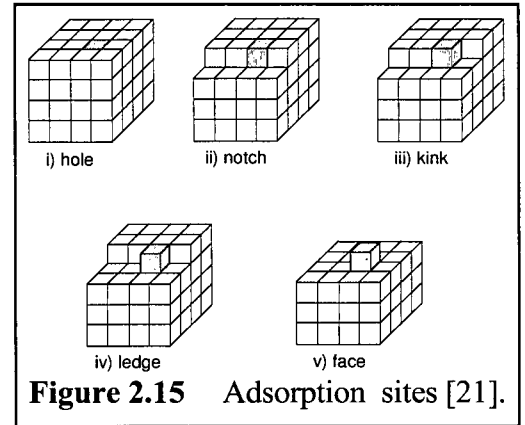
Substrate size also affects nucleation catalysis owing to the size affect on particle free energy with the most active nucleants laying within the range of 0.1 to 1 μm in size [28].

c) <u>Heterogeneous Nucleation Rate</u>

A modified version of the homogeneous nucleation rate predicted by classical theory is offered for heterogeneous nucleation:

$$J_{het} = K' \exp\left(\frac{-\phi(16\pi\gamma_{cl}^3 \overline{V^2})}{3R^3 T^3 (\ln S_s)^2} \right) \tag{2.17}$$

where K' is a factor dependent on the number of heterogeneous nucleation sites available in addition to the factors governing K in Equation 2.13 [24].

The total number of particles formed from heterogeneous nucleation is a function of the

number of foreign particles present and the degree of catalysis offered by the different particulate species; it is not dependent on supersaturation above the critical level. However, as different impurities offers different degrees of catalysis, particle nucleation occurs in waves as the supersaturation level is raised. On increasing supersaturation, the number of particles formed heterogeneously approach a maximum when all available nucleating sites are utilized. Thereafter, further nucleation is achieved homogeneously.

2.4.2.2 Crystal Growth

After nucleation, precipitant free energy is further decreased through crystal growth. The mechanisms involved in crystal growth are similar to that governing the heterogeneous nucleation process and are described in detail elsewhere [32].

The final shape of a growing crystal depends primarily on the rate of its growth. Consequently, different shapes may be produced depending on the degree of departure from equilibrium growth rates.

a) Equilibrium Crystal Growth

Under equilibrium conditions crystals grow in accordance with the Gibbs-Wulff criteria:

$$\left(\frac{\Sigma A_i \gamma_i}{vol.} \right) = minimum \qquad (2.18)$$

$$\frac{d_1}{\gamma_1} = \frac{d_2}{\gamma_2} = \frac{d_n}{\gamma_n} = const \qquad (2.19)$$

where d_n is the distance from face n to crystal centre.

The conditions result in the following [33]:

1. Equilibrium crystal structure corresponds to the configuration requiring the lowest surface energy per unit volume.

2. There exists only one shape that corresponds to the lowest free energy configuration for a given set of state properties (T,P,S_s). This will be the most compact shape possible for the system.

3. Growth rate of a face is proportional to the interfacial tension of that face. The equilibrium crystal structure is bounded by slowest growing faces (lowest γ)

4. Crystal systems with highly varying interfacial tensions will be highly anisotropic. Minerals belonging to the mica group illustrate this property.

Equilibrium crystal shapes are achieved when growth occurs at very low supersaturation ratios (ie. $S_s < 1.00001$ [34]), conditions prevalent in the formation of mineral deposits over geologic time spans.

b) Kinetically Controlled Crystal Growth Shapes

In commercial precipitation processes, kinetic factors take precedence over thermodynamic factors in determining crystal shapes. This is owed to the higher supersaturation levels and temperatures typically encountered which result in a high transformation driving force and very fast nucleation and growth rates. Under these conditions, the negative free energy change for the precipitation of non-equilibrium shapes outweighs the positive change due to departures from equilibrium shapes. Factors that are most influential to crystal shape are: supersaturation, temperature, lattice imperfections and impurities. Crystals resembling equilibrium shapes may be produced if the kinetic form matches that of the equilibrium form; otherwise, highly different crystal habits and morphologies may result [34].

Under mass transport limitations characteristic of high supersaturation levels, anisotropic growth rates across the face tend to produce ill-defined crystal shapes. High initial growth rates may: 1) deplete local solute concentrations in the diffusion boundary layer, and 2) produce an excess flux of solvating molecules away from the growing face which may block the influx of diffusing ionic species [35]. Since the diffusion boundary layer adjacent to corner positions is thinner than

adjacent to face positions, faster growth rate of corners results. Corners extend at the expense of growth normal to faces causing elongation of the crystal. At increasing levels of supersaturation, acicular or dendritic shapes are produced. $CaSO_4 \cdot 2H_2O$ crystals have been shown to convert from platelet to acicular habit by increasing the initial $CaSO_4$ concentrations from 0.27 mol/L to 0.4 mol/L at near room temperature conditions [32].

A similar modification of crystal shape may result from heat transfer limitations resulting from a highly exothermic crystal growth reaction and/or poor hydrodynamics, where a maximization of crystal surface area is needed to dissipate heat at a maximum rate [32].

Table 2.4 illustrates the affect of the initial supersaturation level on the size and shape of crystallites.

Table 2.4 - The effect of supersaturation on crystal size and shape [32]

Supersat. (S_s)	Nucleation Mechanism	Controlling Growth Mechanism	Crystal Size and Shape
< 2	Heterogeneous	Surface incorporation	Compact crystal shape, well developed
2-10	Heterogeneous	Surface incorporation	Compact crystal shape, well developed
10-50	Heterogeneous	Mixed	Ill-developed crystals; dendrites
> 100	Homogeneous	Mixed or Diffusion	Small, isometric crystalline particles often agglomerated
> 1000	Homogeneous	Diffusion	Very small particles or colloids, often amorphous, agglomerates

2.4.2.3 Secondary Processes

As long as precipitates remain in contact with the parent liquor, free energy may be further decreased through the secondary processes of Ostwald-ripening and agglomeration.

I) Ostwald-ripening:

Ostwald-ripening is an ageing process in which small or non-equilibrium shaped crystals revert to a more stable size and shape as driven by thermodynamics to meet the Gibbs-Wulff criteria. Ripening results in the dissolution of corners, edges, dendrite arms and other areas with small radii of curvature, and corresponding growth normal to flat faces leading to an overall coarsening of particles. In poly-dispersed systems, preferential dissolution of smaller precipitates leads to enlargement of larger sized precipitates owing to the particle size affect on solubility.

II) Agglomeration

Agglomeration is the process of particle aggregation owing to interactive forces acting on individual particles. These forces include both the London-van der Waals force of attraction and coulombic repulsion due to surface charge interaction. For particle agglomeration to occur, the London-van der Waals force must exceed the repulsive coulombic forces in the system. The net result is an increase in average size and a corresponding reduction in particle numbers and specific surface area.

The types of agglomerates that may be formed are classified as 1) aggregates and 2) flocs [25]. Aggregates are characterized by strong inter-particle cohesion which yield structures of high density and low porosity. The structures remain stable when subjected to the hydrodynamic shear forces typical of most industrial crystallizers and are only broken under stresses strong enough to cause particle fracture itself [36]. Aggregates are typically comprised of particles of sub-micron size and are formed during the initial stages of crystal growth. Typically, aggregate formations exhibit rough and unfacetted surface characteristics.

Flocs are agglomerates weakly bonded together producing a highly porous structure that is prone to hydrodynamic shear breakages. Flocs are comprised of larger particles - on the order of micron size - which may include aggregate species. Flocs may exhibit high viscosity and pseudoplastic behaviour, conditions detrimental to mixer performance.

2.4.3 Control of Precipitate Properties

Some of the important considerations to commercial precipitation processes are:

- Handling characteristics - solid-liquid separation, mixing, washability, drying rates and caking propensity

- Product size distribution

- Product purity

These properties are influenced by the precipitation process - the relative rates of nucleation and crystal growth and occurrences of secondary processes - and for this reason, are subject to external control and manipulation.

If poor solid-liquid separation is encountered, engineering a precipitate system to have the following characteristics may facilitate the problem: 1) minimization of particle concentration, 2) minimization of precipitate specific surface area - production of large and compact particles, 3) maximization of precipitate density - production of highly crystalline particles. Hydrodynamic/mass transfer limitations resulting from the production of high viscosity colloidal system would similarly be facilitated.

These particle characteristics may be produced by decreasing nucleation kinetics with respect to growth rates, achieved by heterogeneous nucleation at low supersaturations or by doping the system with seed crystals of the precipitant and effecting secondary nucleation. Increased precipitation temperature may also be beneficial as increased Ostwald-ripening rates may be incurred as well as increased precipitate crystallinity owing to the following effects [37]:

- Dehydration favoured
- Neutralization of the charge of the precursor complex is favoured
- Enhanced surface diffusion-mobility of the adsorbed solute
- Accelerated rate of reactive incorporation of solute into crystal.

The production of some ceramic powders and paint pigments often require the precipitation

of a high concentration of sub-micron, mono-dispersed particles (e.g. *nano-crystallites*). This may be achieved through homogeneous nucleation.

The conditions required for the precipitation of amorphous solid products have been described by Sears [38]. A precipitant will grow without an ordered lattice if the critical nucleus size becomes less than one unit cell of the crystalline phase. This may occur for: highly supersaturated solutions and/or crystals with large unit cells. The precipitation of amorphous calcium phosphate over the thermodynamically stable phase, hydroxylapatite, $Ca_{10}(OH)_2(PO_4)_6$ is evidence of this theory [31]. The unit cell of hydroxylapatite contains 18 ion species. Also, solute species possessing high desolvation energy requirements will also have a higher tendency to precipitate as amorphous phases, especially under conditions of high supersaturation and low temperature precipitation. Typically highly hydrated colloidal gels result, an example being ferric hydroxide precipitation from zinc processing operations.

If the production of a highly pure precipitate is desired, such as in the chemical processing industries, solute purification must be performed to avoid impurity co-precipitation. If high levels of purification is unrealizable, conditions promoting rapid growth and agglomeration processes should be avoided because of their tendency to occlude impurities. In impurity removal processes common in many hydrometallurgical applications, such as arsenic/iron co-precipitation with gypsum, the reverse is true; precipitation is designed to enhance impurity removal processes.

2.4.4 Closure

It was found that extended Second Stage leach occurrence was attributable to a transformation of the basic copper sulfate precipitates from large platelets to small acicular particles [7,10]. The precipitation concepts that have been described in this section will be used to gain insight into the mechanisms responsible for such morphological transformations.

Chapter 3

Experimentation

3.1 Research Objectives

The objective of this research was to assess the effect of selected physico-chemical variables on the leaching behaviour of First Stage residues. The experimental program was directed towards determining how the formation of problematic BCS precipitates may be prevented. Experiments were conducted on the laboratory-scale and focussed specifically on two main areas:

1. The role of temperature on the leaching behaviour of various First Stage residues

In many instances, temperature is an important, yet easily controlled parameter in laboratory-scale investigations of chemical reaction processes. As minimal research had been directed towards studying the effect of temperature on Second Stage leach behaviour, a reaction temperature study was proposed. It was hoped that by increasing the temperature, changes in precipitate characteristics would be effected in the direction of producing more compact, higher crystalline basic copper sulfate precipitates which would lead to lower slurry viscosities and facilitate oxygen transfer in solution.

2. The role of arsenic in the promotion of extended leaching behaviour

In Section 2.2 it was discussed that arsenic has been identified as promoting extended leach behaviour in the Second Stage process. An investigation of the problematic nature of arsenic leading to an explanation of its role was desired.

Experiments were performed exclusively at the facilities of INCO Ltd.'s Copper Cliff Copper Refinery (CCCR) in Copper Cliff, Ontario.

3.2 Experimental Variables

The variables investigated in the oxidative pressure leach experiments were:

1) **Feed Solids Composition**. The First Stage residues used as feeds in the study had varying chemical compositions, representative of a range of plant conditions. The assays of the solids used are presented in Table 3.1[2]. The emphasis was placed on feeds with different arsenic levels and arsenic origins. Feeds with arsenic contents of 0.8 wt.% or greater had the following origins: samples #4 and #6 resulted from a Cu-depleted First Stage leach; sample #5 was from incomplete First Stage leaching. Cakes with high Cu:S ratios (>5) are extremely rare in practice and could not be obtained for this study.

2) **Leach Temperature**. Four leach temperatures were employed: 100, 115, 125 and 135°C. Second Stage leaching currently operates at 115°C.

3) **Electrolyte Arsenic Level**. In a select number of tests, the electrolyte arsenic concentration was varied from 0 g/L to 10 g/L.

Table 3.1 - Compositions of the First Stage residues used in the study

Feed #	Cu:S (wt:wt)	Cu	S	As	Fe	Ni	Co
				(Values in wt. %)			
1	4.69	77.4	16.5	0.37	0.46	0.67	0.64
2	4.15	76.4	18.4	0.58	0.17	0.22	0.22
3	4.47	76.5	17.1	0.64	0.24	0.23	0.10
4[†]	4.47	77.3	17.3	0.80	0.12	0.23	0.08
5[††]	3.93	73.5	18.7	0.81	0.82	1.63	0.99
6[†]	4.47	75.4	16.9	1.40	0.34	0.41	0.37

[†] As from Cu-depleted First Stage upset   [††] As from incomplete First Stage leach

---

[2] The feed numbers designated in Table 3.1 differ from the code numbers (CRMT#) used at the INCO Ltd. CRED operation. For equivalent plant code numbers for the feeds used, see Appendix I-C3.

3.3 Apparatus

The oxidative pressure leaching of First Stage residues was conducted in a Parr 2L titanium autoclave. The leach temperature was monitored using a thermocouple probe and maintained at desired set points by external heating and internal cooling coils. Agitation was provided by two, 4-bladed (45°pitch) down-draft impellers connected to a magnetic drive unit. Temperature and agitation were maintained by a Parr controller unit. Oxygen was introduced into the autoclave above the slurry level. Oxygen input rates to the reaction vessel were measured by an OMEGA mass flowmeter and recorded using the Labtech Notebook software package. Slurry viscosity measurements were made using a Brookfield series LV III rheometer controlled by the Rheocalc software package. The experimental setup is represented schematically in Figure 3.1.
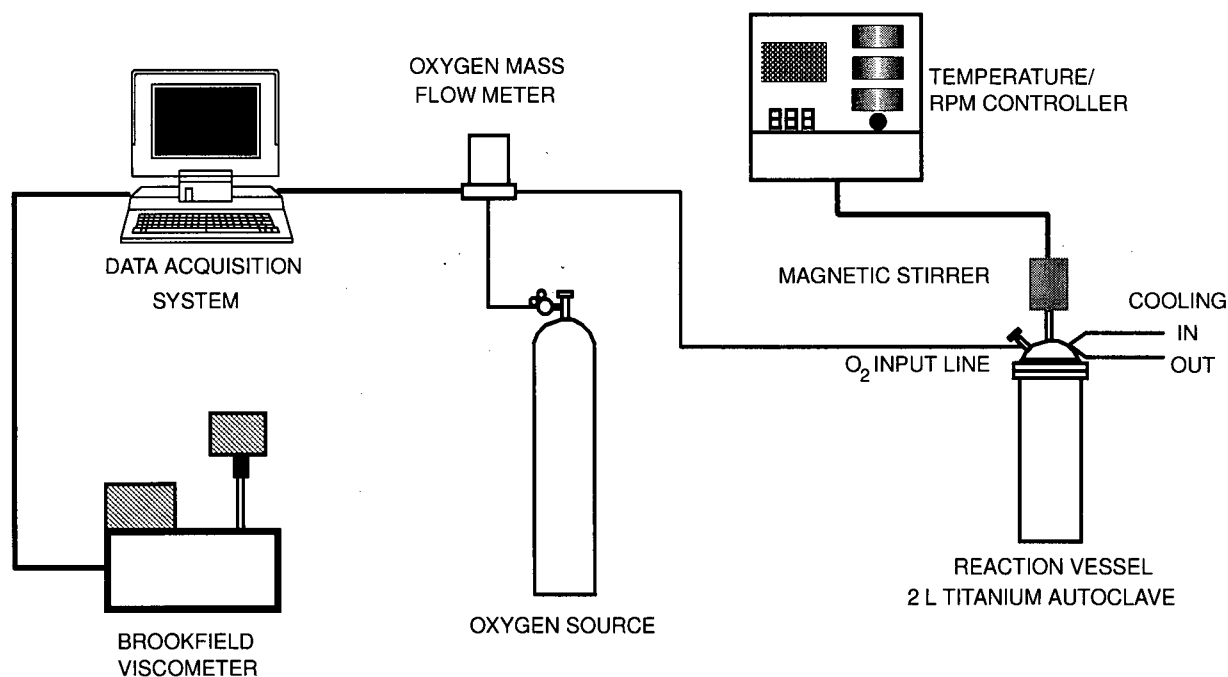
Figure 3.1   Experimental setup used in laboratory-scale oxidative pressure leach experiments.

3.4 Reagent Preparation

The electrolytes used in the leach studies were synthetically prepared by dissolving analytical-grade reagents in distilled water. The standard electrolyte composition followed earlier investigations [7,10], and contained no arsenic: 40 g/L Cu, 5 g/L Fe and 200 g/L H_2SO_4. Copper and iron were added as $CuSO_4 \cdot 5H_2O$ and $FeSO_4 \cdot 7H_2O$. In arsenic electrolyte tests, concentrations of 5 g/L and 10 g/L As were achieved by dissolving anhydrous sodium meta-arsenite, $NaAsO_2$ in the standard electrolyte.

First Stage residues were provided by the plant. Prior to leaching, the residues were repulped, washed and filtered to remove all entrained plant electrolyte. The residues were then stored moist inside air-tight containers until use. A moisture analysis was performed on each residue and chemical compositions were determined by Inductively Coupled Plasma (ICP) analysis.

3.5 Experimental Procedure

The feed slurry for a standard leach test was prepared by combining 510 g of First Stage residue (dry basis) with 500 mL of synthetic electrolyte. Distilled water was added to produce a total volume of 1.2 L. The solids content of the resulting slurry was 30 wt.%. The autoclave was then sealed and heated to the leach temperature. Moderate agitation (450 rpm) was maintained throughout heating to ensure uniform temperature distribution and to prevent solids settling prior to oxidative leaching. After heating to temperature, the oxygen feed to the autoclave was initiated and maintained thereafter at a total gauge pressure of 1034 kPa. Leaching continued over a period of 5 hours at an agitation rate of 820 rpm. Grewal [8] found that this agitation rate was sufficient to overcome oxygen mass transfer limitations in the bench-scale autoclave.

After 5 hours of leaching, the autoclave was cooled below 95°C for pressure release and dismantling. A 600 mL sample of the resulting basic copper sulfate slurry was then removed for potential, pH and viscosity measurements. During viscosity measurement, the slurry temperature was maintained at 70°C by immersion into a heated water bath. Slurry apparent viscosities were measured using the ULA-type spindle. The ULA-type spindle was capable of obtaining viscosity versus shear rate data. This feature was necessary owing to the shear-thinning *(pseudoplastic)* behaviour of the BCS slurries. Consistent with a previous INCO investigation [10] apparent

viscosities were quoted at the specific shear rate of 4.9 s^{-1}. In high viscosity slurries, in which the torque requirements for the ULA spindle exceeded the upper limit of the viscometer at 4.9 s^{-1} shear rate, the LV3-type (non-shear rate obtaining) spindle was used. LV3 values were quoted at 10 rpm rotation speed. Owing to discrepancies in spindle geometry, LV3 measurements do not strictly correlate with ULA measurements. Therefore, the apparent viscosities quoted for the two different spindles can only be compared on an order of magnitude scale.

After viscosity measurement, the leach slurry was filtered and water washed. A sample of the leach filtrate was taken for analysis. A small portion of the BCS filter cake was removed, methanol washed and vacuum desiccated for moisture content analysis and morphology examination by Scanning Electron Microscopy (SEM). The remaining BCS cake was repulped in water and releached at a pH of 0.5 at ambient temperature, by addition of concentrated sulfuric acid. At this pH, all basic copper sulfate dissolves:

$$CuSO_4 \cdot 2Cu(OH)_{2\,(s)} + 2H_2SO_4 \rightleftharpoons 3CuSO_{4\,(aq)} + 4H_2O \qquad (3.1)$$
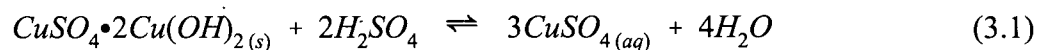
After filtration, samples of the redissolved BCS filtrate and releach residue were taken for ICP analyses.

Chapter 4

Results and Discussion: Oxidative Pressure Leaching Tests

4.1   Preliminary Comments and Observations

Detailed results of the oxidative pressure leaching experiments are provided in Appendix I-C. Summary tables, figures and graphs appear where appropriate. In discussion, any reference to feed solids will be accompanied by the experimental code number. Table 3.1 should be consulted for additional compositional details. The focus of the results analysis will be placed on establishing the following physico-chemical relationships:

- Copper extraction levels versus leach conditions
- Copper extraction levels versus slurry viscosity
- Slurry viscosity versus basic copper sulfate particle characteristics
- Basic copper sulfate particle characteristics versus leach conditions

4.1.1   Distribution of Metallic Species

Soluble copper is distributed between the leach filtrate and the BCS cake. The total copper extracted represented the sum of the leach and releach values minus the initial electrolyte copper content. Extraction values are quoted as a percentage of the initial feed solids copper content. Any leach resulting in less than 97% copper extraction after 5 hours represents extended leach behaviour.

The distribution of elements other than copper were observed as follows: the majority of nickel and cobalt leached into solution and did not reprecipitate; most of the arsenic and iron co-precipitated with the basic copper sulfate and were redissolved at pH 0.5; lead and precious metals reported to the unleached residue.

4.1.2   Oxygen Consumption and E_h/pH Measurements

Monitoring of oxygen flow rate curves was used to identify leach extraction behaviour in progress as distinct oxygen consumption patterns characterized differences between normal and extended leaches. Representative patterns are shown in Figures 4.1a&b. In both cases, the initial

10 minutes of oxygen flow represents pressurization of the vessel at a controlled flow rate of roughly 34 cm^3/sec. Flow rate was regulated to maintain accurate data acquisition during pressurization. Sharp spikes in the pattern were attributed to temperature changes due to periodic cooling water flow.

The sudden decrease in oxygen consumption at roughly 30 minutes characterized extended leach patterns. This time is consistent with Grewal's observation that basic copper sulfate formation had occurred [8], which reflects its significance to oxygen mass transfer limitations.

(a) Normal Leach Pattern   (b) Extended Leach Pattern
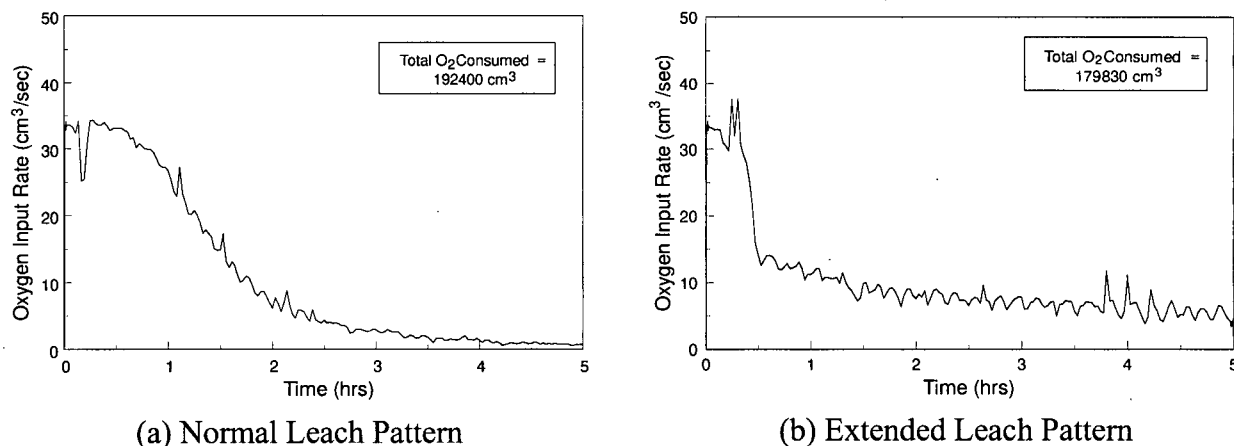
Figure 4.1   Oxygen consumption patterns for bench-scale Second Stage leach experiments. Figure 4.1(a): the leaching of 0.64 wt.% As feed (#3) at 115°C.   Figure 4.1(b): the leaching of 1.40 wt.% arsenic feed (#6) at 135°C.

Slurry pH values for all leaches lay within the range of pH 2.15 to 2.70, measured at 65 ± 5°C. Potential measurements varied between 600-800 mV$_{SHE}$ measured at 83 ± 5°C. A marginal trend towards lower E_h can be seen for decreasing copper extraction and higher viscosity slurries (Appendix I-C). This can be explained by oxygen mass transfer deficiencies in the higher viscosity slurries.

4.2 The Effect of Temperature on Leaching Behaviour

The results for the leaching of various First Stage residues at temperatures between 100 - 135 °C are summarized in Table 4.1. These tests were conducted using the standard (As-free) electrolyte. This was done to assess the effect of arsenic derived solely from feed solids.

Table 4.1 - Oxidative leach test results

Feed #	Feed Assay		Leach	Appar. Visc.*	% Cu
	Cu:S	wt.% As	Temp. (°C)	@ 4.9 s^{-1} (cP)	Extraction
1	4.69	0.37	100	147	94.1
			115	101	99.8
			125	30	99.7
			135	30	99.3
2	4.15	0.58	115	10	99.4
			135	14	98.6
3	4.47	0.64	100	25	93.6
			115	12	99.9
			125	9	99.8
			135	14	99.8
			135	18	99.7
4	4.47	0.80	100	21	95.8
	(Copper Depletion)		115	18	99.6
			115	19	99.6
			125	40	99.5
			135	99	99.5
			135	87	98.7
5	3.93	0.81	100	23	93.5
	(Incomplete Leach)		115	9	99.6
			125	9	99.5
			135	17	99.1
6	4.47	1.40	100	29	93.4
	(Copper Depletion)		115	19	97.7
			125	36	97.8
			135	n/a	85.9
			135	3500(LV3)	83.2

* Apparent viscosity measured at 70°C with ULA-type spindle (unless otherwise noted)

Selected leaches were done in duplicate to check the consistency of the experimental method. The summary above shows that reproducible test results were achieved.

4.2.1   Leaching of First Stage Residues Containing Less than 0.9 wt.% As

The leaching of First Stage residues containing less than 0.9 wt. % As, at the current Second Stage operating temperature of 115°C, resulted in maximum copper extraction levels (>99%) and relatively low product slurry viscosities (9 to 101 cP). The oxygen consumption profiles resembled Figure 4.1a for all feeds.

Leaching at 100°C was found to result in poor copper extraction (93.4 to 95.8%). However, the resulting slurry viscosities were not exceptionally high (<150 cP), suggesting that the slow leach kinetics were attributed to chemical reaction rather than oxygen mass transfer control. Leaching above 115°C did not result in significant changes to copper extraction performance. A minor slurry viscosity increase was noticed with increasing temperature for the higher arsenic feed (#4 - 0.80 wt.% As); the reverse was true for the lowest arsenic feed (#1 - 0.37 wt.% As). The higher BCS slurry viscosities produced from leaching the 0.37 wt.% As feed at 100 and 115°C were attributed to its higher Cu:S ratio.

SEM photomicrographs of typical BCS crystals produced from the leaching of these feeds are presented in Figures 4.2 and 4.3. In general, the precipitates were observed to be compact and platelet-shaped. No conclusive variation in morphology with increasing leach temperature was observed, except for a moderate conversion to a smaller, more asymmetric shape noticed for the 0.80 wt. % arsenic feed (#4) leached at 135°C (shown in Figure 4.6). This is reflected by the slight increase in slurry viscosity.
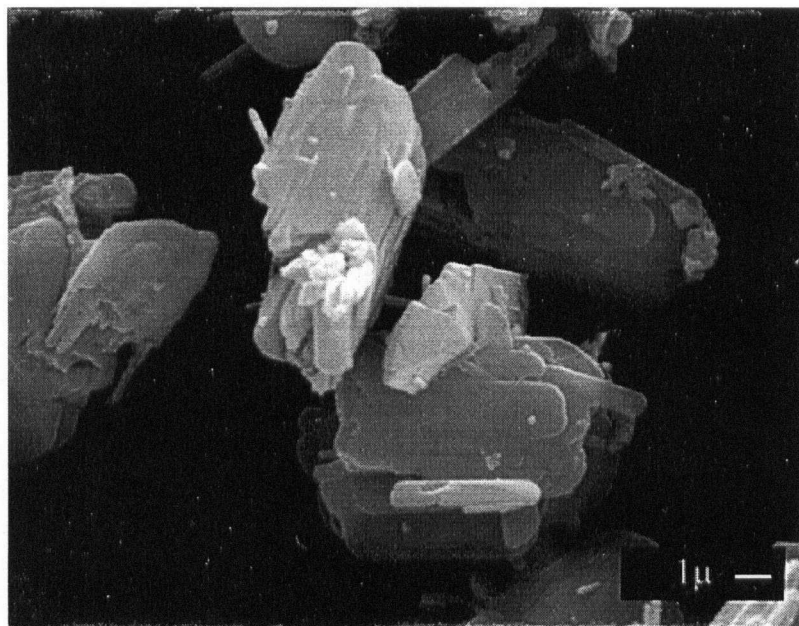
Figure 4.2 Basic copper sulfate crystals produced from the leaching of 0.37 wt.% As feed (#1) at 100°C. (6000x magnification).
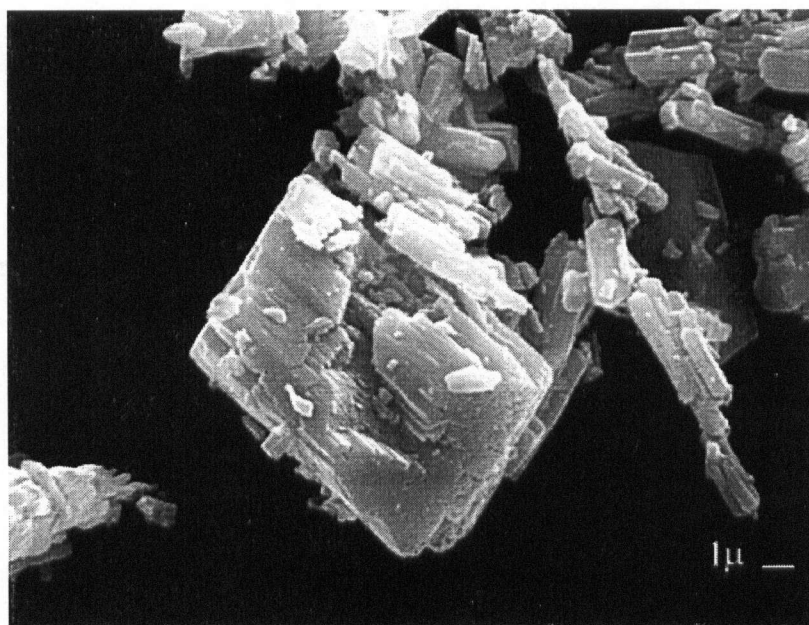
Figure 4.3 Basic copper sulfate crystals produced from the leaching of 0.64 wt.% As feed (#3) at 135°C. (6000x magnification).

4.2.2 Leaching of a High Arsenic First Stage Residue (> 0.9 wt.% As)

Between 100-125°C, leaching a 1.4 wt.% As First Stage residue (copper depletion source) with the As-free electrolyte produced similar results to the leaching of lower arsenic residues. Poor copper extraction (93.4%) was obtained at 100°C. At 115°C and 125°C, copper extractions were lower than for feeds #1 to #5, but still acceptable (≥97.7 %). Low viscosity BCS slurries were produced at all three temperatures suggesting chemical reaction rate control leach kinetics. The basic copper sulfate precipitates produced at each temperature were similar to those shown in Figures 4.2 and 4.3.

Leaching at 135°C, however, resulted in significant differences in copper extraction, slurry viscosity, and BCS morphology characteristics. A highly viscous BCS slurry having very low particle settling rates and extremely poor filtration characteristics was produced. Copper extraction decreased to 83.2%. The apparent viscosity of the slurry was measured to be 3500 cP using the LV3 spindle (10 rpm). Figure 4.4 presents the leach slurry viscosity profiles for the full temperature series. All exhibited pseudoplastic behaviour.

Monitoring of the oxygen flow rates with the data acquisition system revealed that oxygen consumption rates were significantly lower at 135°C in comparison with the lower temperature leaching for this feed. The oxygen consumption pattern for the 135°C test is shown in Figure 4.1b. The 820 rpm agitation prescribed by Grewal [8] as sufficient to overcome oxygen mass transfer limitations in his tests was clearly inadequate for this particular leach system. An SEM photomicrograph of the basic copper sulfate precipitates produced at 135°C is presented in Figure 4.5. A high concentration of acicular, sub-micron crystals indicative of a mass transfer-controlled crystal growth mechanism was evident. The 135°C leach test was repeated and near-identical results were produced.
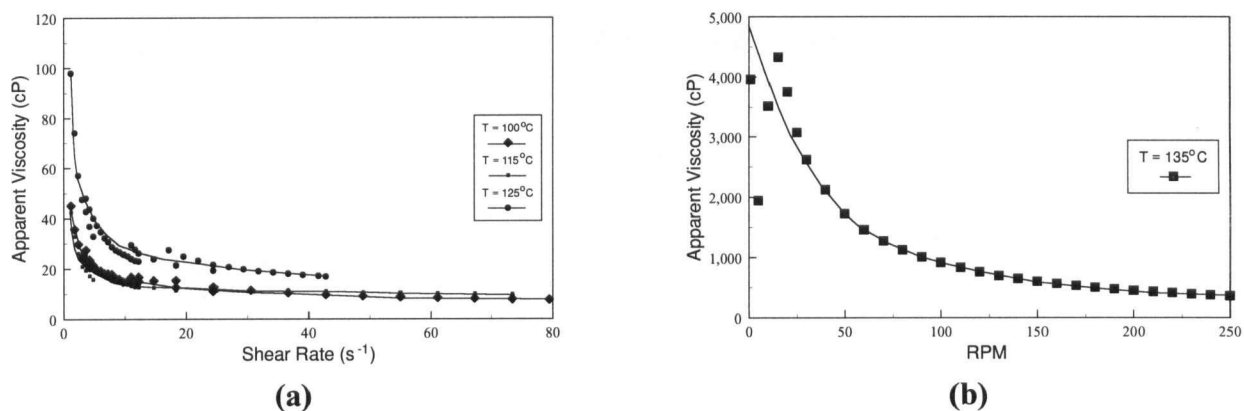
Figure 4.4   Effect of leach temperature on BCS slurry viscosity for high arsenic feed (1.40 wt.% As). Figure 4.4(a) viscosities were measured with ULA-type spindle. Figure 4.4(b) viscosities were measured with LV3 spindle.
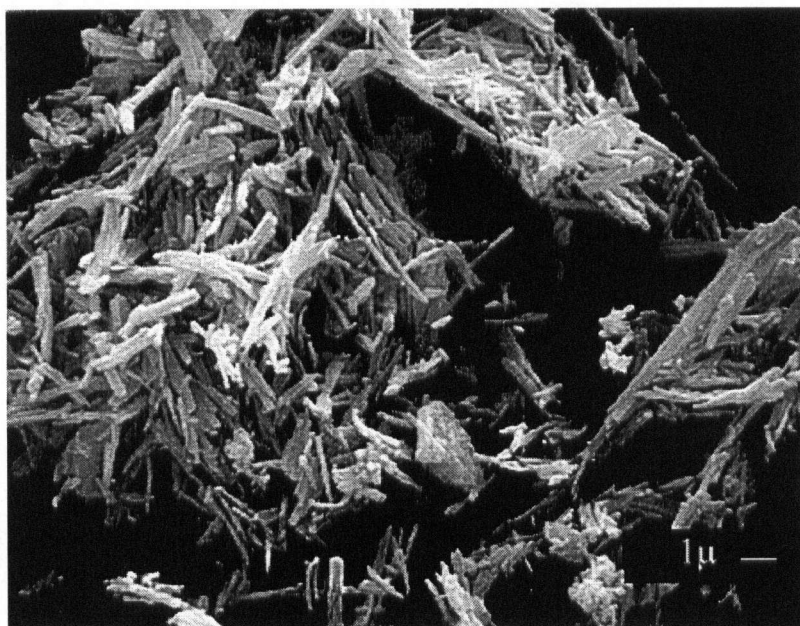
Figure 4.5   Basic copper sulfate crystals produced from the leaching of 1.40 wt.% As feed (#6) at 135°C. Apparent viscosity = 3500 cP (LV3), % Cu extracted = 83.2%. (6000x magnification).

4.2.3 Effect of Feed Solids Arsenic Sources

To assess the effect of different feed solids arsenic sources, First Stage residues having similar arsenic contents (0.8 wt.% As), but from two different First Stage upset conditions, were leached. Between 115 to 135°C, both exhibited full copper extraction (>99%) after 5 hours of leaching. Figures 4.6 and 4.7 present SEM photomicrographs of the BCS morphologies produced from 135°C leaching of the two feeds. The pictures show a higher degree of BCS acicularity for the copper-depleted source than for the incomplete leach source. A tentative explanation may be that arsenic must be present in solution during the early stages of the leach, prior to basic copper sulfate nucleation, to influence the crystal shape. The arsenic present in the residue from copper-depleted First Stage leaching is believed to be in the form of a reprecipitated As(III) compound, such as an arsenic sulfide or metal arsenide. Consequently, this arsenic would be expected to quickly solubilize during Second Stage leaching and oxidize to As(V). Since arsenic from an incomplete leach source is dispersed throughout the First Stage residue, a slower leaching rate is expected. This would result in a lower arsenic concentration at the onset of basic copper sulfate precipitation. Therefore, the detrimental effect of arsenic on BCS morphology would be reduced for this type of arsenic source.

Though the two feeds had similar arsenic levels, they contained different Cu:S ratios and other metallic values, notably Fe, Ni and Co; consequently, reserved judgement must be made on the conclusions of these tests.
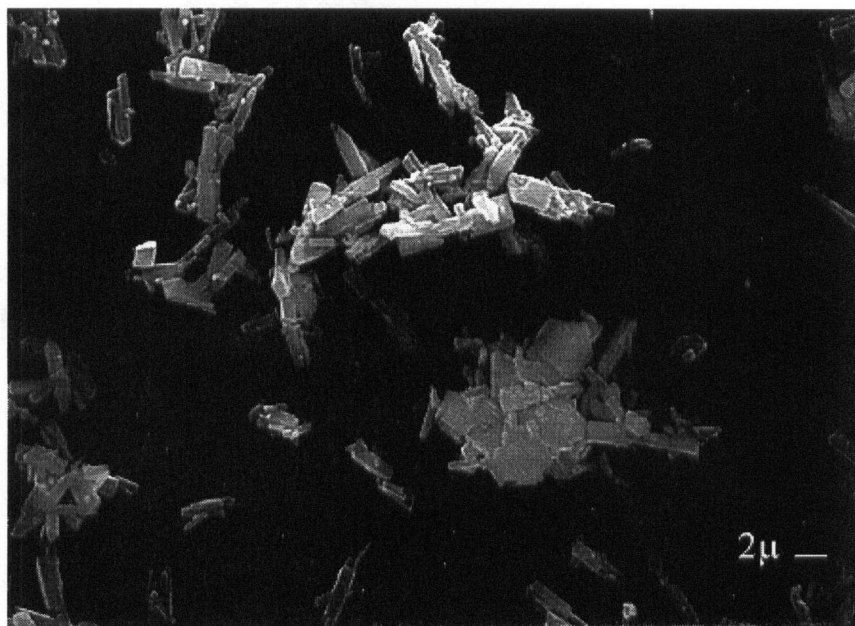
Figure 4.6   Basic copper sulfate crystals produced from the leaching of 0.80 wt.% As copper-depleted First Stage leach source residue (#4) at 135°C. (3000x magnification).
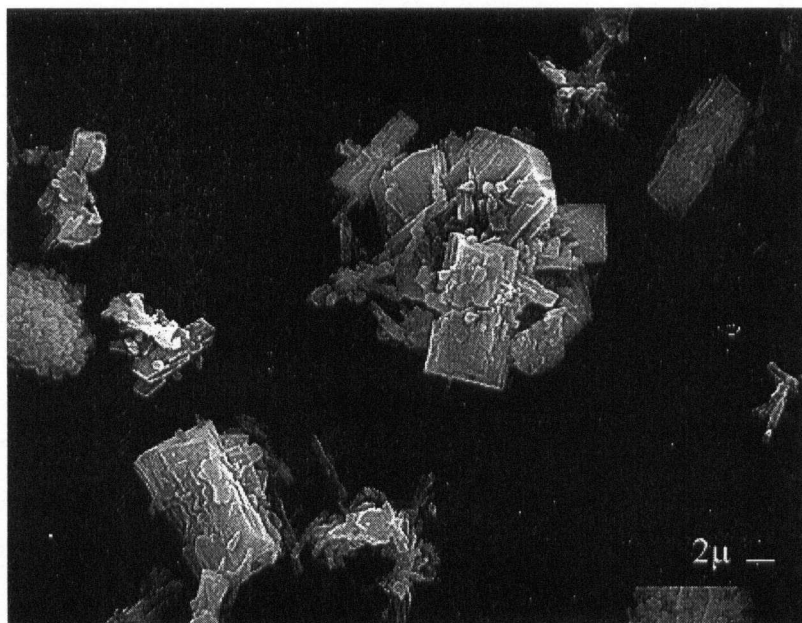
Figure 4.7   Basic copper sulfate crystals produced from the leaching of 0.81 wt.% As incomplete First Stage leach residue (#5) at 135°C. (3000x magnification).

4.3 Effect of Electrolyte Arsenic Concentration

The tests described above were all performed using As-free copper electrolyte. This demonstrated the effect of As from feed solids origin. To assess the effect of electrolyte arsenic, varying concentrations of As(III) were added to the standard electrolyte. This would represent arsenic introduced to the Second Stage leach from recycled spent electrolyte. This could also represent feed solids arsenic from a copper depleted source because of the believed fast redissolution behaviour of the reprecipitated As(III) during Second Stage leaching.

The composition of the First Stage residue leached was: 4.15 Cu:S, 0.58 wt.% As, 0.17 wt.% Fe (feed #2). The electrolyte arsenic concentrations used were 0, 5 and 10 g/L; the total arsenic contents including feed solids composition were equivalent to 0.58, 1.07 and 1.56 wt.%, respectively. Leach tests were performed at two temperatures, 115°C and 135°C, for each of the three arsenic levels.

The results showed that the electrolyte-As system exhibited similar leaching behaviour to that of feed solids arsenic from a copper-depleted First Stage leach (feeds #4,6). Leaching at 115°C resulted in acceptable copper extraction regardless of the arsenic concentration (Figure 4.8). Leaching at 135°C (Figure 4.9) showed a progressive increase in slurry viscosity as electrolyte arsenic levels were increased. Despite the 850 cP apparent viscosity (LV3) obtained from the 5 g/L As test, agitation at 820 rpm still provided a sufficient oxygen incorporation rate as indicated by the relatively high copper extraction level (97.8%). A limitation in oxygen mass transfer was found only when the arsenic level was raised to 10 g/L, resulting in a 1500 cP apparent viscosity (LV3) and only 76.6% copper extraction.

The basic copper sulfate particles (Figure 4.10) show a progression from large, platelet-shaped crystals to smaller and more acicular shapes as temperature and arsenic level were increased, consistent with earlier observations. For the 10 g/L arsenic level and 135°C leach, spherical agglomerates comprised of many individual needle-like crystals are depicted (Figure 4.10-B3). Flocculation may have occurred during the sample drying process and not during the course of BCS precipitation as the high viscosity slurry samples appeared to undergo significant shrinkage cracking upon sample drying during preparation for SEM analysis.

The distribution of arsenic in BCS releach filtrates is shown in Table 4.2. It is evident that the amount of arsenic co-precipitating with the basic copper sulfate for both temperatures increased proportionally to the total feed arsenic level.

Table 4.2 - Distribution of arsenic in BCS releach filtrates for spiked As electrolyte tests

| Condition | 0 g/L As | | 5 g/L As | | 10 g/L As | |
	As (mol) (x 10^{-2})	% Ppt. in BCS	As (mol) (x 10^{-2})	% Ppt. in BCS	As (mol) (x 10^{-2})	% Ppt. in BCS
Feed*	3.94	-----	7.28	-----	10.6	-----
115°C	3.84	97%	7.21	99%	10.6	100%
135°C	3.70	94%	7.01	96%	10.3	97%

* Feed values based on total First Stage residue and electrolyte As contents

This test work has demonstrated that electrolyte As produces the same negative impact on Second Stage leaching as feed solid arsenic from copper-depleted First Stage leaches. The leach tests discussed earlier, which did not have arsenic in electrolyte, would have displayed more pronounced problematic leach behaviour with electrolyte As additions. It is therefore, the combined As concentration, from both solid and spent electrolyte sources, that must be minimized prior to Second Stage leaching.

These results have also provided conclusive evidence of the detrimental role of increasing arsenic concentration at 135°C leaching, as all other chemical variables present in the feed solids were kept constant levels.
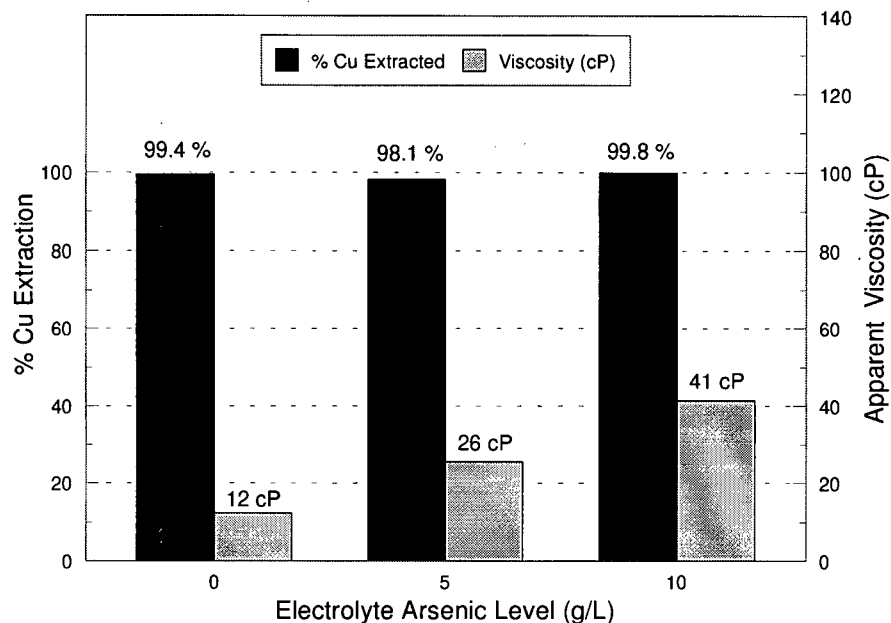
Figure 4.8 The effect of electrolyte arsenic concentration on leach performance at T=115°C. Feed composition: 4.15 Cu:S, 0.58 wt.% As (feed #2). All apparent viscosities measured with ULA-type spindle at 4.9 s⁻¹.
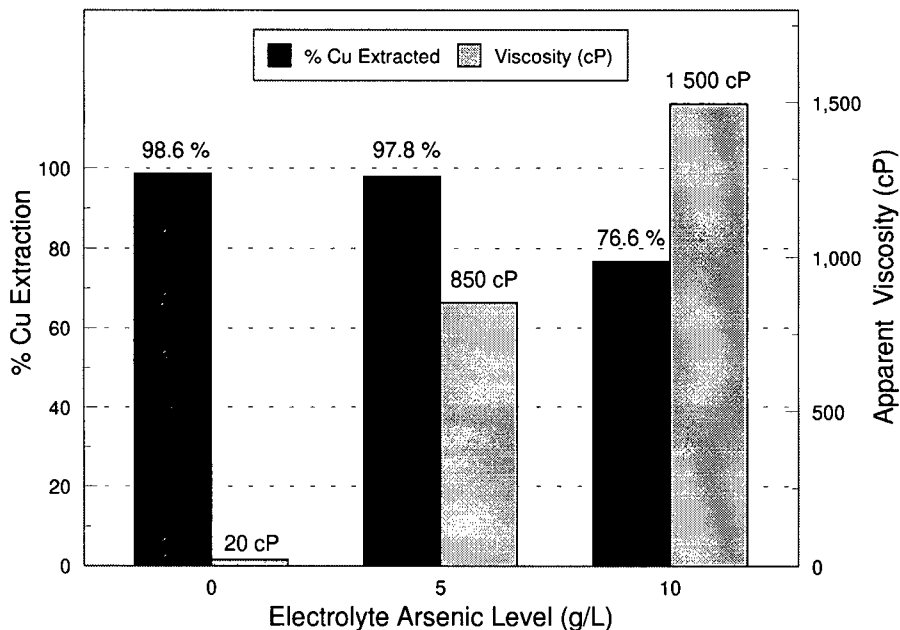
Figure 4.9 The effect of electrolyte arsenic concentration on leach performance at T=135°C. Feed composition: 4.15 Cu:S, 0.58 wt.% As (feed #2). Viscometer spindles used: LV3 for 5 and 10 g/L As leach tests; ULA for 0 g/L As test.
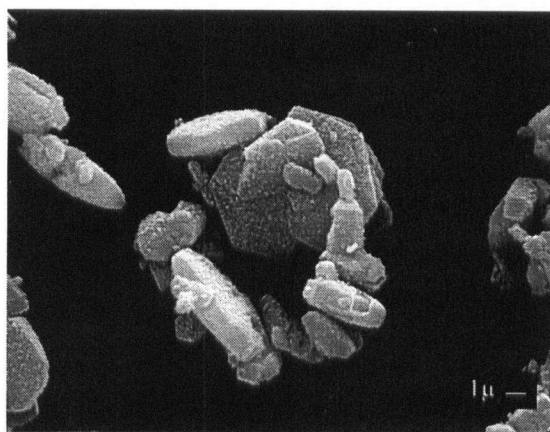
(A1) 0 g/L As
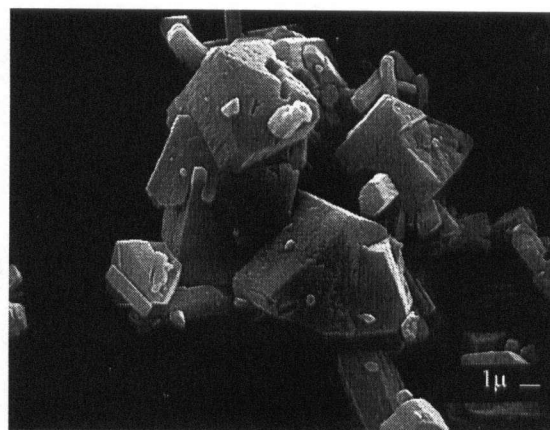
(B1) 0 g/L As
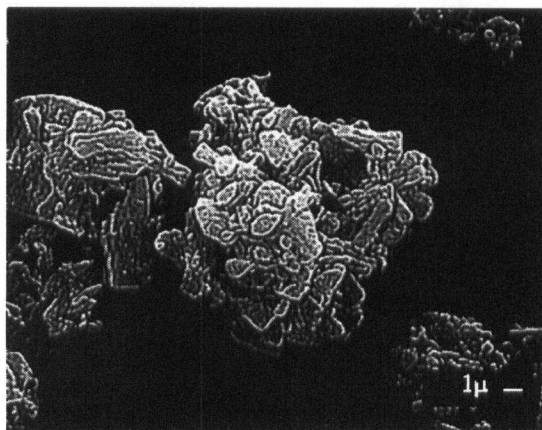
(A2) 5 g/L As
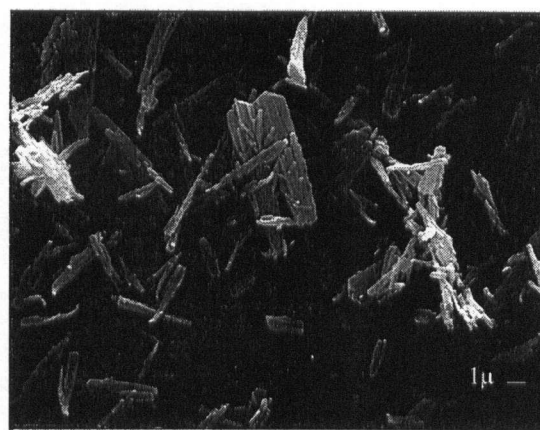
(B2) 5 g/L As
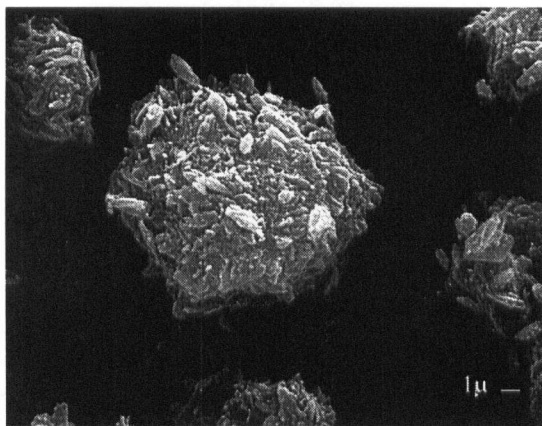
(A3) 10 g/L As
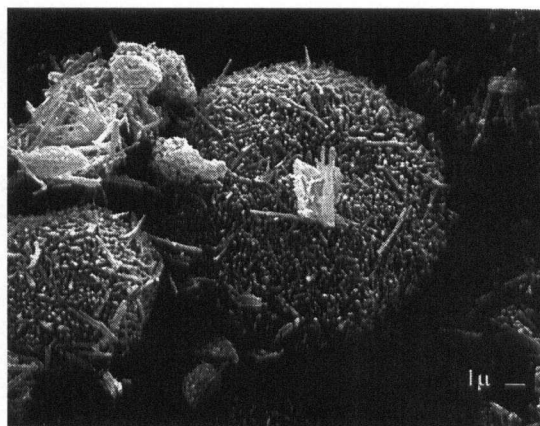
(B3) 10 g/L As

Figure 4.10   Effect of electrolyte As concentration on BCS morphology at: (A) 115°C, and (B) 135°C. Composition of the First Stage residue used for all leaches (feed #2): 4.15 Cu:S, 0.58 wt.% As. (6000x magnification).

Understanding the modifying mechanisms of basic copper sulfate crystal shapes is of fundamental importance in explaining the formation of high viscosity slurries and extended leach patterns observed in the Second Stage leach. It is apparent that the modifying mechanisms are functions of both feed arsenic concentration and leach temperature, and appear explainable by fundamental precipitation theory. A discussion of the possible particle size and habit modifying mechanisms will be presented.

4.4   Effect of Arsenic

Foreign impurities may affect precipitant size and shape by: 1) increasing nucleation rates by forming solids which act as heterogeneous nucleation substrates; 2) effecting epitaxial growth by acting as an oriented substrate or 3) adsorbing and/or incorporating into the growing crystal faces and decreasing growth rates by reducing interfacial energies or by causing internal lattice stresses [26].

4.4.1   Complimentary Investigation - Selective pH Leach of Basic Copper Sulfate

Selective pH leach experiments on the high viscosity basic copper sulfate produced from the 135°C leach of the 1.40 wt.% arsenic feed (#6) were performed [39]. The objective was to identify the precipitate composition as a function of pH to determine if arsenic is precipitated before, after or during basic copper sulfate formation. This could indicate whether arsenic modifies BCS crystal shapes via a substrate-heterogeneous nucleation mechanism or a shape-altering adsorption-incorporation mechanism. A 60 g BCS sample was subjected to redissolution between the pH range 2.53 to 1.86 at a temperature of 80°C. Slurry pH adjustment was achieved by $HClO_4$ addition. Results of the redissolution tests are shown in Figure 4.11 and are expressed as a percentage of the releach filtrate composition obtained at pH 0.5 for which the complete extraction of acid soluble values has been assumed. The chemical compositions of the initial BCS sample, the redissolution residue at pH 1.86 and the final leach residue (pH 0.5) are compared in Table 4.3. An SEM of the initial BCS sample has been presented earlier (Figure 4.5). An SEM photomicrograph of the pH 1.86 residue, showing mostly unreacted covellite, is presented in Figure 4.12.
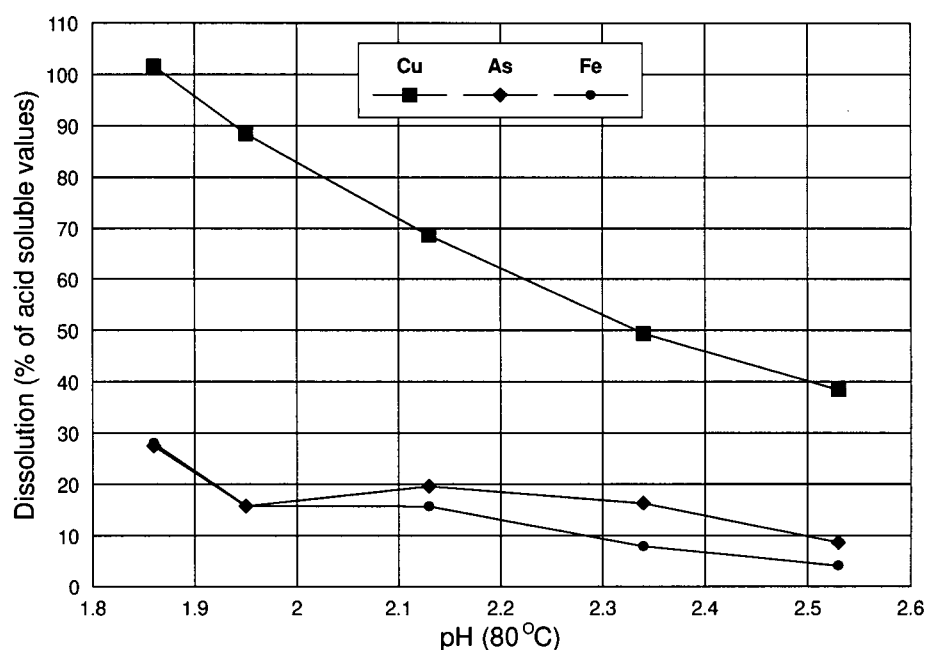
Figure 4.11 Dissolution (% of acid soluble values) of BCS cake at various pH. Total soluble values: 0.35 mole Cu, 9.6x10^{-3} mole As, 6.5x10^{-3} mole Fe. (Sample: ÅCS cake from the leach of 1.40 wt.% As feed at 135°C).

Table 4.3 - Chemical composition and XRD analysis of releach residues

Residue	Chemical Composition (wt. %)					XRD Analysis*	
	Cu	Fe	As	S_{Total}	Pb	Antlerite	Covellite
BCS (initial)	50.1	0.7	1.3	10.7	0.6	M	vm
pH 1.86	49.0	2.8	5.1	21.0	2.7	m	M
pH 0.5	58.5	0.6	0.5	26.0	2.7	---	M

* M = major, m = minor, vm = very minor

Figure 4.11 shows that both arsenic and iron remain stable below the pH of basic copper sulfate dissolution (pH < 1.86), which suggests that their nucleation may have initiated prior to BCS precipitation. The similarities for iron and arsenic dissolution values (28% at pH 1.86) shown in Figure 4.11, do not translate to similarities in the molar concentration of these species. The total moles of soluble arsenic and iron in the tests (60 g BCS sample) were 9.64×10^{-3} and 6.47×10^{3} mole, respectively, representing a molar As:Fe ratio of 1.5.

The drop in % dissolution of both Fe and As values at pH 1.95 was explained by Nissen as follows: "Prior to sampling the slurry after adjusting the pH to 1.95, the slurry sample was cooled to room temperature and reheated to 80°C over a period of 1.5 hours. As a result, the pH of the slurry when the sample was taken was 2.23". The decrease indicates that iron and arsenic reprecipitated during this time; however a similar decrease was not observed for copper. This could be an indication that soluble copper did not revert back to the basic copper sulfate form. This could further indicate that the precipitation of the iron and arsenic compounds occurred at lower pH values than basic copper sulfate.
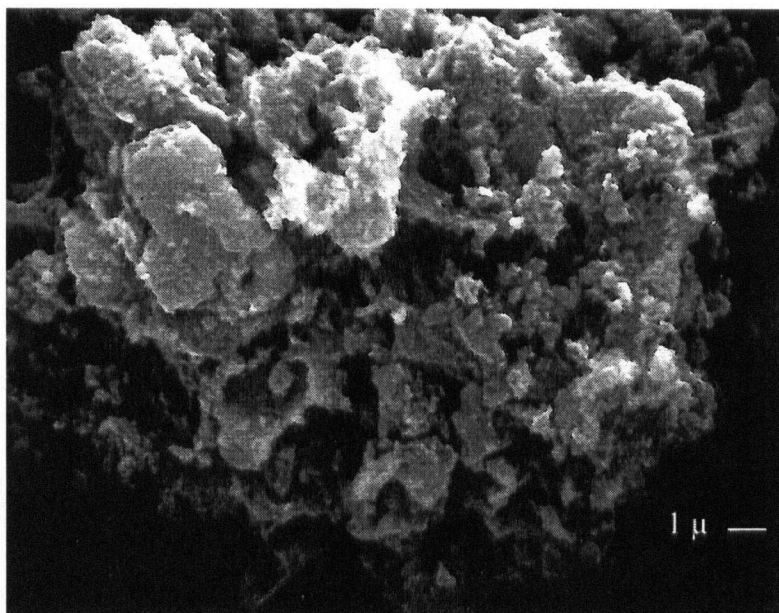
Figure 4.12   Residue resulting from the pH 1.86 redissolution of the BCS sample produced from the leach of 1.40 wt.% As feed at 135°C. (6000x magnification).

- 57 -

SEM qualitative phase analyses of the residues were performed. In all redissolution residues, the presence of two distinct phases were revealed: 1) bright phase containing varying major amounts of Cu, S, Pb and Fe, and 2) grey phase (predominant) containing major amounts of Cu and S with minor amounts of Fe and As. The grey phase composition suggests that an arsenic-iron and/or copper compound is possible. The backscattered-electron photomicrograph of the pH 1.86 redissolution residue is presented in Figure 4.13.
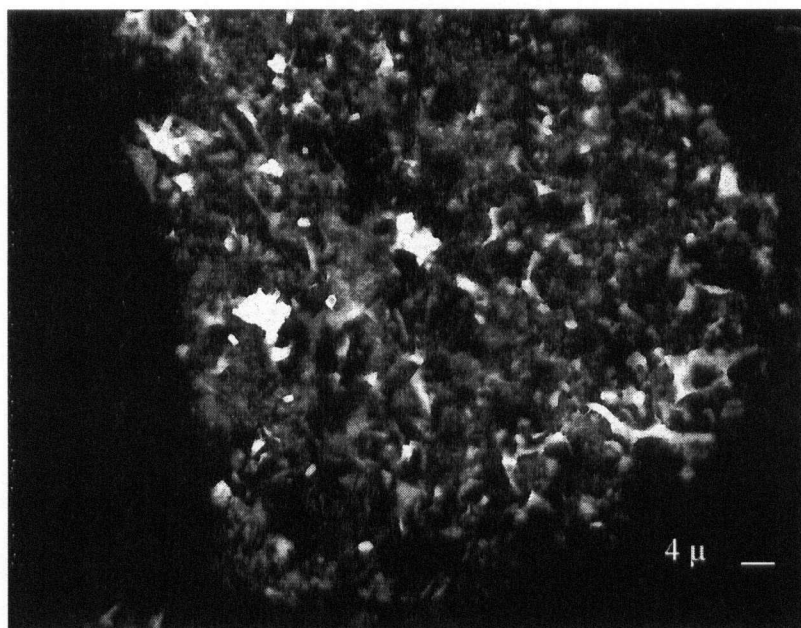
Figure 4.13 SEM backscattered-electron photomicrograph of the pH 1.86 residue. (1500x magnification).

XRD analysis of the redissolution residues showed major antlerite and very minor covellite for all but the pH 1.86 test in which minor antlerite and major covellite were found (Appendix I-D). The XRD pattern obtained from the pH 1.86 residue is given in Figure I-D1. An additional peak was found at 5.90Å. The intensity of this peak increased by a factor of 3 as the redissolution pH was decreased from 2.53 to 1.86. XRD analyses of the final leach residue (pH 0.5), revealed that the peak intensity had once again diminished to near the pH 2.53 value. A probable match to this pattern was found with the jarositic compound *beaverite*, $Pb(Fe,Cu)_3(SO_4)_2(OH)_6$ (Figure I-D4). The

decrease in peak intensity below pH 1.86 is believed attributed to the dissociation of beaverite to *anglesite* (PbSO$_4$).

Initially, an arsenic-bearing jarositic compound, *beudantite*, PbFe$_3$([As,S]O$_4$)$_2$(OH)$_6$, which has a similar XRD pattern to beaverite (Figure I-D5), was postulated as being the As-containing phase responsible for BCS habit modification. However, this has since been ruled out because of two reasons: segregation of As and Pb revealed by backscattered-electron photomicroscopy (Figure 4.13), and the 0.33 As:Fe molar stoichiometry of the compound. As shown in Table 4.4, the As:Fe molar ratios of some BCS releach filtrates approached as high as 2.0; for this BCS sample (#6, 135°C leach), the As:Fe ratio was close to 1.5.

An arsenic-containing species could not be positively identified in the residue at any pH.

Table 4.4 - Arsenic-to-iron molar ratios in BCS releach filtrates

Leach Temperature Series	As: Fe Molar Ratio of BCS Releach Filtrate			
Feed #6	100°C	115°C	125°C	135°C
(4.47 Cu:S, 1.40 wt.% As, 0.34 wt.% Fe)	1.31	1.35	1.42	1.48

Arsenic-Electrolyte Series	As:Fe Molar Ratio of BCS Releach Filtrate		
Feed #2	Temp.	0 g/L As	5 g/L As	10 g/L As
(4.15 Cu:S, 0.58 wt.% As, 0.17 wt.% Fe)	115°C	0.74	1.29	1.90
	135°C	0.93	1.48	2.09

4.4.2 Possible Arsenic Co-precipitating Species

The spiked arsenic-electrolyte experiments revealed that increasing levels of arsenic co-precipitated with the basic copper sulfate as arsenic concentrations were increased (Table 4.2). The selective pH leach experiments indicated that the arsenic bearing compound was stable at a lower pH value than basic copper sulfate (Figure 4.11). These findings suggest that modification of basic

copper sulfate crystal shapes could be attributed to a heterogeneous nucleation effect, with the arsenic-containing solid acting as a preferential nucleation substrate. The current investigation failed to positively identify the arsenic containing species. Examination of identified metal-arsenate compounds reveals the extensive diversity and complexity of this system [40]; however, based on the observations outlined above, some species warrant further discussion.

4.4.2.1 Iron(III)-Arsenate System

Evidence presented by Dutrizac [29] and Robins [41] indicate that if an iron-arsenic compound co-precipitated under the experimental conditions employed, ferric arsenate of the *scorodite* class of compounds $FeAsO_4 \bullet XH_2O$, was a likely candidate. However, the increasing molar ratio of As:Fe in the releach filtrates (Table 4.4) suggests that ferric arsenate was not responsible for BCS habit modification. Nevertheless, it's formation remains possible as revealed by the qualitative phase analysis. The precipitation of basic ferric arsenate, $FeAsO_4 \bullet XFe(OH)_3$ [42], was improbable because of the high iron requirement, which was not met in this study. There is still debate whether basic ferric arsenates are true compounds or simply adsorbed arsenate on ferric hydroxide, with the effect of increasing Fe to simply provide more adsorption surface area [43].

4.4.2.2 Cu(II)-Arsenate System

It has been observed that to reduce the concentration of an aqueous species to near-zero levels through precipitation, a large excess of the co-precipitating ion is needed over the stoichiometric requirement. Precipitation of As^{5+} with iron or calcium are well documented examples [42,44]. In this investigation, the amount of arsenic precipitated approached 100% of the initial feed composition (Table 4.2). The concentration of cupric ions is nearly 10 times greater than any other cationic species in solution. It is therefore probable that cupric is responsible for the precipitation of arsenic from solution. Figure 4.11 which shows that total soluble copper dissolution occurred before full arsenic dissolution would appear to contradict this reasoning. However, if relative moles are considered, the 72% of the arsenic that remains to be solubilized below pH 1.86 would tie up less than 4% of the total soluble copper values. This approaches the limits of experimental analyses. Moreover, full copper solubility at a pH 1.86 could not be true as evidenced by the detection of minor amounts of basic copper sulfate by X-Ray diffraction as earlier mentioned. This discrepancy is again most likely due to the limitations of experimental analyses.

The stability of copper-arsenate compounds in aqueous solutions at 25°C has been investigated by Mirza *et al.* [45] and Harris and Monette [46]. Mirza *et al.* [45] demonstrated that primary copper arsenate, $Cu_3(AsO_4)_2$, formed between pH 2 to 12 from a solution containing 0.1M As^{5+}, 0.4M Cu^{2+} and 0.4M SO_4^{2-}. The pH for minimum solubility of this compound was found to be 6.13 [46].

The copper-arsenate system at 89°C was also investigated by Mirza *et al.* [45] using similar solution compositions as described above. At this temperature, the basic copper arsenate species, *olivinite,* $Cu_2AsO_4(OH)$, precipitated instead of primary copper arsenate. Olivinite was found to be stable between pH 2 and 8, with $Cu(OH)_2$ co-precipitating above pH 4.5. Distribution diagrams summarizing the work are presented in Figure 4.14. The diagrams show that the minimum solubility of Cu^{2+} and As^{5+} occur at a pH 8 and 4.5 respectively. The basic copper arsenate (BCAs) formation reaction was written as follows:

$$2Cu^{2+} + H_3AsO_4 + H_2O = Cu_2AsO_4(OH)_{(s)} + 4H^+ \qquad (4.1)$$
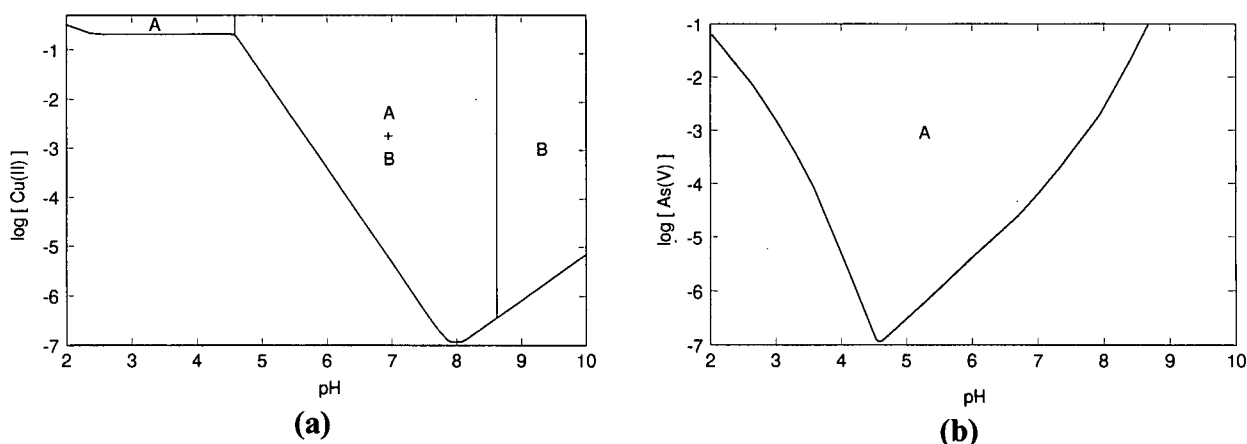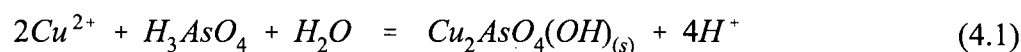
Figure 4.14   Distribution diagram for the Cu(II)-As(V)-sulfate-water system depicting: (a) copper activity; and (b) arsenic activity. Initial solution conditions: [Cu] = [SO_4^{2-}] = 0.4M, [As] = 0.1M, T = 89°C. Species A: $Cu_2AsO_4(OH)$. Species B: $Cu(OH)_2$ [45].

The stability of basic copper arsenate at elevated temperatures was further demonstrated in a recent study by Stewart *et al.* [47]. It was found that a precipitation temperature above 90°C was required to generate a crystalline, low moisture content olivinite product at a pH of 3.5. Results of the work also suggested that basic copper sulfate was not produced during the olivinite precipitation process and only formed at a pH above that required to produce a crude blue copper arsenate product, $Cu_5Me(AsO_4)_4 \cdot NaCl \cdot xH_2O$ (Me = Ca, Ni or Cu), during an earlier stage of the process.

The above indicates that $Cu_2AsO_4(OH)$ could be a stable copper-arsenate compound under solution conditions produced during Second Stage leaching of high arsenic feeds. Based on the reasons discussed below, this species may be responsible for the formation of highly viscous BCS slurries.

4.4.3 Assessment of the Nucleating Potential of Basic Copper Arsenate Species

For basic copper arsenate to be responsible for the crystal habit modification of BCS, the following criteria must be met:

4.4.3.1 Thermodynamics

Calculations of the theoretical precipitation pH values of basic copper sulfate and basic copper arsenate at 115 and 135°C, are shown in Appendix I-B. Activities were chosen to be representative of solution conditions encountered in this investigation. The calculations predict that BCAs should precipitate at lower pH values than BCS. Since the system pH increases with leach time, nucleation of BCS on existing BCAs crystals is thermodynamically possible.

4.4.3.2 Inter-lattice compatibility

The catalysing ability of a nucleant increases with increasing interfacial tension matching between substrate and crystallizing solute (Section 2.4.2) Similarities in interfacial tension are governed by similarities in lattice matching between substrate and crystal. To assess the catalysing potential of basic copper arsenate, a comparison was made of the chemical formulae, lattice parameters and crystal systems of nucleant candidates with that of basic copper sulfate. The results appear in Appendix I-E. The values quoted were taken from available XRD powder diffraction patterns.

Comparison of the crystallographic properties reveal similarities in the unit cell dimensions and crystal systems between olivinite and antlerite crystals. This geometric resemblance combined with the mutual presence of both cupric and hydroxyl species in respective lattices suggests some degree of lattice similarity. The substitutional behaviour of arsenate-sulfate anions in jarosite [29] and scorodite [30] as described in Section 2.4.2, is further evidence of inter-lattice compatibility.

4.4.3.3 X-Ray diffraction analysis

X-Ray diffraction analysis of the selective pH leach residues failed to reveal the presence of basic copper arsenate. Table 4.3 shows that the arsenic content of the pH 1.86 redissolution residue contained 5.1wt.% As. If all of the arsenic were in the form of $Cu_2AsO_4(OH)$, the amount of BCAs in the residue would be 19.2 wt. %. This quantity is by far within XRD detection limits. The formation of ferric arsenate preceding BCAs formation could lower this amount. However, sufficient quantities of BCAs should still be present for its detection. A possible explanation for the lack of BCAs detection in the pH 1.86 residue (Appendix I-D) may be due to the modification of the compound's structure by chemical attack during the redissolution procedure. A second explanation may be the precipitation of arsenic as nano-crystalline BCAs. In terms of crystallinity, nano-crystallites are on the verge of being amorphous and are, consequently, very difficult to detect through X-Ray diffraction. Nano-crystallites are formed under precipitation conditions governed by extremely high nucleation rates, typical of homogeneous nucleation processes. The solution conditions prevailing in the early stages of the leach-- high copper concentration, dissolved arsenic, rapid pH increase, combined with the very low solubility of BCAs above pH 2 [48] suggest that homogenous nucleation of BCAs is possible. This becomes more probable with higher arsenic feeds.

4.4.4 Effects of Basic Copper Sulfate Nucleation Catalysis

According to the precipitation concepts described earlier, the presence of a compatible substrate lattice would decrease the critical supersaturation requirements for BCS nucleation resulting in increased nucleation rates relative to growth rates. Since chalcocite leaching proceeds throughout the precipitation process, the crystallizing solute concentration likely remains at high levels of supersaturation. Combined with the catalysing substrate effect, particle nucleation processes may continue until the majority of substrate sites have been utilized. With increasing number of

sites, higher particle concentrations of smaller sizes would result as the distribution of the crystallizing solute is spread over a larger number of particles.

Therefore, it is suggested that the effect of increasing arsenic levels at 135°C leaching on BCS morphology is due to the formation of higher numbers of arsenic-containing nucleation catalysing substrates. This species is possibly basic copper arsenate ($Cu_2AsO_4(OH)$). As earlier discussed, BCAs could precipitate by homogenous nucleation, a mechanism generally accompanied by the production of high concentrations of high specific area (surface energy) particles.

If feed arsenic concentrations were low, BCS nucleation on a less catalytic substrate such as ferric arsenate, jarosite (beaverite) or chalcocite-covellite intermediate species, may occur which due to higher lattice disregistries decrease the tendency for any subsequent nuclei formation and promote crystal growth.

4.4.5 Possible Effects of Iron

If a ferric arsenate precipitate forms at a lower pH than basic copper arsenate, higher feed iron concentrations could lower the activity of free arsenic in solution prior to basic copper arsenate precipitation. This would result in decreased numbers of BCAs substrates formed and possibly lower BCS particle concentrations.

Such a phenomena could explain the effect of low iron content on leaching behaviour observed by Grewal *et al.* [7], which was not fully addressed. Recalling earlier discussion (Section 2.2), the leaching of a 0.08 wt.% Fe residue with no iron in the electrolyte produced a higher viscosity BCS slurry product and a lower copper leaching rate. The First Stage residue also contained 0.54 wt.% As. It is possible that because of the low iron levels, complexation of arsenic with iron did not occur to an appreciable extent. This would result in high levels of arsenic present in solution at the onset of BCAs precipitation.

If the above hypothesis were true, then increased electrolyte iron concentrations could potentially negate the deleterious effect of arsenic. However, since the system is high in sulfate, jarosite (such as beaverite or hydronium jarosite) precipitation at an even lower pH is also possible

[30]. This would decrease ferric activity and reduce ferric arsenate precipitation. Further work is needed to assess these hypotheses.

4.5   Effect of Temperature

It was initially hoped that increasing the leach temperature would produce a more compact BCS precipitate because of increased driving forces for ageing and crystal ordering processes (Section 2.4.3). This was clearly not achieved as increasing the temperature to 135°C was found to produce less desirable precipitate characteristics. It is believed that this effect was produced because of the following reasons:

1)   Increased supersaturation

The sensitivity of chalcocite leaching kinetics to temperature under oxidative pressure leaching conditions has been demonstrated in several studies [49-51]. Increasing the leach temperature from 115 to 135°C would increase the chalcocite leaching rate, resulting in an increased rate of solute supplied during BCS precipitation. This could possibly result in attaining critical supersaturation beyond the initial nucleation period and lead to an overall increase in particle concentration. Another likely effect is increased crystal growth kinetics which may explain the observed departure from platelet shapes to more dendritic-type shapes. In practice, it is seen that rapidly growing dendritic crystals often fragment and spawn additional crystal growth sites (secondary nucleation). This would further increase the number of particles formed [26].

2)   Decreased nucleation activation energies

Higher temperature of precipitation promotes increased nucleation rates due to both smaller critical nuclei required and increased probability of collision for a given supersaturation.

3)   Decreased precipitate solubility

At temperatures above the boiling point of a solution and under pressure, the solubility of most salts decreases [52]. Kwok and Robins [15] has shown that $CuSO_4 \cdot 2Cu(OH)_2$ follows this trend (Figure 2.9). This results in the lowering of the supersaturation requirement to effect precipitation.

4.6   Summary and Conclusions

Batch-oxidative leaching of various First Stage residues at 100-135°C was performed on a laboratory scale. It was found that the combined effect of high feed arsenic content and high leach temperature was most detrimental to copper extraction kinetics, owing to the formation of high viscosity BCS slurries prior to covellite leaching. This resulted from the precipitation of high concentrations of acicular basic copper sulfate crystals. It was proposed that such a precipitate system resulted from elevated rates of nucleation and growth owing, in part, to higher initial chalcocite leaching rates and the formation of an arsenic-containing nucleation catalysing substrate. It is believed that this species is basic copper arsenate, however, this has not yet been fully verified.

4.7   Industrial Significance and Plant Recommendations

This work has demonstrated that electrolyte As and feed solids As from a copper-depleted First Stage leach produces similar leaching characteristics. Therefore, the combined As level, from both recycled spent electrolyte and First Stage residues, must be reduced to minimize the detrimental effect on Second Stage leaching.

It was also shown that the current operating temperature of 115°C appears to be the optimal leach temperature and, thus, should not be changed. A restricted operating temperature range exists for Second Stage leaching. Below 100°C, copper extraction rates are reduced owing to poor chemical reaction rate kinetics. Above 125°C, the probability of high viscosity slurry formation increases. This indicates that temperature control is extremely important for Second Stage leaching, especially during the initial 30 minutes of leaching, when basic copper sulfate precipitates. In past operation, deficiency in leach temperature control has been observed [8] but the significance in closely regulating this process variable was not fully realized.

Since the reactions involved in the Second Stage leach process are highly exothermic, heat dissipation is required. This is provided by water regulation through vertical serpentine cooling coils adjacent to the inner autoclave walls. At present, the autoclave thermocouple is located between the vessel wall and the cooling coils; therefore, the measured value may not always be an accurate representation of the batch temperature. The pseudoplastic nature of the BCS slurry exacerbates temperature control as viscosity gradients exist: within the high shear impeller zone, slurry

- 66 -

viscosities are low; away from the impeller zone, slurry viscosities may be significantly higher. In the remote location of the thermocouple, severe hydrodynamic limitations may be encountered. At worst, the area may be stagnant. Such factors would probably result in a lower than representative batch temperature reading.

The following measures may assist in minimizing Second Stage leach batch residence times:

1. Improved control of arsenic extraction during First Stage leaching to reduce As input to Second Stage leaching from both feed solids and recycled spent electrolyte.

2. Improved control of temperature regulation to within ±10°C of the target 115°C leach temperature throughout the vessel. Temperature may be better controlled through improvements in thermocouple position and fluid mixing.

3. Improved agitation to maximize gas-liquid mass transfer rate.

An assessment of the gas-liquid mass transfer performance of the Second Stage autoclave and ways to improve this performance are the subjects of the second part of this investigation.

PART II:

Gas-Liquid Mass Transfer and Mixing Studies in a Scaled Model of the Second Stage Leach Autoclave

Chapter 5

Literature Review: Gas-Liquid Mass Transfer/Mixing in Mechanically Agitated Vessel

The mechanically agitated tank is the most widely-used type of industrial reactor vessel. The success of this type of reactor is attributed to its capability of handling independent changes in operating conditions such as variable mixing intensities and residence times.

5.1   Conventional Reaction Vessel Design

5.1.1   Tank System

Most mixing reviews adopt a standard tank geometry as a base-point of comparison for mixing phenomena.   The tank system most frequently adopted is a 4-baffled, vertical, cylindrical tank with a flat or dished shaped bottom. A depiction of the standard configuration along with the standard symbols used for geometry description is given in Figure 5.1.   This geometry is most common; however, in practice several other geometries have been employed, depending largely on the specifics of application, space allocation and fabrication costs.
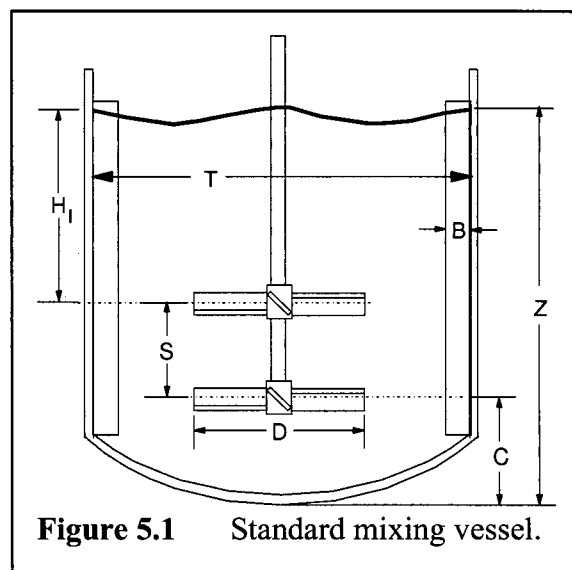
Figure 5.1   Standard mixing vessel.

Other types include: high aspect ratio vertical tanks (bio-leaching, fermentation applications, Z/T > 3), horizontal cylindrical tanks, hemispherical or deep-coned bottom tanks and rectangular or spherical tanks.

5.1.2   Baffling/Internals

For most impellers systems in unbaffled conventional reactors, the dynamics for low viscosity fluids is dominated by vortexed rotary flow. This hydrodynamic pattern is not conducive to fluid mixing as minimal velocity gradients are established. Top to bottom turnover rates are poor and turbulent intensities away from the impeller zone are low. The power draw is generally low

indicating minimal energy transfer to fluid mixing. Increases in agitation rate may result in gas induction if the vortex depth extends to the impeller blade. If this occurs, the overall fluid density and the impeller drag coefficient will be lowered affecting power draw demands. Power draw may become unstable due to differences in liquid-gas properties in the impeller zone and increased mechanical stresses on impeller components may result from increased pressure gradients across the agitator blades (ie. *gas cavitation* effects). Gas induction may also be deleterious to process objectives if the system is oxidation sensitive.

The presence of baffles reduce these problems by promoting multidirectional fluid patterns. Formation of large, central vortices are prevented; gas induction is minimized for impellers under high liquid coverages. Power draw is significantly higher, but is more uniformly distributed throughout the tank volume. Baffling provides the necessary vertical currents required for solid suspension and liquid blending. It also generates high shear stresses needed for effective gas dispersion or agglomerated solids breakdown. Higher mass transfer rates are achieved.

The most common baffle configuration employed is a set of 4 vertical wall baffles of width $W = T/12$ to $T/10$ and length extending beyond the liquid level (Figure 5.1). Such a configuration evolved from power-performance studies. It was found that power demand reached a plateau for a given agitation rate as baffle width was increased to $T/12$ [53]. Any further increase in width did not appreciably increase power demand. Increasing the number of baffles above 4 also did not significantly increase power draw. Similar results to the standard configuration may be obtained using different number of baffles as long as the total projected area is maintained [54].

Baffles are usually mounted with an off-wall clearance to prevent dead volume existence behind baffles where solids deposition may occur. Also, off-wall mounting facilitates tank cleaning, reducing cross-contamination. An off-wall clearance of $T/50$ for low viscosity fluids, with increasing clearances for increasing fluid viscosities was recommended [55].

When baffle installation is not possible or economical, an effect similar to baffling is achieved with an angled entry (10-20°) and/or off-centre placement of the impeller shaft.

The placement of cooling coils in cylindrical tank reactors may also yield a baffle-like effect. Common cooling coil configurations are (Figure 5.2): horizontal spiral; vertical meandering (serpentine) or vertical tube bundles (4 to 6 tubes per bundle). Meandering coils and vertical tube bundles offer baffling effects similar to the standard configuration. For optimal heat transfer characteristics, Shah [55] recommends that spiral coils be used with axial flow impellers and meandering coils or vertical tube bundles be used with radial flow impellers. The coupling of these coils with impeller types yields the most effective fluid circulation pattern between the coils and tank wall.
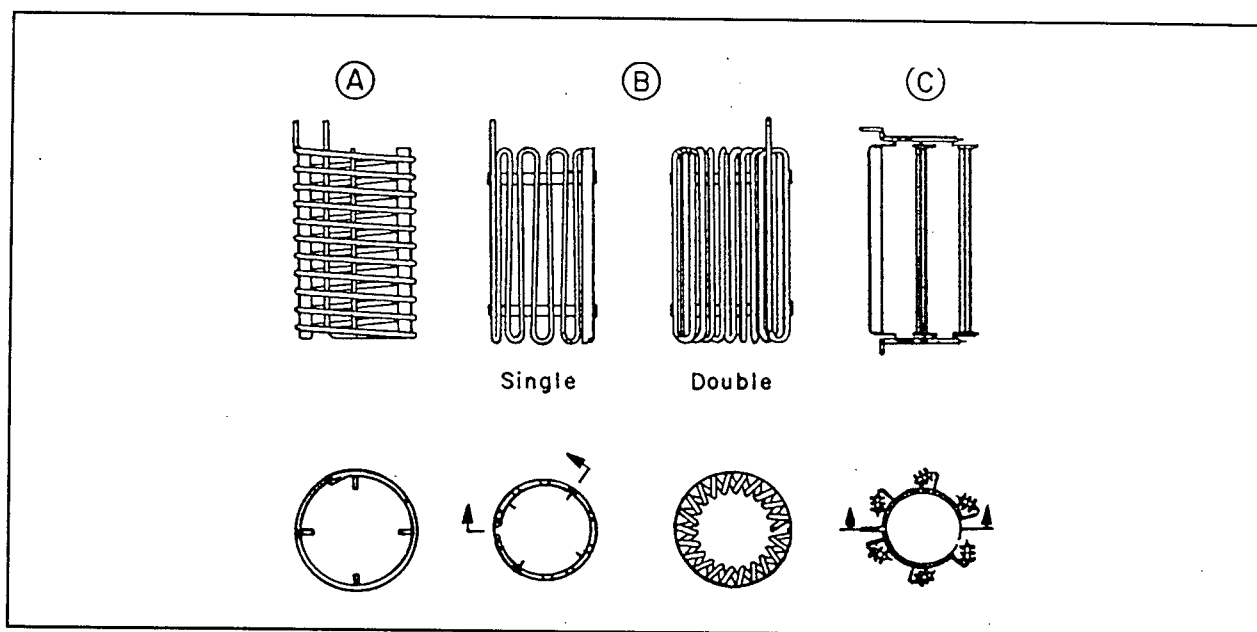
Figure 5.2   Tube coil designs: (a) Spiral coil; (b) meander coils (cooling basket); (c) tube bundles [55].

5.1.3   Impellers Types

Impellers are broadly classified into two categories: axial flow, and radial flow. Common axial flow impellers include: marine propellers, pitched-blade turbines and hydrofoils. Radial flow impellers include: flat blade disk turbines, open turbines and bar turbines. The type and geometry of impeller chosen for a mixing systems is dictated by the process objectives. This will be discussed in a later section.

A brief discussion of the impellers used in this work is given below. For a more extensive review of basic conventional impellers, Oldshue [53] should be consulted. Recent impeller designs and special application impellers including INTERMIGS, sawtooth disk and hollow gas inducing impellers are discussed briefly by Shah [55]. LIGHTNIN impellers [56] and the shrouded helical impeller (AGR) system [57] are discussed in detail elsewhere.

5.1.3.1 Axial Flow Impellers (AF)

A common type of axial flow impeller is the 45° pitched-blade turbine depicted in Figure 5.3a. Generally, these impellers are fabricated having 4, 6 or 8 blades. Depending on the pitch orientation, downward or upward flow may be generated in a baffled tank. The open structure of the impeller permits continuous fluid circulation following the full loop patterns shown in Figures 5.4a. Down-draft impellers (AFD) characteristically generate strong axial flow with a minor radial component. However, vertical flow is severely reduced if the impeller is located at very low clearances (C/T < 1/6) and the resulting flow discharge is directed radially [53]. Updraft impellers (AFU) are less efficient for flow generation; single updraft systems are considered a misapplication and rarely encountered in practice [58].

5.1.3.2 Radial Flow Impellers (RF)

The most common radial flow impeller is the flat-blade radial disk impeller, commonly called "Rushton Turbines" (Figure 5.3b). These impellers consist of a solid circular disk with 6 or 8 mounted vertical blades. Strong vertical flow components enabling top-bottom turnover are achieved with this type of impeller only with concurrent use of vertical baffles. A continuous flow pattern is prevented by the solid disk; consequently, fluid circulation follows the double-loop pattern depicted in Figure 5.4b.
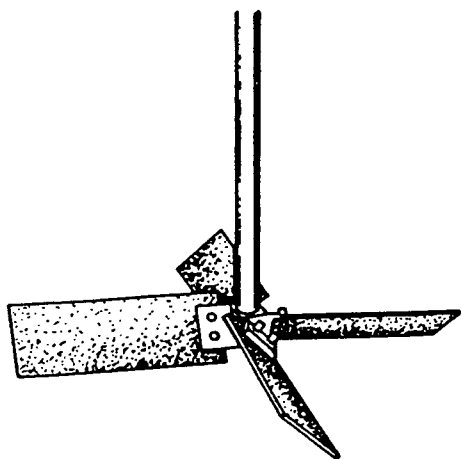
(a) 4-bladed 45° pitch axial flow
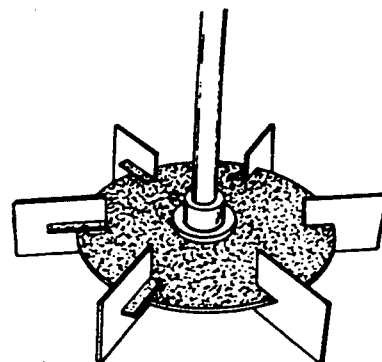
(b) 6-bladed radial disk

Figure 5.3   Common impeller types [58].
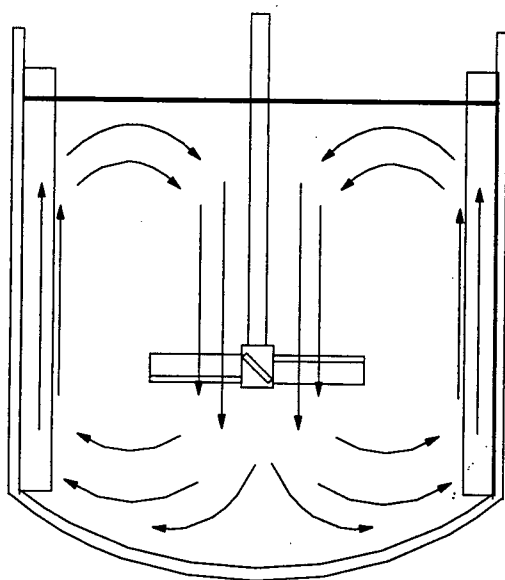
(a)
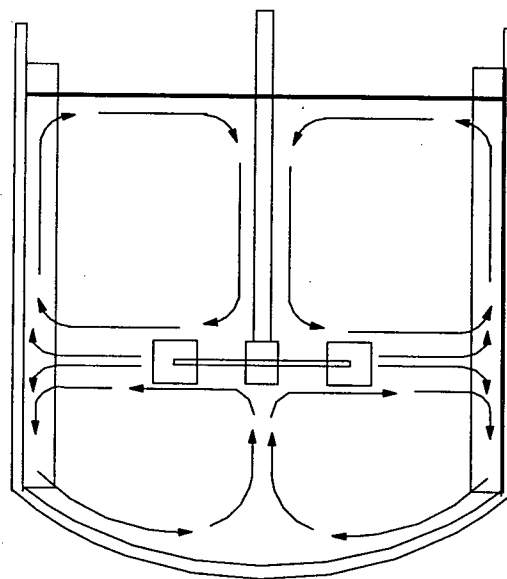
(b)

Figure 5.4   Flow patterns generated in a baffled tank by: (a) axial impellers, and (b) radial disk impellers.

5.2 Mixing Performance and Dimensionless Correlations

The turbulent state in an agitated vessel is represented by the impeller Reynold's number:

$$N_{Re} = \left(\frac{ND^2\rho}{\mu} \right) = \frac{inertial\ force}{viscous\ drag\ force} \tag{5.1}$$

In a fully baffled vessel, the limits: $N_{Re} < 10$ and $N_{Re} > 10^4$ define fully laminar and turbulent conditions respectively [59].

The power drawn by a rotating impeller generates fluid flow (Q) and shear stress[3] (or velocity head, H). Power is ultimately dissipated in the form of viscous heat losses. For a given impeller type, the power draw is a function of impeller speed, and several geometric and fluid characteristics. The dimensionless power number, N_P, equivalent to the impeller drag coefficient is defined as:

$$N_P = \left(\frac{P}{N^3 D^5 \rho} \right) \tag{5.2}$$

The power numbers for some basic impeller types are listed in Table 5.1 below. Radial disk turbines have power numbers roughly 3-4 times higher than AFD type impellers and 10-12 times higher than propellers.

The flow-to-shear distribution of power is governed by the impeller type. Axial flow impellers generate much higher flow and lower shear stress than radial flow impellers. This dictates the choice of impellers for various process objectives. Applications such as solid suspension, liquid blending, and heat transfer require maximum flow generation - axial flow impellers should be employed. In industry, this represents approximately 80% of all mixing applications [53]. For two-phase dispersion-type processes, such as olefin hydrogenation, solvent extraction, and solid dissolution, the benefits of high shear stress often outweigh high flow generation. Radial disk turbines are effective. For three-phase systems, such as oxidative leaching processes, a balance must be achieved between satisfying both flow and shear requirements. Excellent solid suspension

---

[3] In mixing systems, the velocity head (H) is used as a measure of shear stress (τ) where: $H = \tau/\rho$ (in m^2-s^{-2}).

characteristics may be counter-productive to gas dispersion. In biological leaching processes, oxygen mass transfer is often rate controlling; however high shear-type impellers cannot be implemented as excessive shear stress is detrimental to the survival of the biomass [60].

Flow generation is non-dimensionalized to yield the fluid flow number:

$$N_Q = \left(\frac{Q}{ND^3} \right) \tag{5.3}$$

Impeller velocity head (in m^2-s^{-2}) is derived from the power and flow relationships:

$$H = \frac{P}{\rho Q} = \frac{N_P}{N_Q} N^2 D^2, \quad \Rightarrow \quad N_H = \frac{N_P}{N_Q} \tag{5.4}$$

These relationships show that for an equivalent power input, a small impeller operating at a high speed generates higher shear stress than a large impeller rotating at a slow speed. Tabulated flow and velocity head numbers for common impeller types appear in Table 5.1.

Table 5.1 - Power, flow and velocity head numbers for common impellers[†] [53]

Impeller	# Blades/Angle	N_P	N_Q	N_H (=N_P/N_Q)	N_Q/N_H
Marine Prop (AF)	3 Blades	0.35	0.50	0.7	0.71
Pitch Blade - Down (AFD)	4 Blades - 45°	1.5	0.75	2.0	0.38
	6 Blades - 45°	1.6	0.96	1.7	0.56
Radial Disk (RF)	4 Blades	4.0	0.47	8.5	0.06
	6 Blades	5.0	0.68	7.4	0.09

[†] Conditions: 4-Baffles (B/T = 0.1), D/T = 0.33, W/D = 0.2, C/T = 0.33

Under unbaffled or partially baffled tank conditions, in which gross vortexing occurs gravitational effects become significant to the power number correlation. For an unbaffled tank, this occurs for Reynold's number > 300 [61]. The impeller Froude number, accounts for gravitational effects:

$$N_{Fr} = \frac{N^2 D}{g} = \frac{inertial\ force}{gravitational\ force} \qquad (5.5)$$

In two-phase systems, where surface tension effects may be significant, the Weber number may also affect power draw:

$$N_{We} = \frac{N^2 D^3 \rho}{\sigma} = \frac{inertial\ force}{surface\ tension\ force} \qquad (5.6)$$

The power number can then be correlated to the above dimensionless groups in the following manner:

$$N_P = \Pi\ (N_{Re})^a\ (N_Q)^b\ (N_{Fr})^c\ (N_{We})^d = \frac{P}{\rho N^3 D^5} \qquad (5.7)$$

where Π is a constant dependent on impeller type and geometric ratios. For a single-phase mixing application, in a fully baffled vessel, the Weber and Froude numbers are negligible. Furthermore, under fully turbulent conditions, the power number ceases to depend on the Reynold's number. Therefore, for fixed impeller and fluid properties and constant geometric ratios, power draw varies only with N^3.

5.3   Fundamentals of Gas-Liquid Mass Transfer

5.3.1   Physical Absorption

The mass transfer between a gas and liquid phase in the absence of a chemical reaction is termed *"physical absorption"*. The mass transfer rate of such a process is driven by the concentration gradient across the interface and is described by the phenomenological equation of the familiar form:

$$\dot{n}_A = k\left(C_A^* - C_A^b\right) \qquad (5.8)$$

where $\dot{n}_A$ is the gas/liquid molar flux (mol-m^{-2} s^{-1}), k is the mass transfer coefficient (m-s^{-1}) and C^*, C^b are respectively, the interfacial and bulk concentrations of the dissolved gaseous species A in the liquid phase (mol-m^{-3}). In this expression, k is analogous to the heat transfer coefficient (h) used to describe convective heat transfer phenomena ($Q = h(T_2 - T_1)$). The molar flux is dependent on the

additive resistances of the gas and liquid phases. However, for sparingly soluble gas systems such as O_2 and N_2 in water, liquid-film resistance usually dominates and the above expression is written as $\dot{n}_A = k_L (C_A^* - C_A^b)$ or $R_A = k_L a (C_A^* - C_A^b)$ where a is defined as the specific gas-liquid interfacial area (m^{-1}).

Because of the difficulty in measuring the mass transfer coefficient in turbulently agitated gas-liquid systems, various models have been developed to predict k_L. Brief descriptions of the three basic models are given below. For additional details, Treybal [59] should be consulted.

1) The Film Model

The film model is based on the theory that there exists a stagnant liquid film beyond the interface through which transport of the dissolved species occurs by molecular diffusion alone. In this film of thickness δ, the full concentration gradient $(C^* - C^b)$ is established. Beyond the film, the bulk composition is kept uniform by turbulent agitation. The molar flux is given by:

$$\dot{n}_A = \frac{D_A}{\delta}\left(C_A^* - C_A^b\right) \tag{5.9}$$

where D_A is the diffusion coefficient of species A in m^2-s^{-1}. This expression yields: $k_L = \frac{D_A^n}{\delta}$, where the exponent n equals one.

The effect of hydrodynamics is accounted for by the film thickness δ, decreasing for increasing turbulence. For constant hydrodynamics, film theory predicts a linear relationship between mass transfer coefficient and molecular diffusivity of the gaseous species. This does not agree well with experimental evidence where the exponential factor n, has been observed to vary from 0 to 0.8-0.9 with an average around 0.5 [59].

For real gas-liquid systems under turbulent agitation, the gas-liquid interface is not stationary and steady state conditions are not fully established during the short contact time. Therefore, the assumption of a stagnant film layer with a fully established concentration gradient (C^*-C^b) surrounding the gas phase is unrealistic leading to inaccurate film model predictions.

2) The Penetration Model

The penetration model recognizes the transient nature and short exposure times of gas-liquid systems. Two cases in which the model applies are: 1) rising gas bubbles and 2) convective motion of liquids in contact with overhead gas. For rising bubbles, the liquid element initially at the top surface remains exposed to the gas for time = θ, during which the bubble rises by one diameter. As the bubble rises, continuous replacement of the liquid element with fresh solution of bulk concentration occurs. For case 2, an eddy from the bulk remains at the surface of the gas-liquid interface for time = θ, then returns to the bulk and replaced by a fresh eddy. The value of θ is assumed constant, during which time unsteady state diffusion of the gas occurs. The two boundary conditions governing penetration theory are: the solute concentration at the interface equals the saturated value C_A^* for all θ, and, the concentration at the outer edge of the eddy or bubble must always equal the concentration value C_A^b. The latter is a valid assumption provided that θ is small and the diffusivity of the gas in the liquid (D_A) is slow.

When averaged over time = θ, the penetration model predicts that $\overline{k_L} \propto D_A^{0.5}$ (equation 5.10) which agrees well with experimental evidence.

$$\overline{n_A} = 2\sqrt{\frac{D_A}{\pi\theta}}\,(C_A^* - C_A^b) \tag{5.10}$$

3) The Surface Renewal Model

The surface renewal model recognizes that exposure times θ of surface liquid elements is generally not constant as the penetration model assumes. Exposure times of surface elements follow a distribution function. The average rate of gas absorption is found by the summation of individual penetration rates along the age distribution curve. The probability of a surface element being replaced by a fresh element is independent of exposure time. The parameter θ is replaced by the fractional rate of surface renewal s, a function of system hydrodynamics. The mass transfer coefficient predicted by the surface renewal model is given by:

$$k_L = \sqrt{D_A s} \tag{5.11}$$

The inverse of surface renewal rate ($1/s$) may be regarded as the average lifetime of all interface

elements. The surface renewal model therefore, reduces to the penetration model for the special case of a single exposure period $\theta = 1/s$.

The above models are all subject to degrees of uncertainty about the hydrodynamic influence. These appear as the variables: δ, θ and s for film, penetration and surface renewal models respectively. Of the three models, film theory is known to be poorest in k_L prediction based on D_A correlation. However, it is the easiest to visualize and mathematically most simple to calculate. Also, it does well for systems involving mass transfer with chemical reaction where steady state conditions (via chemical equilibria) may be quickly established within the liquid film.

5.4   Gas-Liquid Mass Transfer Rate Optimization

From equation 5.8, the rate of gas absorption may be maximized by optimizing three parameters: 1) the mass transfer coefficient, 2) the specific gas-liquid interfacial area and 3) the interface-bulk concentration gradient. As discussed below, optimization of k_L and a can be achieved through judicious choices of impeller types, geometries and positions, as well as gas introduction systems. Concentration gradients may be increased by increasing the partial pressure of the desired gas phase (increasing C^*). For oxygen absorption in water, this can be achieved by using pure O_2 ($P_{O2} = 1$ atm, $C^*_{O2, 25\,°C} \sim 40$ mg/L) over air ($P_{O2} = 0.21$ atm, $C^*_{O2, 25\,°C} \sim 8$ mg/L) or by increasing the total pressure of air or pure O_2 delivered.

5.4.1   Mass Transfer Coefficient, Specific Interfacial Area and Gas Holdup

The gas-liquid mass transfer coefficient, k_L, is a function of the gas diffusion coefficient in the liquid, D_A, and the hydrodynamic state in the agitated reactor. For a specific temperature and gas-liquid system, D_A is a constant, typically on the order of 10^{-9} m^2-s^{-1} for solutes in an aqueous media. Applying film theory, the mass transfer coefficient then reduces to a function of the diffusion layer thickness, which is decreased through shearing action caused by micro-scale turbulent eddies [59].

The specific gas-liquid interfacial area, a, represents the interfacial area per unit volume of the gas-liquid mixture. Assuming spherical bubbles of diameter d_B:

$$a = \left(\frac{6\,\varepsilon_G}{d_B} \right) \qquad\qquad (5.12)$$

where ε_G represents the volume fraction of the gas phase (gas holdup). Maximization of a is achieved by the creation of the smallest stable bubble size possible and by maximizing gas holdup.

The size distribution of gas bubbles in a dispersion is determined from complex interactions between several physical, chemical and mechanical variables. For a given bubble, the stable size represents an equilibrium between surface tension and shear forces. In a gas dispersion, bubbles are classified into two categories: primary bubbles and secondary bubbles. Primary bubbles are those initially created in the high shear impeller zone. Coalescence of primary bubbles results in the formation of larger, secondary bubbles. Bubble coalescence is a function of collision probability; maximum coalescence frequency is occurs at the periphery of the high shear impeller zone where bubble concentration and velocities are high. It is virtually absent in other parts of the tank because the low kinetic energy of the bubbles cannot stretch out the liquid film between the bubbles to reach the critical coalescence thickness required for drainage [55].

Coalescence is also greatly influenced by the presence of additives in solution. In low viscosity (< 50 cP) pure liquids such as water, methanol or acetone, the average stable bubble diameter is typically between 3-5 mm and $\varepsilon_G \sim 0.1$, independent of the gas distributor used [55]. The stable size is attained immediately after primary bubbles leave the high shear impeller zone. Preservation of primary bubbles by increased agitation is not practical in such a system. In aqueous ionic solutions, the average stable bubble size is observed to be between 0.2-0.5 mm and [55]. According to equation 5.12, this represents an order of magnitude increase in the gas-liquid mass transfer rate over that of pure water for the same gas holdup. The effect of ionic species on bubble size reduction is believed attributable to the influence of electrostatic charges which hinders inter-bubble approach [62]. Coalescence is prevented and primary gas bubble sizes are retained. The effect is more pronounced with increasing solution ionic strength.

However. additives which prevent primary bubble coalescence do not necessarily result in increased mass transfer rates. The addition of 300 mg/L of the frothing agent, methyl isobutyl

carbinol (MIBC) was found to reduce the mass transfer rate of oxygen by 25% [63]. The lower mass transfer rate was believed the result of increased resistance to oxygen diffusion through the surfactant film. This lowered k_L, the magnitude of which outweighed the substantial increase in specific interfacial area.

Coalescence rates may be enhanced by the addition of some organic surfactant compounds. Shah [55] describes that the addition of less than 3 mg/L of some anti-foaming agents may result in the reduction of physical absorption rates by as much as 50%.

The gas phase holdup, ε_G, may be calculated by measuring and then dividing the increase in the aerated liquid level over the static liquid level.

In a given system, sparged at a given gas flow rate, increased holdup is achieved through increased residence times of the bubbles. Decreasing bubble size leading to decreased buoyancy forces permit higher gas back-mixing rates. High impeller shear forces and the presence of coalescing suppressing additives increase holdup. Gas holdup has been found to vary inversely with gas-liquid surface tension, σ with a power of 0.55 to 0.65 [58]. Chapman *et al.* [64] found that beyond a minimum impeller speed, increasing N increases holdup until a maximum value is reached after which further increases in agitation rate has no effect. The use of horizontal baffles mounted near the static liquid surface has been found to increase gas holdup [55].

5.4.2 Design

A basic difficulty in optimizing gas dispersion and mass transfer operations is the conflicting hydrodynamic requirements for bubble creation, gas holdup and distribution processes. Generation of new gas bubbles requires high shear forces, whereas holdup and distribution benefit from increased flow and bulk circulation. As discussed in Section 5.2, shear and flow are opposing consumers of power input and require different impeller types and geometries for maximum effect. However, shear forces have been found to play the more significant role in gas-liquid mass transfer operations [53] and application of radial disk turbines at high impeller speeds have been successful in early studies [65]. Subsequently, these impellers have been extensively researched and are employed frequently in industrial operations.

Gas-liquid contacting in mechanically agitated tanks is achieved through gas-sparging and/or surface aeration. The mechanisms and optimum operating conditions for both methods are discussed below.

5.4.2.1 Gas-Sparging Systems

Most industrial gas-liquid contacting systems involve some form of gas sparging into the liquid phase. Table 5.2 compares the characteristics of various types of sparged gas-contacting systems and shows that in a baffled agitated tank, relatively high rates of mass transfer can be achieved over a wide range of vessel sizes. As a trade-off, however, lower gas-holdup is achieved and higher power draws are required.

Table 5.2 - Comparison of different gas-liquid contacting devices (air-water system) [66]

Device	$k_L a$ (s^{-1})	V (m^3)	a (m^{-1})	ε_G	Liquid Flow[†]	Gas Flow[†]	P/V (kW/m^3)
Baffled agitated tank	0.02-0.2	0.002-100	~ 200	0.1	~BM	INT	0.5-10
Bubble column	0.05-0.01	0.002-300	~ 20	0.05	~Plug	Plug	0.01-1
Packed tower	0.005-0.02	0.005-300	~ 200	0.95	Plug	~Plug	0.01-0.2
Plate tower	0.01-0.05	0.005-300	~ 150	0.85	INT	~Plug	0.01-0.2
Static mixer (bubble flow)	0.1-2	Up to 10	~ 1000	0.5	~Plug	Plug	10-500

[†] BM = Backmixed; INT = Intermediate

Sparge Devices

In mechanically agitated vessels, sparger systems may be of complex design such as ring, disk and cone shaped spargers fitted with orifices, or as simple as a pipe. Sparging devices are generally placed under the impeller for maximum dispersion effectiveness. This is done to ensure that the gas phase passes through the highest shear zone in the tank. The use of radial disk impellers are especially effective for dispersion as the disk forces the rising gas to migrate along the periphery

of the rotating blades. The short circuiting of the rising bubbles along the impeller shaft (low shear zone) is prevented. Axial flow pitched-blade impellers are not as effective as radial disk turbines because of their open structure and lower shear generating capabilities. The optimum size of a ring-type sparger was found to be 0.8 D (impeller diameter) which produced 10-15% higher mass transfer rates over other sizes at a given Q_G and P input [53]. Though this work was done using radial disk impellers, a similar result probably would apply to the axial impeller as short circuiting for such impellers along the impeller shaft would be reduced. The effect of hole diameter and orientation was found to be insignificant provided that the agitation rate is high enough for fluid mixing patterns to prevail over gas flow patterns [53].

McLaughlin *et al.* [63] have shown the ineffectiveness of gas introduction using pipe lances located near the walls of tanks as is still practiced in many operations such as gold cyanidation. Injection of gas by this manner precludes bubble creation and results in short gas residence times for the "one-pass bubbles". In a laboratory study, using radial disk impellers, changing the sparge design to a cone-type sparger resulted in increased mass transfer rates by as much as 4 times (Figure 5.5). Similarly, in full-scale application, steady-state dissolved oxygen concentrations in solution were found to increase by a factor of 3-4 times, and approached oxygen-air saturation limits (Figure 5.6). In addition, higher dissolved oxygen concentrations were obtained from the cone sparger-air system than with a wall sparging-tonnage oxygen system (tanks 3,4).
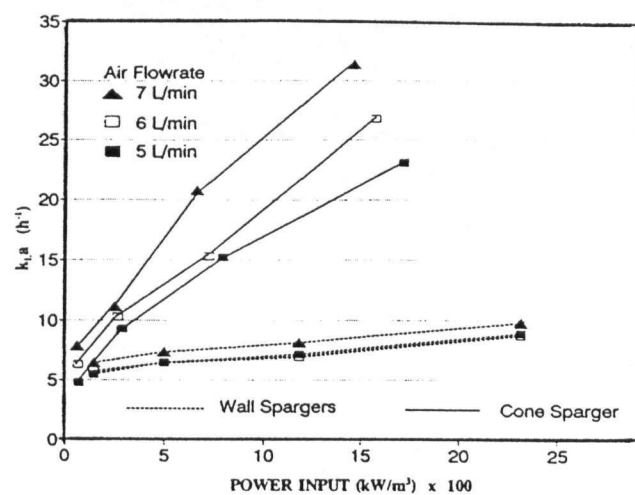
Figure 5.5   The effect of sparger type on oxygen mass transfer rates at various air flowrates [63].
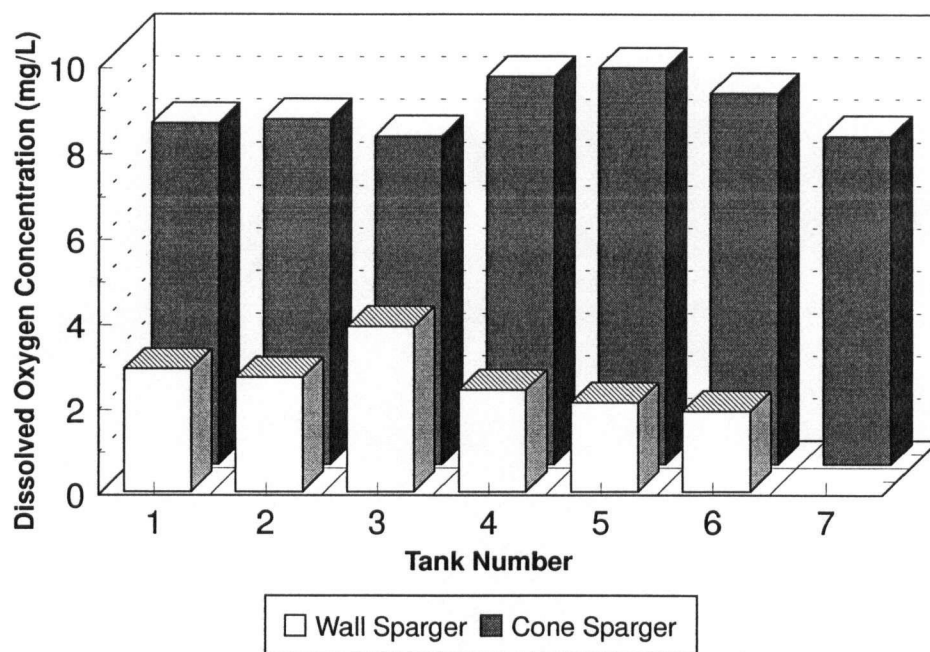
Figure 5.6   Dissolved oxygen profile before and after installation of cone spargers [63].

Gas dispersion mechanisms

The mechanistics of sparged gas dispersion by mechanical agitation have not yet been fully elucidated. For radial disk impellers, however, the proposal by van't Riet and Smith [67] has gained acceptance. According to the authors, the rotation of the radial-disk impeller generates low pressure zones on the back-side of the flat blades. Sparged gas migrates into the low pressure zones, forming ventilated cavities. For a given sparging rate, three different size and shaped cavities may result depending on the impeller rotation speed (Figure 5.7). At low speeds, large cavities covering the entire back blade side results (Figure 5.7a). At higher speeds, the cavity volume reduces and the shape begins to conform to that of the trailing vortices (Figure 5.7b), With further speed increases, higher volume reduction occurs and the trailing end becomes backward swept (Figure 5.7c). Primary bubbles are created and discharged from the trailing ends of the gas-filled cavities.

Because of their poorer gas dispersing properties, axial impellers have not been as widely studied as radial disk impellers. At low gas rates, bubble creation appears to result from the shearing action of the downward liquid flow coming in contact with the gas orifice [64]. At higher gas flows, the level at which bubble shearing occurs approaches the hub of the impeller.

Critical Agitation Speed

The impeller speed required to adequately disperse gas is directly related to the gas sparging rate. For a given sparge rate, there exists a minimum speed requirement for effective gas dispersion below which, gas floods the impeller and negligible dispersion results. This is accompanied by a step decrease in impeller power consumption. The flooding transition has been proposed to be a balance between impeller pumping and the buoyant pumping of the bubbles and may be correlated by the gas flow number and the Froude number as follows [68]:

$$\frac{Q_G}{ND^3} = \Pi\left(\frac{N^2D}{g}\right) \tag{5.13}$$

with Π dependent on geometric factor; $\Pi = 1.2$ for the radial disk turbine system employed.

Two other critical agitator speeds relevant to gas dispersion systems have been investigated by Chapman *et al.* [64]. These are the minimum speeds for complete gas dispersion (N_{CD}) and gas recirculation (N_R). It was found that these critical speeds could be accurately identified on gassed power number vs. 1/N plots as shown in Figure 5.8. Previously, these speeds were identified by visual observation of dispersion patterns (Figure 5.9).

Mechanistically, for radial disk turbines, the power number minima at N_{CD} and maxima at N_R were explained as follows:

1. With increasing N, increased size gas cavities form. The cavities raise the local pressure behind the impeller blades and reduce the front-back pressure gradient. The clinging gas cavities also act to streamline the impeller, reducing drag. A minimum power number occurs when the gas cavity covers the entire blade face (Figure 5.7a). This corresponds to N_{CD}.

2. Further increases in N causes the size of the cavity to decrease so that less of the blade is covered by gas. The cavity shape progressive to that of vortex cavities (Figures 5.7 b,c) and power number increases.

3. At a certain speed, N_R, the onset of gas recirculation occurs, which reduces the mean fluid density and therefore, power draw begins to diminish again.

— Direction of rotation
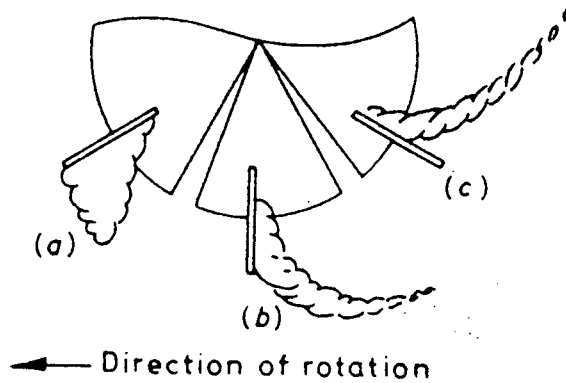
Figure 5.7   Changing cavity shape with increasing speed (N(a) < N(b) < N(c)) for disk turbines at a constant gas flow rate [64].
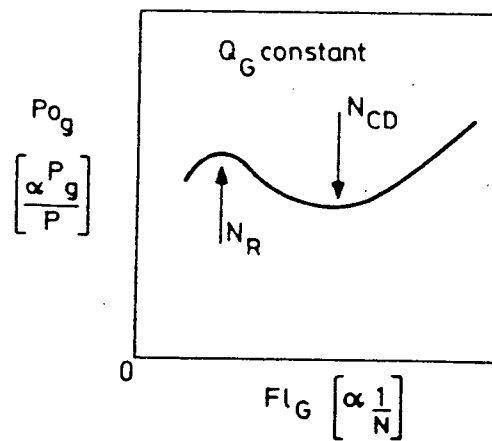
Figure 5.8   Power number versus flow number for disk turbine at a constant gas rate (Q_G) [64].
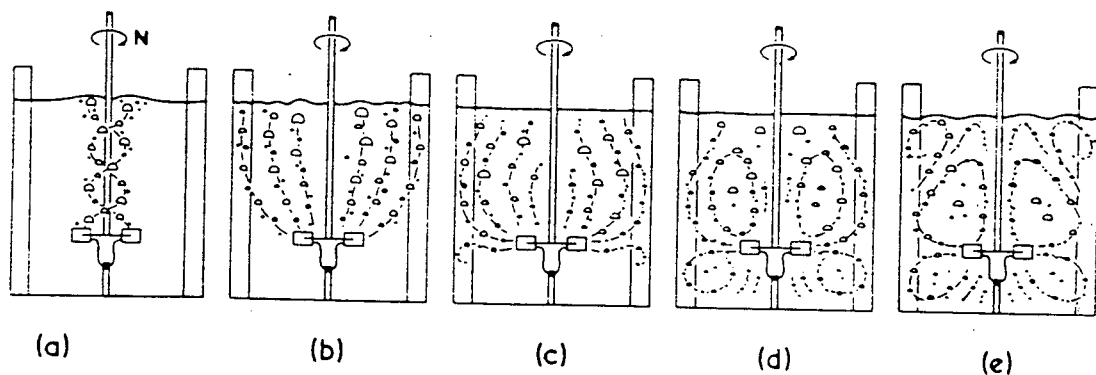
Figure 5.9   Bulk flow patterns with increasing N (a to e) or decreasing Q_G (e to a).   The transitions from (c) to (d) and (d) to (e) correspond to N_{CD} and N_R respectively [69].

5.4.2.2 Surface Aeration

Another method of gas-liquid contacting is achieved through plenum gas incorporation resulting from the interaction of agitator blades with the free liquid surface; the impeller behaves as a gas pump. This is referred to as "surface aeration".

Surface aeration methods are particularly important for elevated pressure processes with high reagent gas costs as in oxidative pressure leaching with pure oxygen. In these processes, gas bubble residence times may be too short to fully exploit the value of sparged gas bubbles. The loss of gas into the plenum space as one-pass bubbles, may represent substantial financial losses. Therefore, the rate of reincorporation via surface aeration is an important parameter and the agitator system used must be chosen carefully.

Boerma and Lankester [70] concluded that surface aeration not only may supplement mass transfer from conventional sparging methods, but may exceed sparged mass transfer rates. Some processes such as the Second Stage leach and Cominco's Zinc Pressure Leach rely solely on surface aeration methods to supply the dissolved gas demands needed for process objectives. Surface aeration methods are also practiced in waste-water treatment processes (ie. biochemical treatment of waste-water ponds). For such processes, the oxygen requirement is typically too large for compressed gas use because of the enormous scale of the system. The use of rotating brush aerators located near the static surface is common (Figure 5.10).
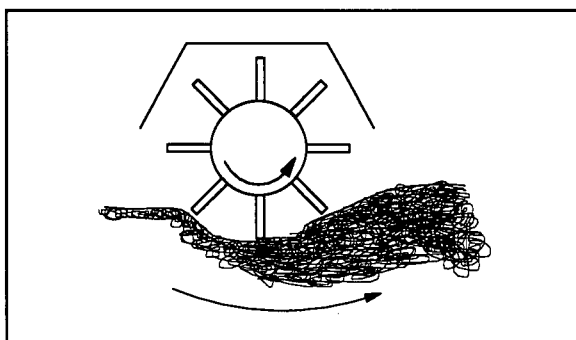
Figure 5.10   Rotating brush aerator [62].

<u>Mechanisms</u>

For conventional impeller systems, surface aeration is achieved through vortex draw-down action. The nature of these vortices and the rate of gas incorporation has been observed to be a function of impeller geometry, speed, position and the degree of baffling [71-76].

The mechanism of surface aeration in a fully-baffled vessel is depicted in Figure 5.11. Impeller turbulence generates cylindrical eddies at the surface which draws plenum gas down. Bubbles are created by shear forces at the tips of the vortices and are drawn into the impeller zone by fluid circulation. If high enough aeration rates occur, a significant drop in power will occur attributed to the formation of large clinging cavities behind the impeller blades.

In unbaffled tanks, surface aeration occurs by impeller draw-down of plenum gas by the central vortex (Figure 5.12). For partially baffled tanks, both mechanisms may occur.

(a) Plan View

(b) Side View
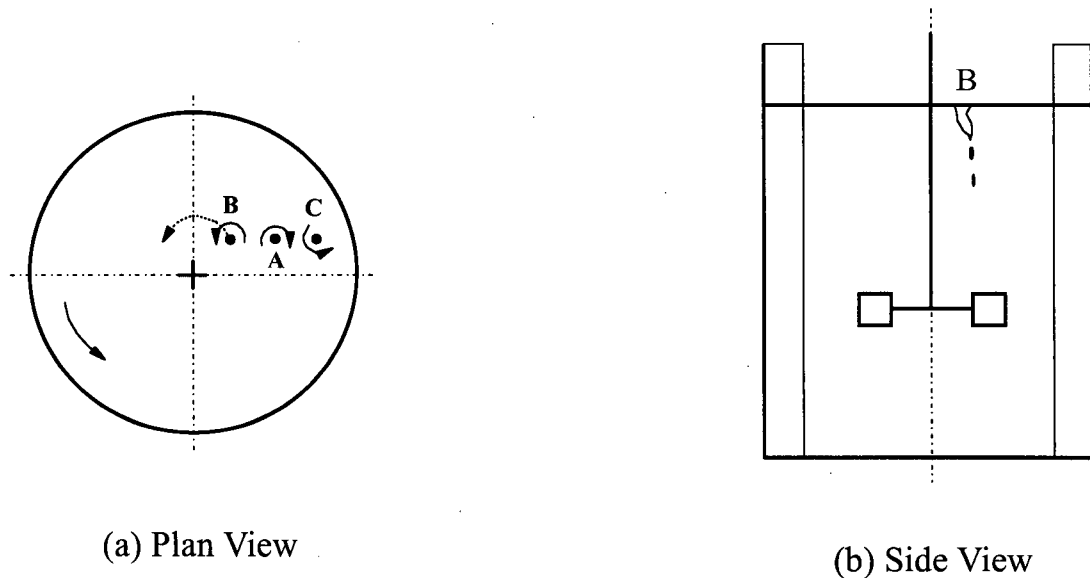
Figure 5.11   Mechanism of surface aeration in a fully-baffled tank [72].
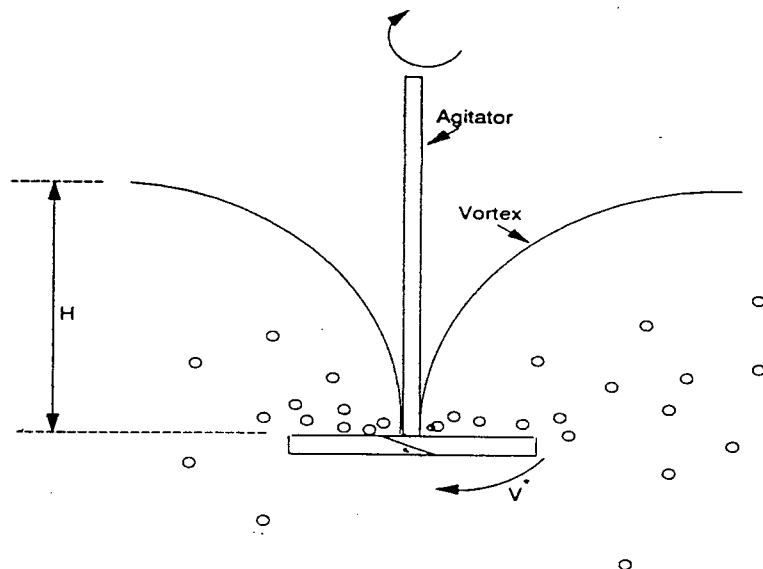
Figure 5.12   Mechanism of surface aeration by vortex action in a partially baffled or unbaffled tank [76].

Critical impeller speed

Degraaf [74] offered a simplified method of predicting the critical tip speed required for the onset of impeller gas-pumping. This method was based on a simple potential-kinetic energy balance at the tip of the agitator blade. The kinetic energy required to generate a bubble ($1/2mv^2$, m = mass of fluid displaced, v = ND) must equal the potential energy of the bubble generated at a depth H_I, equal to the immersion depth of the impeller (mgH_I). This resulted in the following expression:

$$v_C = (N_C D) = \frac{\sqrt{2gH_I}}{\alpha}$$

(5.14)

where α is a gas-pumping efficiency factor dependent on impeller type and equals one for an ideal impeller in an unbaffled system. Degraaf investigated this relationship using different impellers and found that the 6-bladed radial disk impeller ($\alpha = 0.86$) was more efficient at gas-pumping than the

4-bladed 45°pitch-down impeller (α = 0.61)

On inspection, equation 5.14 describes a critical Froude number requirement which has been discussed by other researchers [71, 77].

$$N_{Fr} = \frac{N^2 D}{g} > 2(H_I/D) \tag{5.15}$$

Similar correlations have also been developed to predict the critical speed for induction using gas-inducing type contactors. Such impellers are fabricated from hollow tubes joined in the shape of a 'T'. Joshi and Sharma [78] have predicted the critical speed to occur when the inertial forces generated by the impeller are sufficient to overcome the hydrostatic pressure of the fluid in the shaft:

$$N_C = \frac{1}{\pi D} \sqrt{\frac{2gH_I}{P'}} \tag{5.16}$$

where P' is a dimensionless quantity depending on impeller type and the outlet orifice position. Clearly, this equation is similar to equation 5.14 which is not surprising since the induction mechanism is very similar to vortexed aeration in an unbaffled tank.

Surface aeration studies

The bulk of the research on surface aeration phenomena has focussed on examining the critical speed requirements for surface aeration and resulted in empirical correlations relating critical speeds to impeller and tank geometries (D/T, H_I/T, C/T) and fluid properties (ρ, μ, σ). Veljkovic et al. [73] have conveniently summarized much of the work done up to 1991.

Swiniarski [75] and Dawson-Amoah [76] of UBC have investigated extensively surface aeration phenomena under unsparged conditions. The objectives of Swiniarski's work were to investigate further Degraaf's critical tip speed correlation (equation 5.14) and to investigate the role of baffling on surface aeration gas-liquid mass transfer phenomena. This was done in a 200 L unbaffled, vertical cylindrical vessel using a variety of impeller speed, sizes and positions. A large tank diameter and unbaffled conditions were employed to simulate the free rotation of an impeller in the ocean. The work resulted in several significant conclusions:

1. The 6-bladed radial disk impeller was more efficient at pumping gas than a 4-bladed axial flow updraft impeller under unbaffled conditions

2. Provided that a stable central vortex could be sustained, the use of baffles greatly increased surface aeration mass-transfer rates over unbaffled vessels. This condition was met using small impellers rotating at very low liquid coverages. For the radial disk impeller, an increase in mass transfer rate by 3-6 times was found over the unbaffled case (Figure 5.13).

3. The increases in power draw under baffled conditions rose at a faster rate than increases in mass transfer in the range of velocities and impeller depths studied.

Effect of Baffles on K_G^{20}

(a) K_G^{20} Without Baffles

(b) K_G^{20} With Baffles
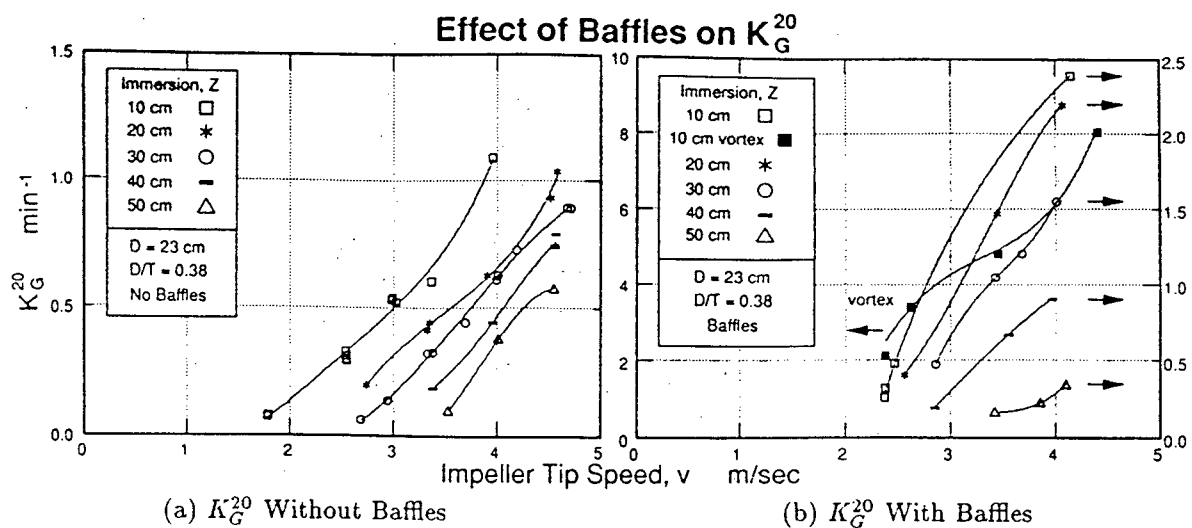
Figure 5.13   The effect of baffles on oxygen mass transfer rates (K_G^{20}) [75].

Dawson-Amoah [76] investigated similar parameters in a scale-model of the first compartment of Cominco's Zinc Pressure Leach autoclave. The vessel shape resembled a horizontal, cylindrical vessel bounded on one side by a hemispherical dish (outward) and by a vertical wall on the other. It was shown that the asymmetric geometry of the vessel provided adequate baffling effects which resulted in an increase in mass transfer over an unbaffled vertical cylindrical tank by a factor of 3.6 times. This increase was on the order of Swiniarski's fully baffled symmetrical tank (3-6 times). As expected, an increase in power, by 20-40 times was also found.

Adding baffles to the asymmetric tank resulted in two effects: at low impeller coverages (<11.5 cm), increases in the mass transfer rates were obtained; at high impeller coverages (>16.5 cm) reductions in mass transfer rates were obtained. This was attributable to the increased difficulty in vortex formation with increasing impeller coverages, at a given agitation rate.

Dawson-Amoah found that the 6-bladed radial disk impeller achieved significantly higher gas-liquid mass transfer rates (~ 3 times) over the 4-bladed 45° updraft impeller. Of the three types of impellers investigated, the 4-bladed 45° downdraft impeller was found to be the least effective in gas-liquid mass transfer performance.

5.5   Oxygen Mass Transfer Rate Measurement Techniques

Oxygen mass transfer into liquid may be measured by either physical or chemical methods. An excellent review describing methodologies and limitations of these techniques is given by van't Riet [80].

Of the physical methods, the *dynamic gassing-out method* appears to be most reliable. The procedure involves deoxygenation of the solution with an inert gas (eg. N_2), followed by oxygen absorption, the rate of which is monitored by a polarographic electrode (Clark cell). The limitations of this technique can be attributed to the electrode performance. Contact of the electrode with gas bubbles may result in too high a measurement as the concentration in the gas phase may be inadvertently measured. Also, incorrect readings may result from slow electrode response time, mainly attributable to slow diffusion rates through the membrane.

Chemical methods for oxygen $k_L a$ measurements are based on the reaction of dissolved oxygen with a reduced aqueous species. Historically, chemical methods have been employed more frequently than physical methods because of their greater simplicity and cost effectiveness. However, chemical methods are generally considered to be prone to greater inaccuracies.

For $k_L a$ measurements via chemical methods, restrictions on the reaction rate of the governing oxidation reaction must be met. If the reaction rate is too slow, the dissolved oxygen concentration in the bulk may become significant and reduce the concentration gradient driving force:

$$R_{O_2} = k_L a \left(C_{O_2}^* - C_{O_2}^b \right)$$

(5.17)

Consequently, the determination of C^b_{O2} must be made. Conversely, if the reaction rate is too fast, the reaction of oxygen may occur appreciably within the boundary layer leading to chemically enhanced O_2 absorption rates which result in artificially high $k_L a$ measurements. Therefore, for accurate $k_L a$ measurements, the reaction rate must be slow enough so that oxygen diffusion can proceed across the full boundary layer thickness yet fast enough to keep the bulk concentration close to zero.

A dimensionless parameter called the *Hatta* number has been used to indicate the effect of the chemical reaction rate on the overall mass transfer rate [81]:

$$Ha = \frac{1}{k_L} \sqrt{\frac{2}{m+1} K_{mn} D_A C_A^{m-1} C_B^n}$$

(5.18)

where K_{mn} is the reaction rate constant and m,n are the reaction order of species A and B respectively. The concept of the Hatta number is based on film theory and essentially represents the ratio between the maximum possible conversion rate and the maximum diffusion rate in the film [59]. The concentration profiles within the vicinity of the boundary layer for different Hatta numbers are shown in Figure 5.14.
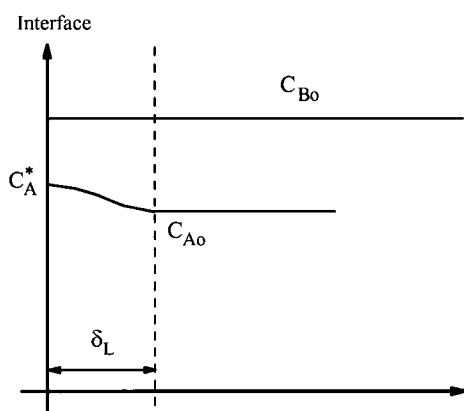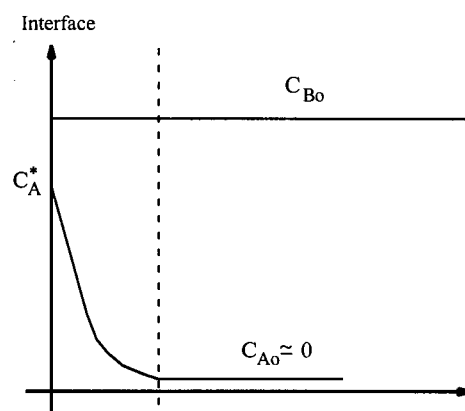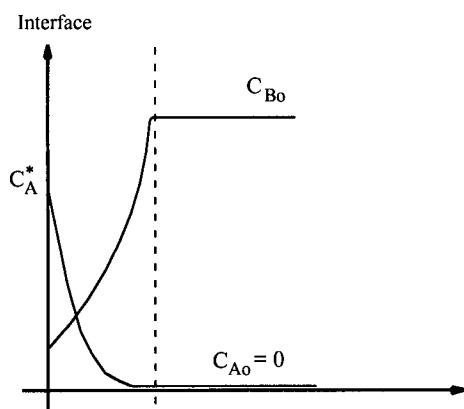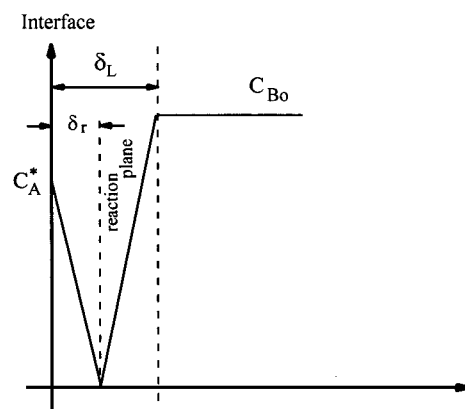
Figure 5.14 Liquid-phase concentration profiles for mass transfer with chemical reaction for various chemical reaction rates [81].

For chemical methods, reactions yielding Hatta numbers within the range $0.02 < \text{Ha} < 0.3$ (Figure 5.14b) are required.

5.5.1 Sulfite Oxidation Method

The sulfite oxidation method has been the most frequently used chemical method for oxygen $k_L a$ measurements. The overall reaction is as follows:

$$SO_3^{2-} + \frac{1}{2} O_{2\,(aq)} \overset{Co^{2+}}{\Longrightarrow} SO_4^{2-} \qquad (5.19)$$
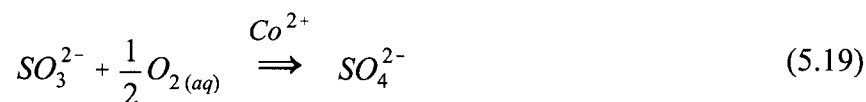
Because the SO_3^{2-}- O_2 reaction is by itself too slow in distilled water (Ha < 0.02), a cobalt (Co^{2+}) catalyst is required. Alternatively, cupric ions (Cu^{2+}) have also been found to catalyse this reaction. Oxygen mass transfer rates are then obtained by monitoring the rate of sulfite depletion which may be done by titrimetric methods [82].

The kinetics of the sulfite oxidation reaction is given by the following expression

$$R_{O_2} = K C_{O_2}^m C_{SO_3^{2-}}^n C_{Co^{2+}}^r \qquad (5.20)$$

where K is the reaction rate constant and (m, n, r) refer to reaction orders of the species. Operation within the zero order kinetics range for sulfite (n=0) is practiced. This prevents the depletion of sulfite due to oxygen reaction from having any effect on the reaction rate measured. The sulfite depletion rate will then be constant over the duration of the experiment, facilitating the determination of the oxygen mass transfer rate. However, as illustrated in the extensive review of sulfite oxidation kinetics by Linek and Vacek [83], much discrepancy in the reported zero-order concentration range appears in literature. Degraaf [74], Swiniarski [75] and Dawson-Amoah [76] have all employed 0.02 M initial sulfite concentrations. However, apart from these studies, zero-order kinetics for sulfite at such low concentrations have not been frequently reported. Krause [84] has observed zero-order kinetics within the sulfite concentration range of 0.4 - 0.02 M. Most other studies reported in Linek and Vacek's review [83] have indicated that zero-order kinetics require a minimum of 0.2 M sulfite with 0.8 M being the normal initial concentration.

For cobalt, which does not get consumed in the reaction, a reaction order of 1 has been generally reported. For oxygen, the reaction order (m) appears to vary according to its partial pressure in the gas phase. Reaction orders of 2 and 1 have been reported for oxygen in air and pure oxygen respectively, both under ambient conditions. Reaction orders of 1 have been reported for $C^*_{O2} \geq 7 \times 10^{-4}$ M which corresponds to $P_{O2} \geq 0.6$ atm [83].

The poorly understood kinetics of the sulfite reaction makes comparison of data from different sources extremely difficult. In addition to reaction rate order dependence on concentrations, such factors as pH, temperature and even sulfite purity have been reported to affect reaction kinetics [80].

Another disadvantage to the sulfite method is its ionic form. As discussed in a previous section (Section 5.4.1), the presence of dissolved ionic salts can have a significant effect on the average bubble size (an order of magnitude reduction). As $a = 6\varepsilon_G/d_B$ (equation 5.12), the oxygen mass transfer rate into a sulfite solution will therefore be higher than in pure water. As a consequence, results obtained by this method **may not** be correlated to a pure water system. In addition, the preservation of the total ionic strength of the system is imperative. Any attempt to replenish the depleted SO_3^{2-} concentration from run-to-run with fresh sodium sulfite may significantly affect results. This implies that it is dangerous to compare results from studies using different initial sulfite concentrations.

However, as a measurement technique, the sulfite oxidation method has several advantages: a lack of toxicity; cost-effectiveness; a well-established method for sulfite depletion analysis, and ease of implementation in large-scale testwork. This was the method employed in the current study.

Chapter 6

Experimentation

6.1 Research Objectives

The objective of this research was to evaluate the gas-liquid mass transfer/mixing performance in the Second Stage leach process through the use of a scaled version of the plant autoclave. Ways to improve the existing performance were studied by changing both design and operating conditions of the autoclave model. Specifically, conversion of the impeller types from an axial down-draft system to a radial disk system was investigated. As discussed in Chapter 5, previous UBC studies [73-75] have shown radial disk impellers to be superior in gas-liquid mass transfer performance than 45°pitch blade impellers largely due to increased shear stress and turbulence generated. The experimental work for this research work was performed at the University of British Columbia.

6.2 Experimental Variables

The variables investigated in this study were:

1) **Impeller Type**. Two different impeller types forming three dual impeller systems were studied: i) 4-bladed axial flow down-draft system (AD); ii) 6-bladed radial disk system (RR); and iii) a radial disk(top)/axial combination system (RA). Current plant practice employs a 4 blade dual-axial down-draft configuration (Figure 2.2).

2) **Tank Internal System**. The effect of the internal configuration of the tank and mass transfer/mixing performance was investigated. The systems studied were: i) an unbaffled tank; ii) a baffled tank (4 vertical baffles), and iii) cooling coil simulation (modelled Second Stage autoclave).

3) **Agitation Rate**. The relationship between surface aeration rates and impeller rotational frequency was investigated. The frequencies used were: 121, 171, 221 and 271 rpm. Where 271 rpm was unattainable due to excessive splashing, a speed of 246 rpm was used.

4)   **Fluid fill level**. A series of tests using different fill levels were performed to determine the effect of fill height on surface aeration rates. Levels of -10%, -5%, 0%, +5% and +10% (linear distance) above the scaled current operating level were examined.

6.3   Apparatus

The analysis of oxygen incorporation/mixing performance was performed in a geometrically scaled plexiglass model of the INCO Second Stage autoclave. The scaling factor was 1:5.8. The power required by the system was supplied by a 3 h.p. Toshiba 3-phase induction motor. The motor was equipped with an SKK gear reducer which lowered maximum output rpm from 1720 down to 640 rpm (1:2.734). Accurate agitation control from 0 to 640 rpm was provided by a variable speed drive unit (Toshiba High Performance Transistor Inverter).

Power draw measurements were made using an OMEGA rotary torque sensor. Data acquisition of power draw was made using the Labtech Notebook software package. A schematic representation of the overall setup is shown in Figure 6.1. Main components are depicted in Figures 6.2 - 6.5 and are described briefly below.

6.3.1   Mixing Vessel

The mixing vessel used in the modelling studies was fabricated out of 1.27 cm (1/2") thick clear plexiglass. The maximum capacity of the vessel was roughly 190 L including a 20 L capacity dished bottom. The dimensions of the vessel are given in Figure 6.2. A frame constructed out of 5 cm (2 ") wide hollowed steel beams was used to support the vessel. A plexiglass cover was used to seal the vessel in order to maintain a high level of oxygen in the plenum space and to prevent loss of fluid due to splashing. Sampling holes were made in the lid for solution and gas sampling. The gas sampling hole was fitted with a septum for syringe extraction. Additional holes were drilled into the lid to allow oxygen gas introduction into and exit out of the plenum space.

6.3.2   Internals

6.3.2.1 Cooling Coils

The double meandering cooling coil system used in the Second Stage autoclave was

simulated using forty-eight 1.27 cm diameter plexiglass rods 54 cm in length(Figure 6.3). The rods were arranged concentrically, spaced 30° apart and mounted on a removal support frame.

6.3.2.2 Baffles

Vertical baffles used in baffled tank studies consisted of 4 plexiglass plates 0.8 cm thick and 54 cm long (Figure 6.4). The widths of the baffles were 6 cm giving a B/T = 1/10 and were arranged 90° apart as specified by standard convention (Figure 5.1). The removable baffles were mounted by screws onto baffles supports with a wall offset ratio of T/70.

6.3.3   Impellers

A scaled version of the dual 45° pitch-down impeller system currently used in INCO's Second Stage leach process was created out of 0.32 cm (1/8") thick mild steel coated with paint to prevent corrosion. The impellers were 27.4 cm in diameter and 5 cm in blade width.

To study the performance of a radial disk impeller system, two 6-Blade radial disk turbines were constructed having the same blade diameter, width and thickness as the pitch down system. The fabricating material used was 316 stainless to avoid the need for paint protection. Schematic representations of the impellers used in the scaled model study are depicted in Figure 6.5.

The impellers were mounted with set screws onto a 1.9 cm (3/4 ") diameter 316 stainless steel shaft. Horizontal deflection of the impeller shaft was prevented by a teflon bearing located on the bottom of the vessel.
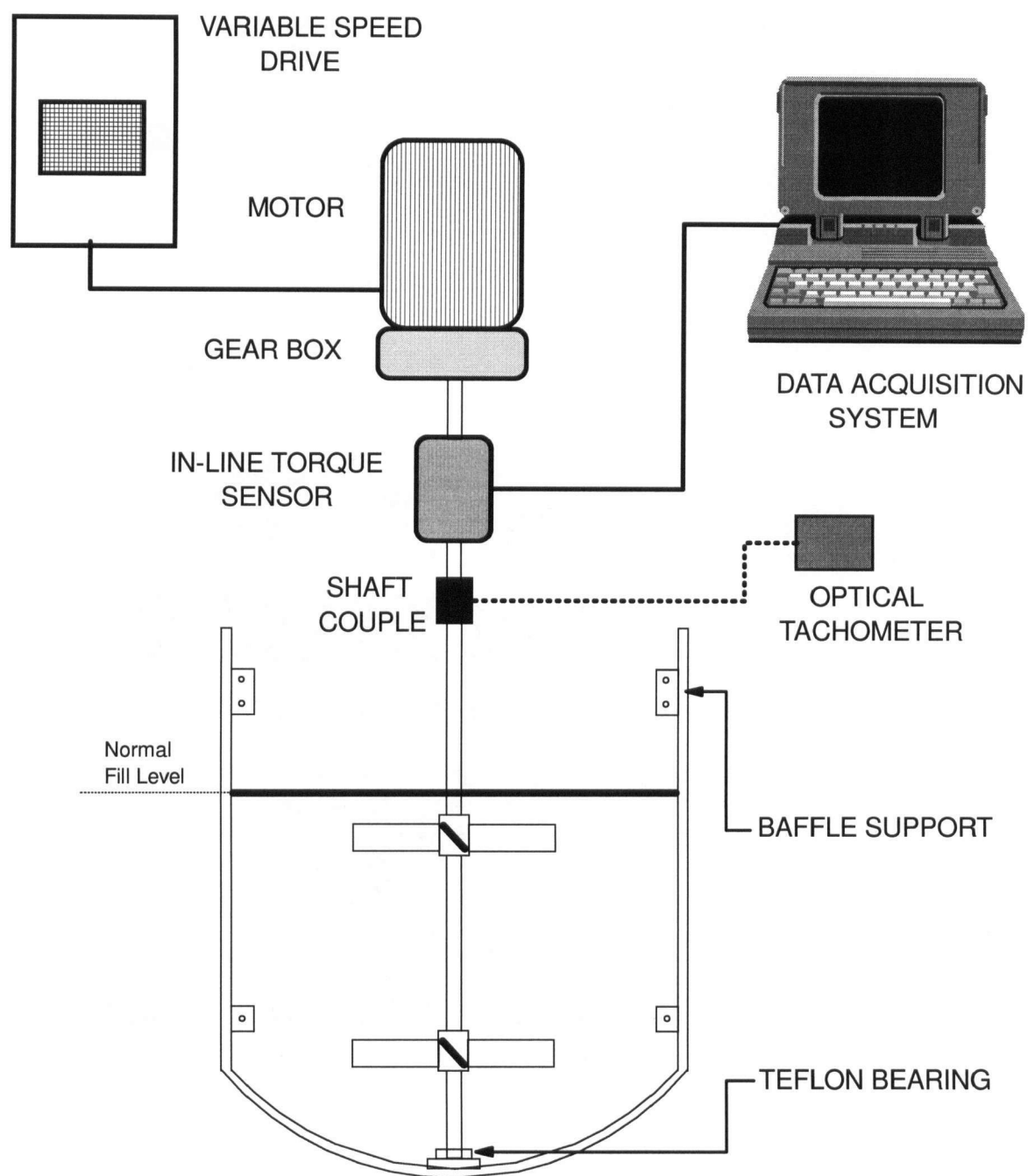
Figure 6.1   Overall set-up used in the mass-transfer/mixing experiments.

Figure 6.2   The scaled autoclave model and its dimensions.
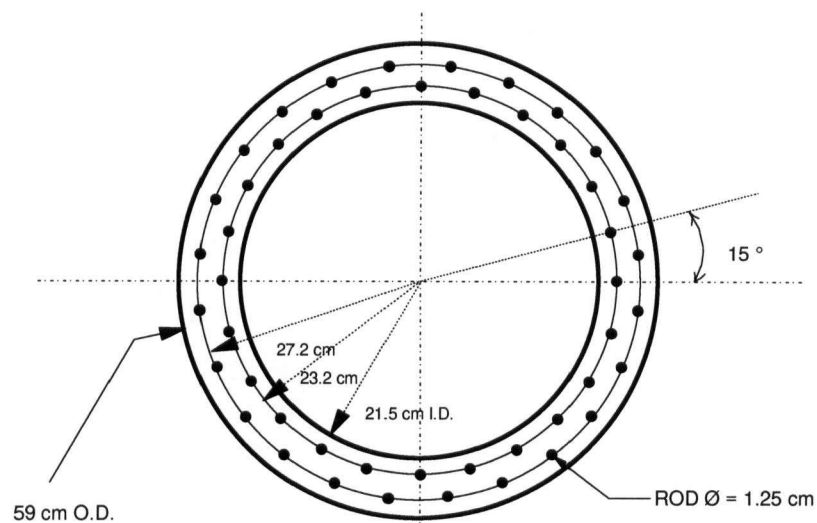
a) Top View of Cooling Coil Support Ring

59 cm O.D.

27.2 cm

23.2 cm

21.5 cm I.D.

15 °

ROD Ø = 1.25 cm
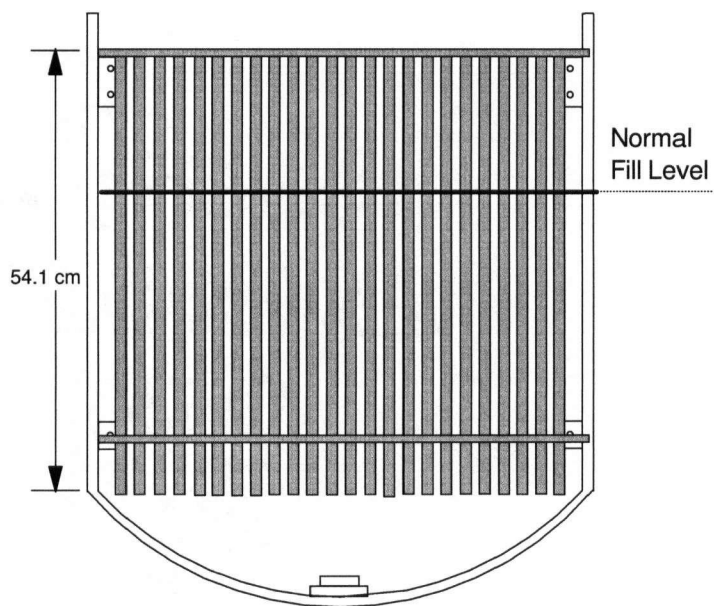
b) Front View of Vessel with Cooling Coils

Normal
Fill Level

54.1 cm

Figure 6.3   Model of the cooling coil system.
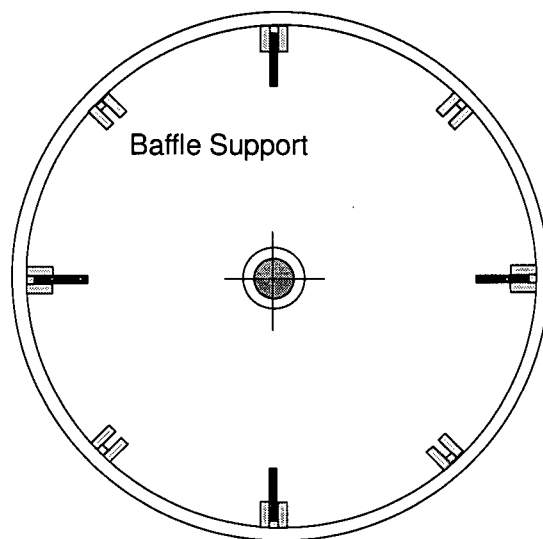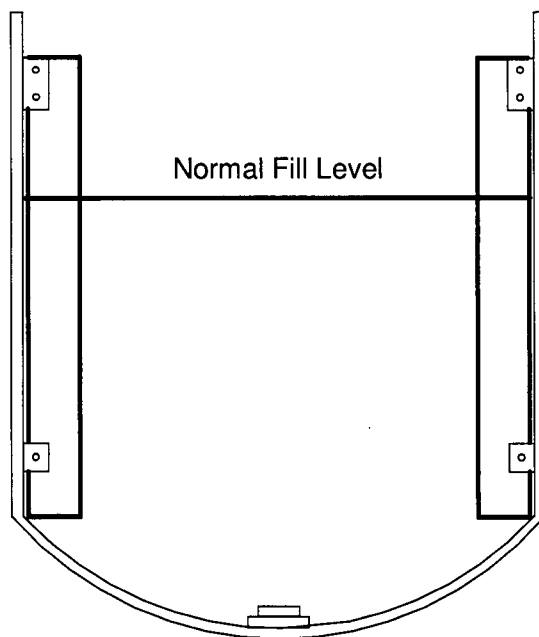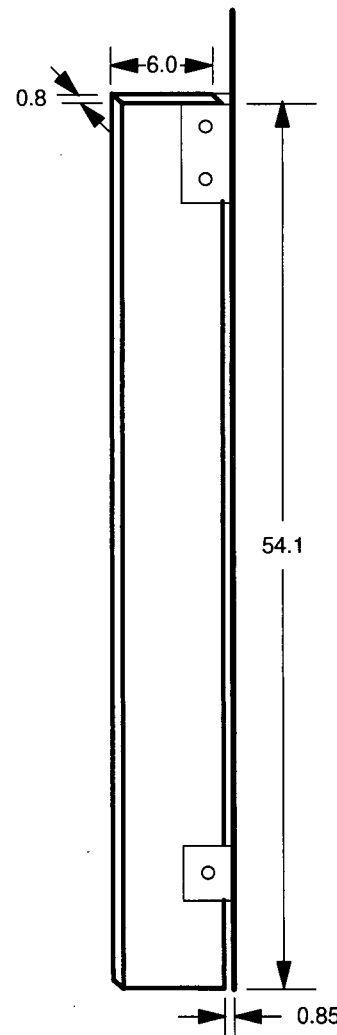
Figure 6.4   Standard vertical baffles (B = T/10).
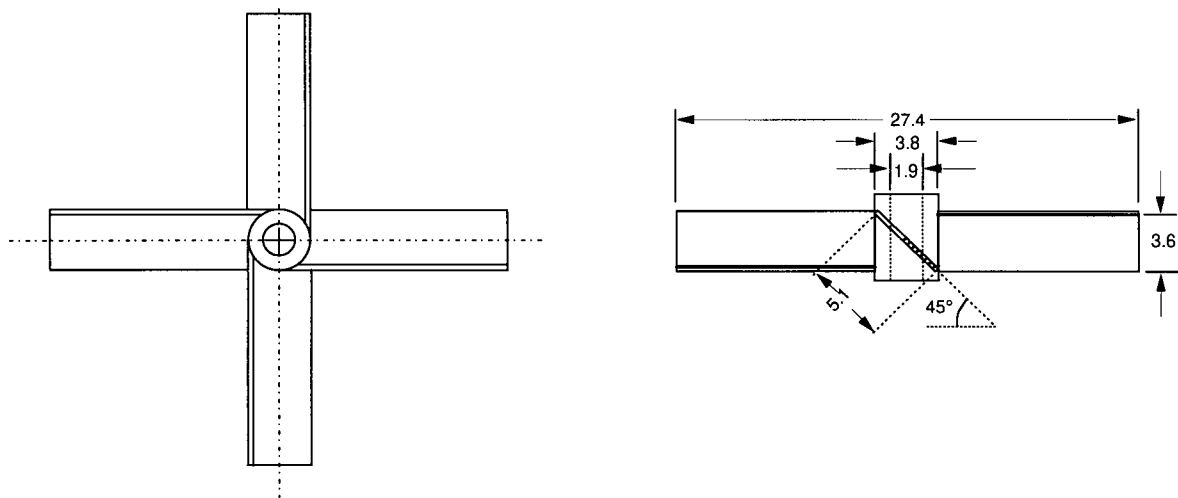
A) 4-Bladed Axial Down-draft

All Dimensions in cm
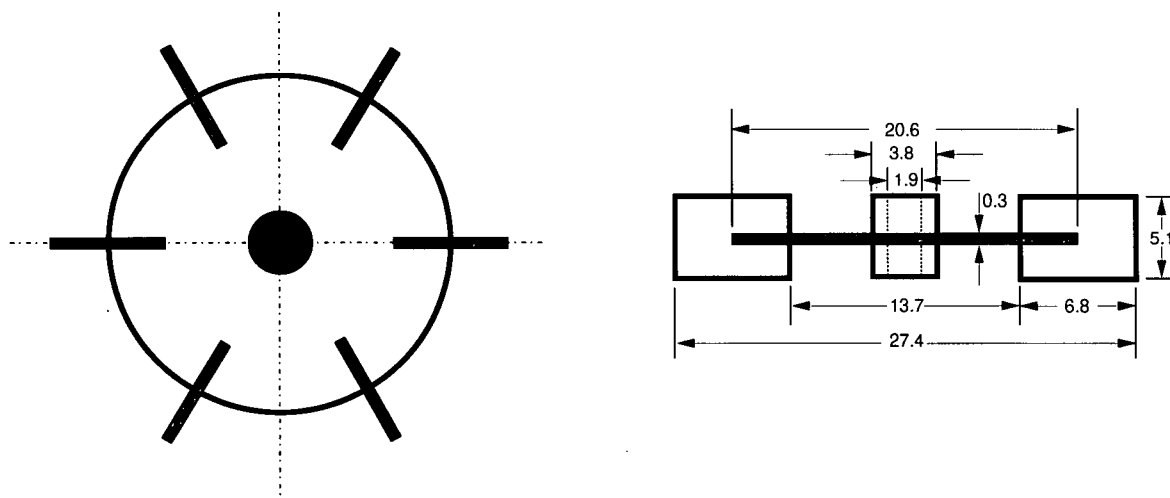
B) 6-Bladed Radial Disk

Figure 6.5   Impellers used in the investigation.

6.4 Reagent Preparation and Standardization Procedures

With the exception of sodium sulfite, all chemical reagents used were of analytical grade. Commercial grade anhydrous sodium sulfite was supplied by the Rhône-Poulenc Chemical Company. All solutions were made by reagent dissolution in deionized water.

The concentrations of sodium sulfite and cobalt catalyst used in all tests were 0.254 mol/L and 1.70×10^{-4} mol/L (10 mg/L) respectively. For standard volume conditions (125 L), the required reagent weights were 4000 g Na_2SO_3 (126.04 g/mole) and 5.96 g $CoSO_4 \cdot 7H_2O$ (281.10 g/mole).

Titrimetric analyses required 0.1 mol/L iodine solution (prepared from stock 0.5 mol/L iodine), 0.2 mol/L sodium thiosulfate solution and 0.02 mol/L (3.6 g/L) KIO_3. The KIO_3 crystals were dehydrated in a drying oven at 120°C for at least 24 hours prior to use. This was required because KIO_3 was used as a primary standard for thiosulfate determination, and therefore, any absorbed moisture had to be removed prior to weighing. The KIO_3 crystals were weighed to four decimal place accuracy.

Standardization of thiosulfate was performed using a solution containing 25 mL of the 3.6 g/L KIO_3 solution, 1 g KI and 10 mL of 1M HCl. On addition of KI and HCl to the potassium iodate solution, I_2 was immediately formed (stoichiometrically to IO_3^-) according to:

$$IO_3^- + 5I^- + 6H^+ \rightleftharpoons 3I_2 + 3H_2O \tag{6.1}$$
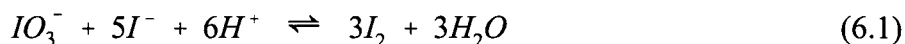
The iodine produced was titrated against the thiosulfate solution to determine thiosulfate concentration.

$$2S_2O_3^{2-} + I_2 \rightleftharpoons S_4O_6^{2-} + 2I^- \tag{6.2}$$
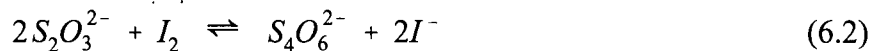
The thiosulfate solution could then be used as a titrant to standardize the 0.1 mol/L iodine solutions. For this standardization, acidification of the iodine solution (1 mL of 1M HCl) was required to prevent the reaction of iodine with hydroxyl ions present in the thiosulfate solution.

$$I_2 + 2OH^- \rightleftharpoons I^- + IO^- + H_2O \tag{6.3}$$
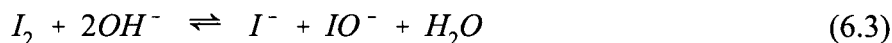
The standardization procedures were obtained from *Vogel's Textbook of Quantitative Chemical Analysis* [82]. All standardizations were done in duplicate.

6.5 Experimental Procedure

6.5.1 Start-up and Sampling

Predissolved Na_2SO_3 and $CoSO_4 \cdot 7H_2O$ were added to deionized water to make up a total volume of 125 L. The contents were then slowly blended for at least 15 minutes to ensure complete mixing of the added reagents. During this time, dissolved oxygen initially present in the water was observed to have been scavenged using a dissolved oxygen probe and system temperature stabilization was achieved. Oxygen gas flow was initiated into the plenum space and continued thereafter. This was done to ensure that a high level of oxygen was maintained in the plenum space gas during the duration of the tests.

Agitation was started and power draw was monitored. After stabilization of the power draw, the sampling procedure was started. Sampling times varied according to the rate of oxygen transfer into solution. Typically, the interval was such that 10-12 samples were taken during the duration of the experiment. For consistency, all samples were withdrawn from the same depth in the fluid system. Because of the reactivity of the sulfite-oxygen system, care was taken to minimize solution exposure to air. Argon purged sample containers were used at all times. Sample solutions were stored stoppered under an argon bath until analyses.

Four plenum space gas samples were extracted during the course of each run for oxygen analysis by gas chromatography. This was done using 60 mL syringes. Analysis was performed using a PYE series 104 chromatograph. The oxygen level quoted for the experiment was based on an average of the four samples.

6.5.2 Oxygen Transfer Rate Determination by Titrimetric Analysis

The rate of oxygen transfer into solution was measured by the chemical method of cobalt-catalyzed sulfite oxidation. The reaction mechanism is described by:

$$SO_3^{2-} + \frac{1}{2}O_{2(aq)} \overset{Co^{2+}}{\Longrightarrow} SO_4^{2-} \tag{6.4}$$
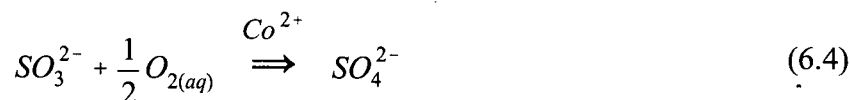
Oxygen transfer rates were then related to sulfite depletion rates according to the stoichiometry of the above reaction:

$$\left(\frac{dC_{O_2}}{dt}\right) = \frac{1}{2}\left(\frac{dC_{SO_3^{2-}}}{dt}\right) \tag{6.5}$$

In order to determine the rate of sulfite depletion, analyses of sulfite concentrations were made by the method of iodine-back titration [82].

For each sulfite sample withdrawn, 5.0 mL of the solution were pipetted into 20.0 mL of 0.1mol/L (standardized) acidified iodine solution. Care was taken to minimize sulfite solution exposure to air during pipette drainage. Solution addition was effected under gently stirred conditions. To ensure complete reaction, at least 15 minutes were allowed to elapse before titrimetric analysis was initiated.

The amount of iodine used was in excess of the stoichiometric amount required to oxidize sulfite to sulfate. The reaction is given by:

$$(1+X)I_2 + SO_3^{2-} + H_2O = 2I^- + SO_4^{2-} + 2H^+ + XI_2 \tag{6.6}$$
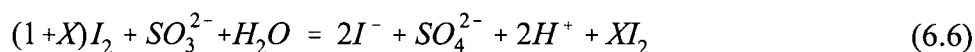
The excess amount of iodine remaining(X) was determined by titration with a standardized 0.2 mol/L sodium thiosulfate solution. The amount of iodine reacted was then back-calculated from the determined excess. From the stoichiometry of the iodine-sulfite reaction, the amount of iodine reacted is equivalent to the amount of sulfite present in the sample. The change in sulfite concentration with time was then equated to the transfer of oxygen into solution by equation 6.5. Consequently, by monitoring the depletion of sulfite with time, the rate of oxygen transfer into solution was determined. A typical oxygen transfer rate curve is shown in Figure 6.6.
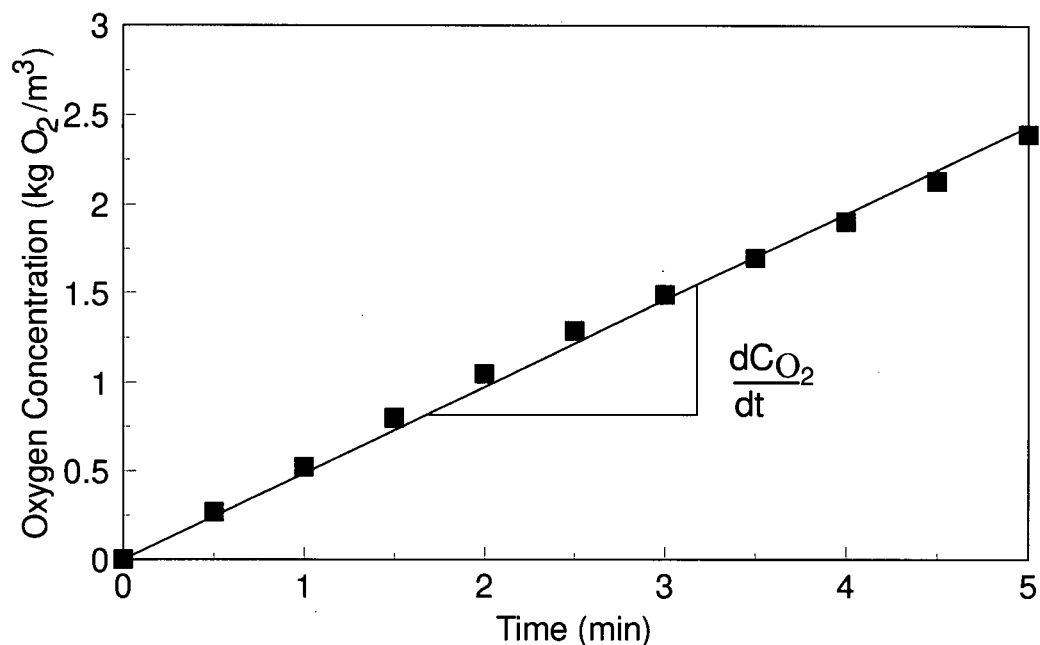
Figure 6.6 Typical oxygen transfer rate curve obtained from sulfite-oxidation method.

The sulfite concentration of 0.25 M was employed in this study. Deviations from linearity in the sulfite depletion (oxygen consumption curve) suggesting non-zero order kinetics were observed for residual sulfite concentrations below 0.05 M. Consequently, oxygen mass transfer rates were based on the linear regression slope between 0.25 - 0.05 M residual sulfite.

6.5.3 Power Draw Calculation

The following relationships enabled impeller power draw to be calculated from the shaft torque as measured by the OMEGA rotary torque sensor:

$$P = (F \times d) \times \omega$$
$$= Tq \times \omega \qquad (6.7)$$

where Tq is the torque draw (in N•m), and ω is the angular velocity (in rad-s^{-1}). The torque sensor measured torque as an electrical signal (mV) which was continuously recorded by the acquisition

system. To convert the signal to conventional SI units of torque, a system specific conversion factor of 2.0923 N•m/mV was required. The angular velocity was found from the impeller rotational frequency (in rpm) according to:

$$\omega = \left(\frac{2\pi N_{rpm}}{60} \right)$$

(6.8)

In power draw calculations, the average value of the torque over the duration of the experiment was used. For fluid mixing power draw, the average operating power draw was corrected by subtracting the average power required to run the impellers in air.

Chapter 7

Results and Discussion: Gas-Liquid Mass Transfer/Mixing Tests

7.1   Preliminary Comments

7.1.1   Use of Pure Oxygen

If not corrected for, variations in air composition can result in incorrect oxygen mass transfer rate measurements using both chemical and dynamic methods [85]. For the sulfite-oxidation method, air is susceptible to oxygen depletion as oxygen concentrations in the bulk are kept at low concentrations by chemical reaction, thereby maintaining a significant driving force for diffusion. With oxygen depletion, P_{O2} becomes less than 0.21 atm, resulting in C^*_{O2} values below the assumed 8 mg/L at saturation. This problem becomes more significant as the residence times for bubbles increase [80]. Degraaf [74] found oxygen levels dropped to $P_{O2} = 0.13$ atm in the reacted bubbles. Grewal [86], measuring mass transfer rates in an AGR system (Advanced Gas Reactor) found that escaping air bubble composition dropped to as low as $P_{O2} = 0.04$ atm. This was attributed to the longer residence times of gas in such a high-aspect ratio reactor. Preliminary measurements in the current investigation determined oxygen concentrations of $P_{O2} = 0.12$ atm, close to Degraaf's system.

One method to correct for this phenomena is to constantly measure representative gas compositions. Another method is to use a pure source of oxygen in the free space, to minimize P_{O2} variations. In this investigation, the latter method was adopted. Though pure oxygen levels were not fully realized, P_{O2} in all tests exceeded 84% (avg. 89 ± 5%), for which negligible depletion was assumed. Both Swiniarski [75] and Dawson-Amoah [77] did not account for oxygen depletion effects which suggests that the mass transfer rates quoted in these studies were slightly too low.

7.1.2   The Effect of Sulfite and Temperature on Oxygen Saturation (C^*_{O2})

Based on available published literature, Linek and Vacek [83] have offered the following empirical correlation relating C^*_{O2} with Na_2SO_4 concentration and temperature:

$$C^*_{O_2} = 5.909 \times 10^{-6} \exp\left(\frac{1602.1}{T} - \frac{0.9407 C_{Na_2SO_4}}{1 + 0.1933 C_{Na_2SO_4}} \right) \times P_{O_2} \quad (mol - L^{-1}) \quad (7.1)$$

where C is in mol-L^{-1} and T is in K. This correlation is applicable for: $0 < C_{Na2SO4} < 1$ M, and 288K (15°C) $< T <$ 308 K (35°C), which is within the range used in this investigation. In this correlation, it has been assumed that the oxygen solubility in a Na_2SO_4 solution is identical to that of a Na_2SO_3 solution. At 298 K, for $C_{Na2SO4} = 0.25$ M, the % difference in C^*_{O2} between correlated prediction (10.18×10^{-4} mol/L) and experimental measurement (10.22×10^{-4} mol/L) was less than 0.4% [83]. A plot of equation 7.1 showing the variation in C^*_{O2} (in mg/L) with temperature for different concentrations of Na_2SO_4 is given in Figure 7.1.
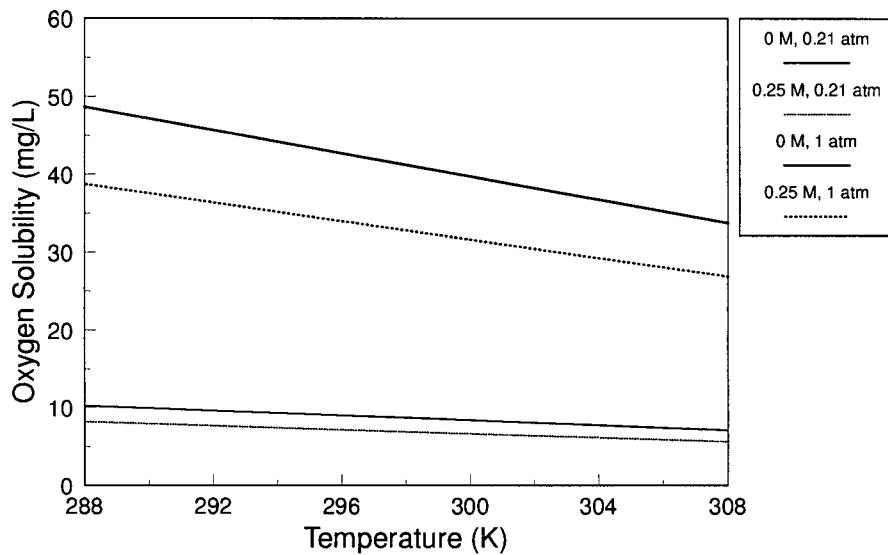
Figure 7.1   Effect of temperature and Na_2SO_4 concentration on oxygen solubility in water using correlation of Linek and Vacek [83]. Limits of correlation: 288 K $< T <$ 308 K; 0 M $< C_{Na2SO4} < 1$ M.

This correlation was used in the evaluation of the mass transfer rate expression:

$$R_{O_2}(T) = k_L a \left(C^*_{O_2}(T) \right) \qquad (7.2)$$

7.1.3   Modelling Approach

The precise modelling of multi-phase mixing action in a scaled agitated tank is viewed by many to be virtually impossible [53,58-59]. The hydrodynamics involved are too complex to account for all possible interactions. The difficulties are compounded with the addition of gravitational effects (N_{Fr}) and interfacial effects (N_{We}), such as those involved in gas-liquid mass

- 112 -

transfer-surface aeration processes. As discussed by Treybal [59] to maintain dynamic similarity in a geometrically similar but unequally sized vessel operating with a vortex, both N_{Re} and N_{Fr} must be maintained. For different sized impellers, specification of the impeller speed in the model is not possible using the same fluid, as equal Reynold's and Froude numbers require the following conditions to be met:

$$N_{Re} \quad \Rrightarrow \quad \frac{N_1}{N_2} = \left(\frac{D_2}{D_1}\right)^2 \qquad\qquad (7.3)$$

$$N_{Fr} \quad \Rrightarrow \quad \frac{N_1}{N_2} = \left(\frac{D_2}{D_1}\right)^{0.5} \qquad\qquad (7.4)$$

Therefore, most mixing studies have implemented fully baffled conditions to eliminate gravitational effects. This was not possible for the current investigation because of the governing conditions involved in the Second Stage leach process (Section 2.2).

Oldshue [53] describes that some three-phase processes such as oxidative leaching and fermentation, cannot be correlated with dimensionless groups and other methods must be found for scaling. His general recommendation in such cases was to maintain: 1) geometric similarity and 2) power per unit volume (P/V), which under fully turbulent condition (N_P = constant) reduces to:

$$\frac{P}{V} \quad \Rrightarrow \quad \frac{N_1}{N_2} = \left(\frac{D_2}{D_1}\right)^{2/3} \qquad\qquad (7.5)$$

As done by Swiniarski [74] and Dawson-Amoah [76], this method was adopted for the current investigation, which yielded the scaled agitation rate of 221 rpm (versus 68 rpm for industrial vessel). It must be cautioned that this speed corresponds to the case involving 0.25 M sodium sulfite solution, and not the three-phase system employed in practice. Therefore, discussion of results will stress relative changes and not absolute values obtained in the model studies. As a further measure, additional speeds (±50 rpm increments) were employed to assess the trend of results to prevent conclusions drawn based on the scaled speed alone.

7.2 Oxygen-Mass Transfer Studies in the Scaled Model (Cooling Coils)

This series of experiments focussed on assessing the effect of impeller type, rotational speed and positional geometry on the gas-liquid mass transfer/mixing performance in the scaled Second Stage autoclave model. Performance was judged based on $k_L a$, power draw and the ratio of R_{O2} to power draw. This ratio (abbreviated ME) corresponds to moles of oxygen transferred per joule of energy input (mol O_2-J^{-1}) and was normalized at $25\,^\circ C$ using $C^*_{O2}(25\,^\circ C)$ for comparative purposes. Detailed results are presented in Appendix II-A. As shown in Table 7.1, turbulent conditions were encountered in the impeller zone for all agitation speeds employed.

Table 7.1 - Impeller Reynold's number at agitation speeds employed

N (rpm)	N (rev-s^{-1})	N_{Re} x 10^4 ($ND^2\rho/\mu$)
121	2.02	15.1
171	2.85	21.3
221	3.68	27.7
246	4.10	30.8
271	4.52	33.9

D = 0.274 m, ρ = 1000 kg-m^{-3}, μ = 0.001 Pa-s

7.2.1 Effect of Impellers

The effect of changing impeller systems from the current dual axial-downdraft system to that involving radial disk impellers are summarized in Figures 7.2 to 7.4. In all experiments, the presence of a central vortex was observed which indicated that the system was in a partially baffled state; consequently, gravitational effects were significant (Froude number). For the radial/axial system, excessive splashing outside the vessel prevented 271 rpm tests to be conducted.

7.2.1.1 Effect on $k_L a$

The effect of the impeller system on mass transfer performance is shown in Figure 7.2. Of the impeller systems studied (AD, RR, RA), the 4-bladed $45\,^\circ$ axial-downdraft system was found to be poorest in oxygen mass transfer performance. Converting to a dual-radial disk system resulted in marked increases $k_L a$, as expected. However, the radial/axial combination was found to be most superior - a near doubling of the $k_L a$ was achieved using this system over the existing system.

Figure 7.2 also shows that the top impeller in a dual impeller system was most significant to the oxygen mass transfer performance. This was expected as surface aeration results from vortex generation, shearing action and other surface turbulence phenomena - conditions strongly sensitive to the impeller type and liquid coverage (H_l) as described in Chapter 5, equation 5.14. Also evident is that a negligible oxygen mass transfer rate was achieved using the AD system at the lowest speed, 121 rpm. This suggests that the critical speed for vortexed aeration induction was not attained. Aeration was observed to occur for both the RR and the RA at this low speed, further showing that the radial disk impeller is more effective for surface aeration.

The increase in $k_L a$ of the RA system over the RR system may be attributed to improved gas dispersion and increased gas bubble residence times resulting in increased gas holdup values. This could be the result of the stronger fluid downflow generated by the lower axial down-draft impeller.

7.2.1.2 Effect on Power Draw and ME ratio

The effect of impeller system on power draw is depicted in Figure 7.3. The power draw was found to be stable over the duration of the tests for all impeller configurations and did not undergo any step changes with increasing rpm. All show increasing power draw with increasing rpm. The comparative power draw behaviour of the AD and RR systems were as expected from the literature review. The RA system showed that the lower impeller consumed most of the power in the dual impeller system. This was attributed to the following reasons:

1) increased gas volume distributed in upper portion of tank, which decreased bulk fluid density in this zone.

2) extensive large gas cavity formation decreased upper impeller drag

3) central vortex formation decreased fluid coverage on upper impeller resulting in a further decrease in drag coefficient.

The effect of impeller system on the ME ratio is shown in Figure 7.4. This plot shows that the radial/axial combination system yielded the highest conversion of power to oxygen mass-transfer phenomena. This could be expected from the results shown in Figures 7.2 and 7.3.

All systems showed the same trend of approaching a maxima at 171 rpm. The steep increase in ME for the AD system between 121 and 171 rpm was likely due to the surpassing of the critical speed requirement for surface aeration at 171 rpm. The decreasing trend beyond 171 rpm indicates that the rate of increase in power draw with N was faster than the rate of $k_L a$ increase. This suggests that an increased fraction of the power was being imparted to such fluid mixing processes. The poor ME ratio for the RR system was due to the high power draw of this impeller system. However, in mass-transfer rate limiting processes, maximization of this relationship is not as significant as maximizing $k_L a$. Therefore, rejection of the RR system, which had the lowest ME ratio above 171 rpm is not correct for a mass-transfer application.
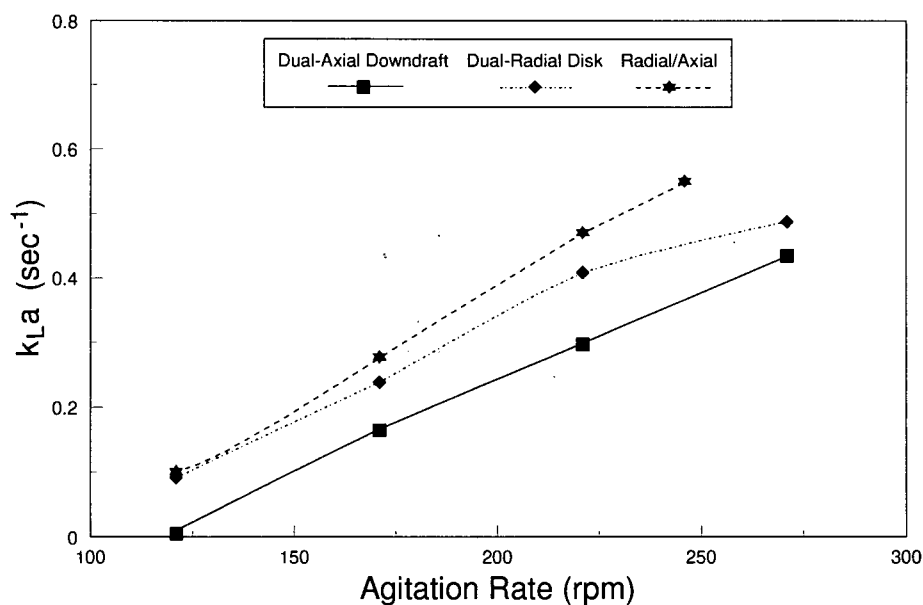
Figure 7.2 The effect of impeller system and agitation speed on $k_L a$ in the model configuration (cooling coils).
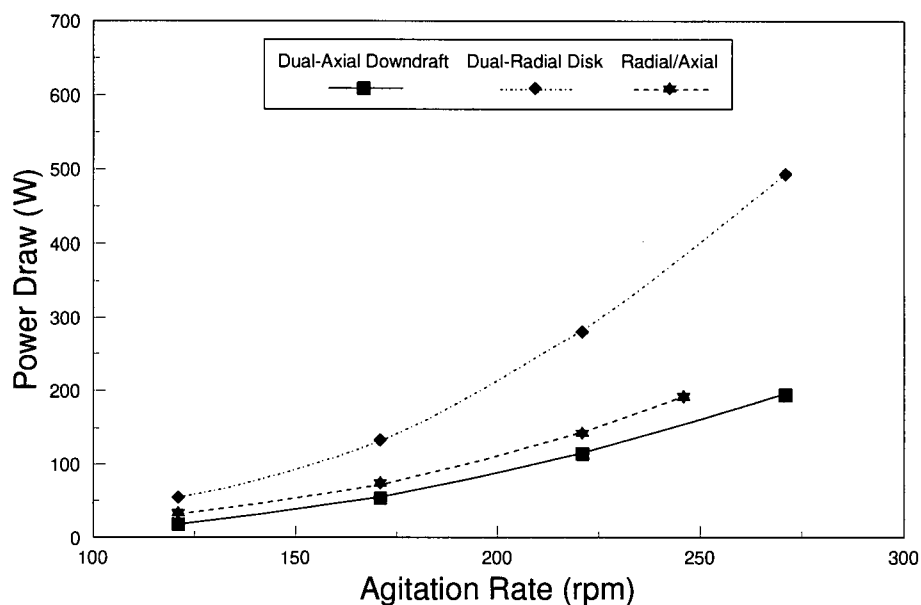
Figure 7.3   The effect of impeller system and agitation speed on power draw in the model configuration (cooling coils).
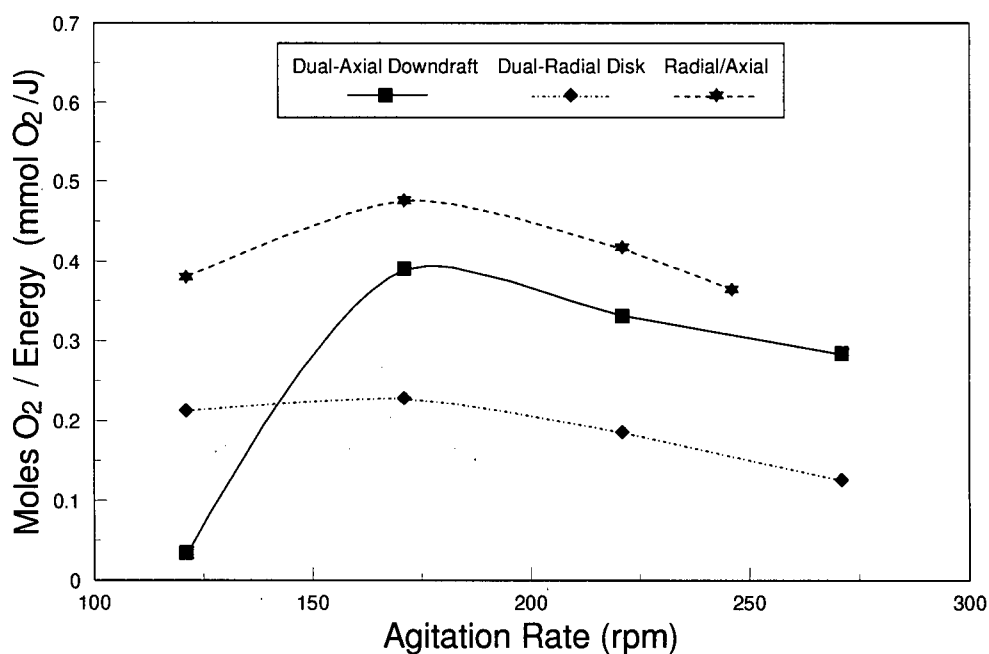
Figure 7.4   The effect of impeller system and agitation speed on mol O_2-energy (ME) ratio in the model configuration (cooling coils).

7.2.1.3 Reproducibility of Measurements

Table 7.2 illustrates the reproducibility of the measurements made in this series of test. In each case, the agitation rate used was 221 rpm. The average values tabulated below were used to create Figures 7.2 and 7.3 above. Excellent reproducibility for power draw was obtained using the OMEGA in-line torque sensor described in Chapter 6. Wider scatter in the data for $k_L a$ measurements were obtained owing to the inherent errors in the chemical analytical method employed. However, the tests were still reproducible within reasonable margins.

Table 7.2 - Reproducibility of the experimental method

Impellers	Run (221 rpm)	$k_L a$ (s^{-1})	P (W)
AD	1	0.275	114.6
	2	0.295	113.8
	3	0.315	113.1
	4	0.303	114.5
	Avg.	0.297 ± 7.5%	114.0 ± 0.8%
RR	1	0.394	277.4
	2	0.404	277.7
	3	0.427	284.1
	Avg.	0.408 ± 4.6%	279.7 ± 0.8%
RA	1	0.452	139.9
	2	0.462	144.6
	3	0.494	143.5
	Avg.	0.470 ± 5.1%	142.7 ± 2.0%

7.2.2 The Effect of Liquid Coverage

A significant process difficulty in the Second Stage leach process is the attainment of a constant batch fill level. Since impeller positions in the autoclave remain fixed, inconsistent fill levels from batch to batch result in variations in the liquid coverage (H_l). As discussed in Chapter 5, liquid coverage plays a crucial role in surface aeration phenomena, as increasing H_I leads to higher critical agitation speed requirements. If the fill height is too high, the existing operating speed of 68 rpm may not be adequate to effect sufficient oxygen incorporation rates. Conversely, too low a coverage can also result in inadequate mass transfer rates if the vortex generated by the dual impeller

system extends below the upper impeller, causing it to run freely in air. Consequently, it was decided to investigate the effect of fill height on mixer performance in the scaled model to see the sensitivity of each type of configuration to deviations from the normal filling height. The normal liquid coverage, scaled from the INCO autoclave was 4.4 cm above the top edge of the upper axial impeller blade (50.5 cm above base). This is shown in Chapter 6, Figure 6.2. Variations in liquid coverages by ±5% and ±10% (±2.5, 5.0 cm respectively) were employed. A standard agitation rate of 221 rpm employed in all tests. Additional sulfite and cobalt were added accordingly to compensate for the volume increase to maintain the 0.25 M concentration.

Results of the tests showing the approximate tolerance to fill height changes are plotted in Figures 7.5. The tests show that all impeller systems exhibited $k_L a$ dependence on fill height. However, the dual-axial system currently employed by INCO was found to be most sensitive to overfilling. A significant reduction in oxygen mass transfer rate resulted after +5% increase in fill height, whereas both radial disk systems exhibited similar decreases only after +10% increases. At +5% filling, changing the impeller system from AD to either the RR or RA systems improved $k_L a$ by over 600% (0.4 s^{-1} vs. 0.06 s^{-1}) in the model. The RR and RA systems were both insensitive to fill height changes between -5 to +5%. A significant reduction in mass transfer performance owing to under filling was only evident after 10% reduction in fill height for all three systems. For all impeller systems, the scaled normal operating level (giving $H_I = 4.4$ cm) appeared to be optimal.

As shown in Figure 7.6, power consumption increased with increased fill height. This was expected as with increasing height, less gas holdup, cavitation and vortexing effects which act to reduce drag apply to the upper impeller.
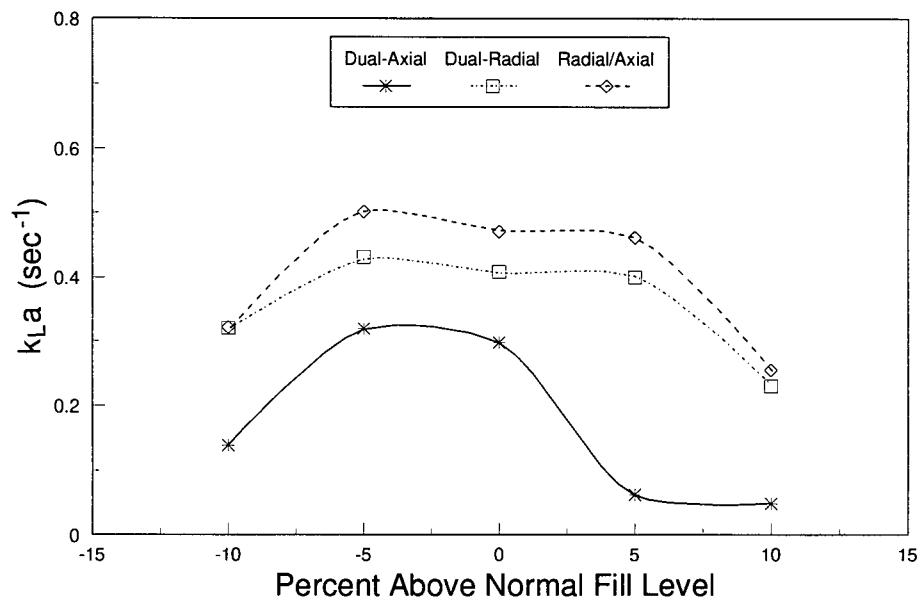
Figure 7.5   The effect of fill level on $k_L a$ for various impeller systems in the model configuration (cooling coils).
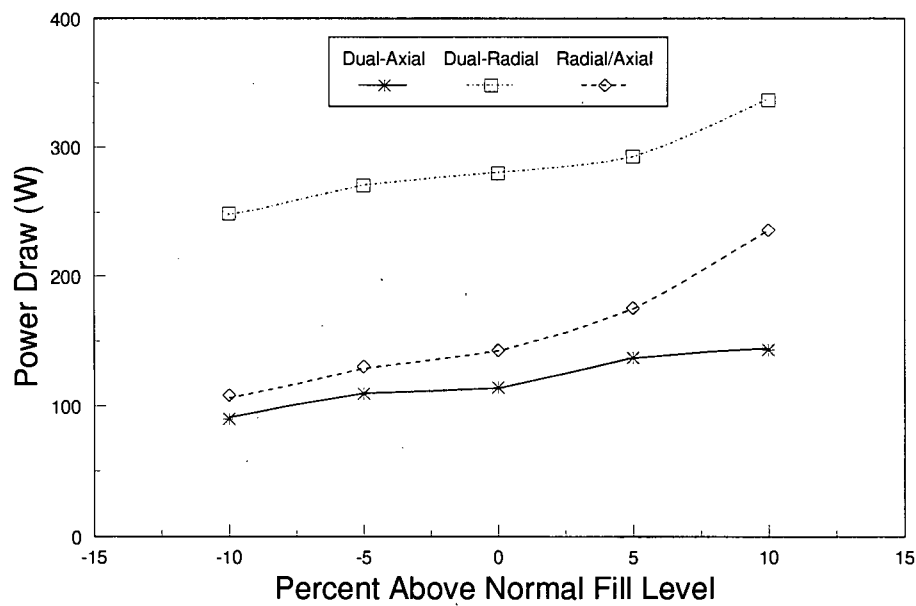
Figure 7.6   The effect of fill level on power draw for various impeller systems in the model configuration (cooling coils).
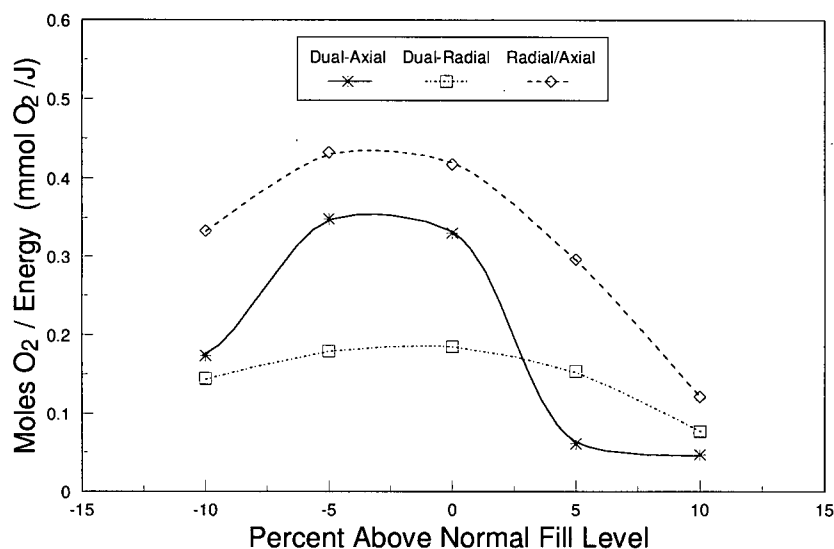
Figure 7.7   Effect of fill level on mol O_2-energy ratio (ME) for various impeller systems in the model configuration (cooling coils).

7.2.3   Other Observations

A 200 L sample of BCS slurry was obtained for use in power draw measurements as well as visual mixing observations. The viscosity of this sample was relatively low (10 cP @ 4.9 s^{-1}) indicating that it was not from an extended leach batch.   Comparison of the power draw characteristics of the slurry with that of the 0.25 M Na_2SO_3 solution are shown in Figure 7.8   for the AD impeller system.
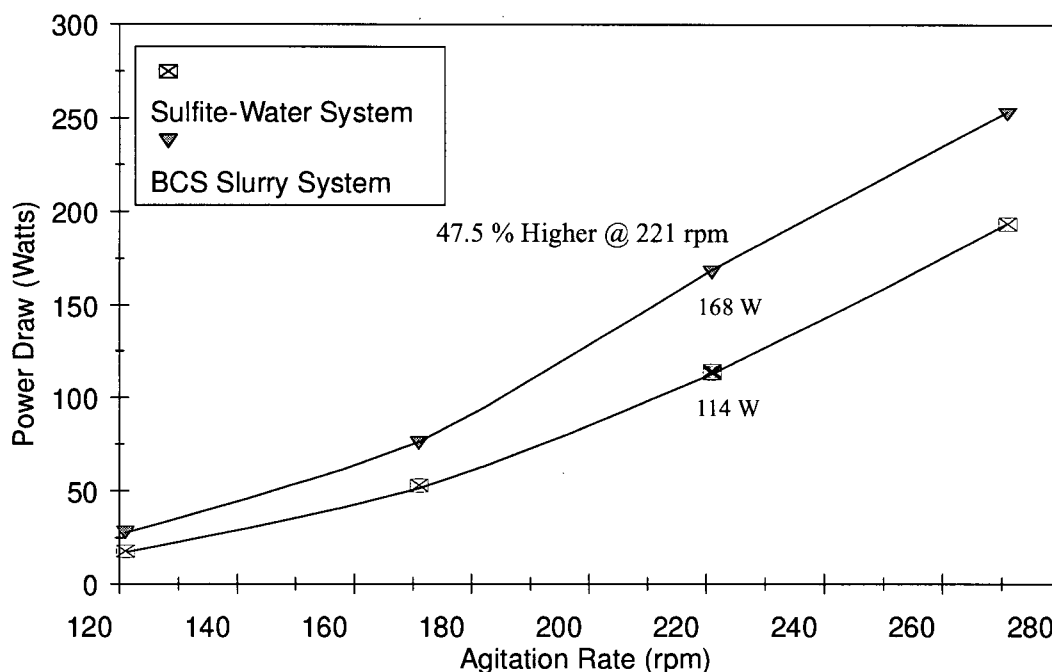
Figure 7.8   Impeller power draw comparison between a BCS slurry and a sulfite-water system

Because of the opacity of the dark green slurry, no conclusions could be drawn about the mixing patterns. However, significant frothing of the contents was observed, forming a foam layer about 4 inches thick that remained stable after mixing was ceased. This was believed to be due to the presence of Dowfax 1AO surfactant which is employed as an anti-acid misting reagent in the copper electrowinning tankhouse. The surfactant is believed to be present in the spent electrolyte and is introduced into the Second Stage leach circuit during batch feed makeup. The apparent evidence of the surfactant observed during the mixing study is significant because it indicates that the compound remained stable throughout the Second Stage leach operation. As discussed earlier (Section 5.4.1) surfactants can have a disastrous effect on gas-liquid mass transfer rates [63]. Moreover, if a stable foam layer forms at the liquid surface, surface aeration will likely be inhibited regardless of the impeller system employed. Therefore, further studies on the effect of Dowfax on gas-liquid mass transfer should be performed.

7.3   The Effect of Baffling

The use of cooling coils to achieve a baffling effect has been discussed in Chapter 5. Swiniarski [75] and Dawson-Amoah [76] demonstrated that the presence of baffles greatly increased surface aeration rates provided that a stable vortex could be formed. It was therefore decided to compare k_La and power draw characteristics of the cooling coils in the model to that of an unbaffled tank and a conventional (vertical) 4-baffled tank (B/T = 1/10). This was done to assess the relative degree of baffling provided by the cooling coils.

The results for each impeller system under the three states of baffling are shown in Figures 7.9 - 7.14 (located at the end of this section) and discussed below.

7.3.1   Dual-Axial Down-draft Impeller System (AD)

Above 121 rpm, the cooling coils appeared to give slightly higher oxygen mass transfer rates than the 4-baffled condition (Figure 7.9) - the difference increasing with increasing rpm. The significant k_La obtained in the 4-baffled tank indicated that only a partially-baffled condition was achieved. The noted presence of a stable vortex at speeds in excess of 121 rpm confirmed this condition. The generation of a stable vortex resulting in high k_La was attributed to the low liquid coverages (H/T = 4.4/60) for the normal fill level conditions. The minimal mass transfer rates in the unbaffled condition was expected owing to gross circulation and very low turbulent shear phenomena.   The slight increase in k_La at 271 rpm may be attributable to increased significance of the lower blade.

The degree of baffling in a system is also reflected by the relative power draw for the system. Comparison of the power draw for each system (Figure 7.10) shows that the degree of baffling offered by the cooling coils was slightly less than the conventional 4-baffled system. This was probably attributable to the open structure of the cooling coils and the curved surface of the cylindrical rods which produced less drag.

In the unbaffled tank, it was observed that the central vortex did not fully extend beyond the lower impeller even at the highest rpm (271). This explains the continuous increase in power draw with rpm over the range of speeds studied. If vortexing extended beyond the lower impeller, as for

higher rpm or higher impeller-tank bottom clearances, a local maxima in power draw should occur at a distinct rpm.

7.3.2   Dual Radial Disk Impeller System (RR)

The effect of baffling on the mixer performance of the RR system followed the same general characteristics as the AD system with the exception that the $k_L a$ for both the cooling coils and the standard 4-baffle configuration were nearly identical at all speeds (Figure 7.11).

The larger power draws for both types of baffling (Figure 7.12) as compared to the AD system can be explained by the flow pattern generated by each type of impeller. The predominantly radially directed flow of the radial disk impeller perpendicularly intersects vertical baffles/cooling coils. Fluid motion is then redirected which results in increased turbulent intensities in all parts of the tank. High impeller drag results. This is not the case for pitch blade turbines in which the dominant fluid motion is directed parallel to the baffles.

During the course of the 221 and 271 rpm tests in the 4-baffled tank, fluctuations in impeller power draw were observed. Specifically, periodic power spikes were noted. For the 271 rpm test, a spike occurring towards the end of the run caused the motor to trip. It is believed that this behaviour was attributed to the collapse and reformation of the central vortex. The cause of this phenomena is discussed below.

7.3.3   Radial / Axial Impeller System (RA)

Figure 7.13 shows that the RA system underwent a decrease in mass transfer rate performance between 171-221 rpm for the 4-baffled tank. For speeds above 171 rpm, it was observed that a central vortex was present for only the first 1-2 minutes of agitation, thereafter collapsing. A step increase in power draw accompanied this transition. Beyond this transition, the system appeared to be in a near fully baffled state and power draw stabilized at this higher value. Power and mass transfer measurements were made after power stabilization. As shown in Figure 7.14, impeller power draw increased dramatically with speed above 171 rpm. Similar observations of central vortex instabilities were made by Swiniarski [75] in some of his tests. Vortex instability probably resulted from increased redirection of radial flow back into the upper impeller

zone. This disrupted the rotational flow pattern of the central vortex causing collapse to occur. A near fully baffled state resulted.

For the cooling coil tank system, stable central vortices and power draws were observed at all speeds tested. This was probably attributable to the open structure of the cooling coil system which effects less flow redirection, thereby retaining more rotary circulation over standard baffles.
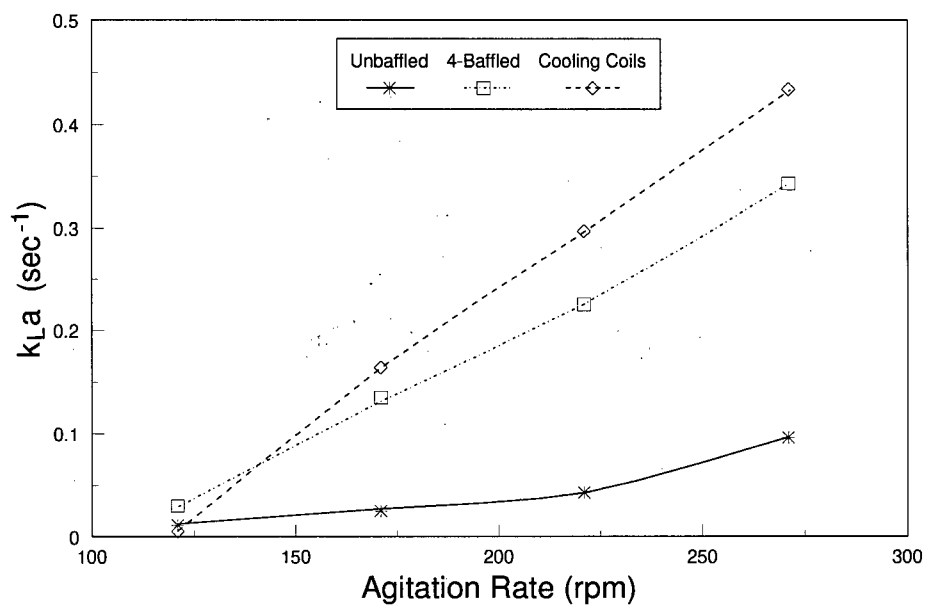
Figure 7.9 The effect of baffling on $k_L a$ for the dual axial down-draft (AD) impeller system.
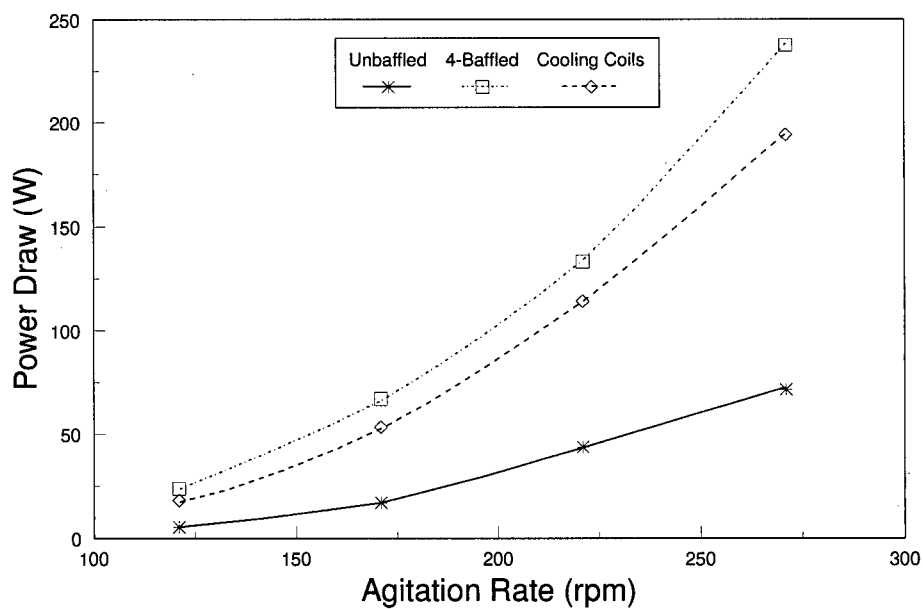
Figure 7.10 The effect of baffling on power draw for the dual axial down-draft (AD) impeller system.
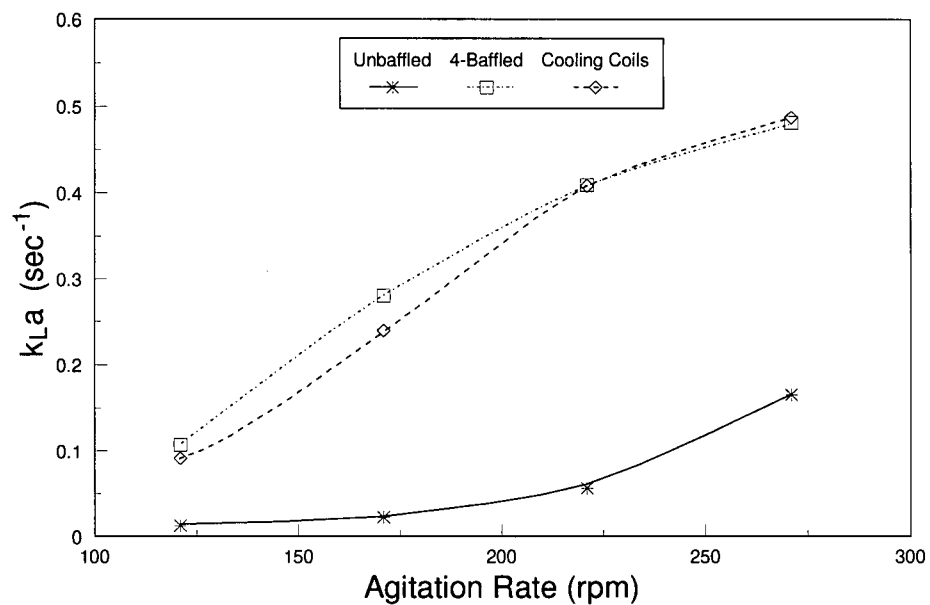
Figure 7.11 The effect of baffling on k_La for the dual radial disk (RR) impeller system.
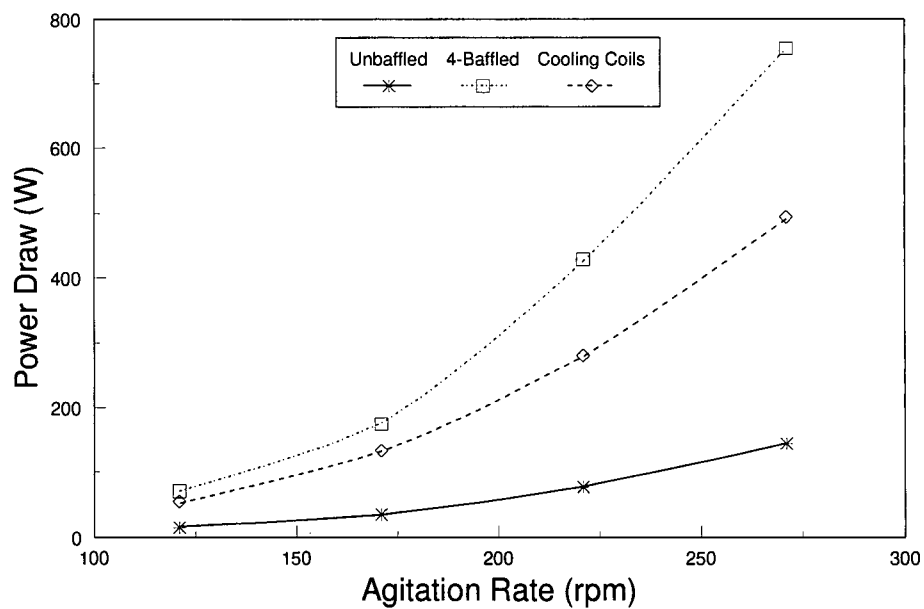
Figure 7.12 The effect of baffling on power draw for the dual radial disk (RR) impeller system.

- 127 -
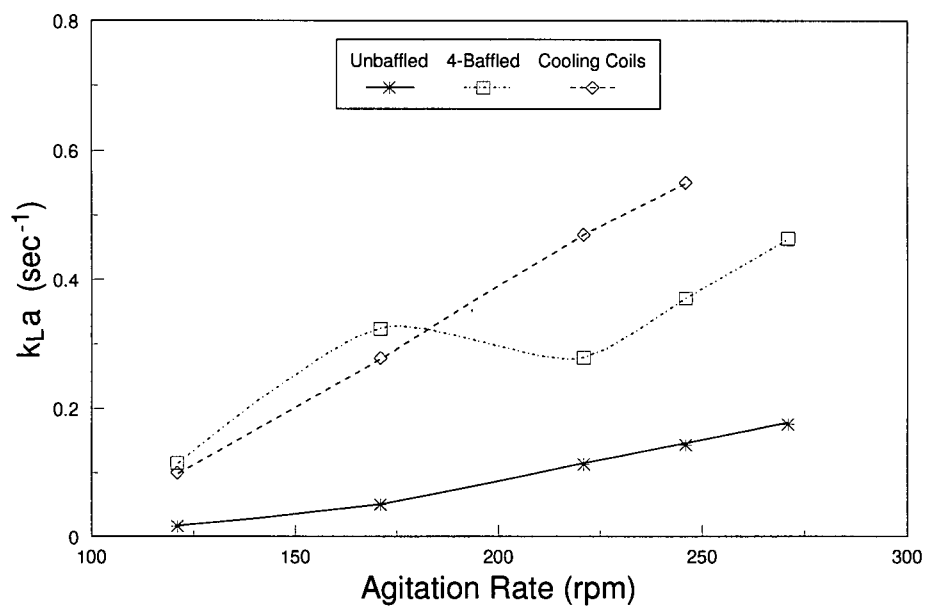
Figure 7.13   The effect of baffling on k_La for the radial/axial (RA) impeller system.
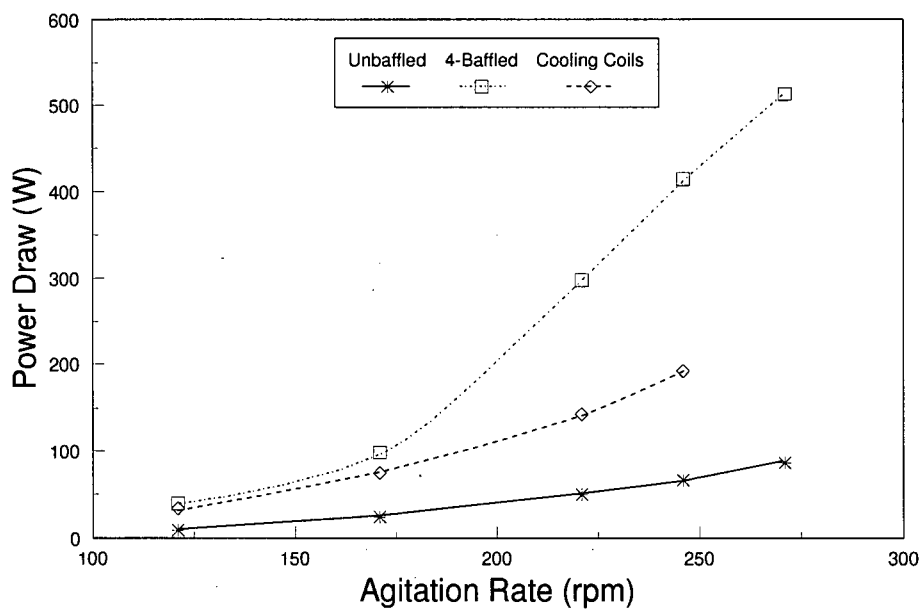
Figure 7.14   The effect of baffling on power draw for the radial/axial (RA) impeller system.

7.4 Summary and Conclusions

Oxygen mass transfer and power draw measurements were made in a scaled model of the INCO Second Stage autoclave. The test work showed that the current dual axial down-draft impeller system was poorest in gas-liquid mass transfer performance and fill level sensitivity among the impellers studied. Significant improvements were achieved when converting to a dual radial disk system; however, the improvements were made at the expense of much higher power draw. A radial/axial system appeared to combine the benefits of both radial disk and axial down-draft impeller systems. High oxygen mass transfer rates were achieved at relatively low power consumption resulting in highest mol O_2-energy ratio (ME) performance. Both the dual radial disk impeller system and the radial/axial system exhibited less sensitivity to fill level than the axial down-draft system.

The presence of the vertical cooling coils in the autoclave yielded a baffling affect which greatly increased oxygen mass transfer rates over an unbaffled tank system. Based on power draw measurements, the degree of baffling provided was less than that of the standard vertical 4-baffle configuration owing to its open structure and curved surface. This enabled the sustaining of a stable central vortex for all agitation speeds which improved surface aeration rates and prevented power draw fluctuations.

Chapter 8

Final Conclusions and Recommendations for Further Work

This thesis was divided into two parts. In part I, oxidative pressure leaching of various First Stage residues were performed at temperatures between 100-135°C. It was found that the combination of high feed arsenic (1.40 wt.% As) and 135°C leach temperature resulted in an extremely viscous basic copper sulfate slurry product which inhibited oxygen mass transfer into solution and reduced the covellite leaching rate. The presence of arsenic in the electrolyte produced similar results to that of arsenic in feed solids. The modification the basic copper sulfate precipitate morphology from large platelets to small acicular shapes was responsible for the high viscosity slurries. It is believed that such a modification resulted from increased supersaturation levels and the formation of increased numbers of a nucleation catalysing substrates. Indirect evidence suggested that basic copper arsenate was the species responsible for BCS habit modification. However, positive identification of this species was not made to fully support this claim. Therefore, additional work must be done to identify the species responsible or provide additional evidence for basic copper arsenate formation. The following is a list of suggested experiments and subsequent analyses that could supplement the current study:

- An investigation of the addition of seed crystals of basic copper arsenate into a solution containing copper and sulfate, followed by pH increase. The amount of seed crystals added as well as the average seed size should be varied to see if heterogenous nucleation of BCS would take place, and if so, what types of BCS morphology would result. This would have to be done at high temperatures (> 89°C) because of the decreased stability of both species at lower temperatures.

- Leaching of high arsenic feeds with electrolyte containing as high a dissolved arsenic concentration as possible (> 10 g/L As). This should be followed by selective pH leach experiments and XRD analysis. The higher feed arsenic content should increase the amount of As-containing precipitant formed. However, leaching at 135°C may produce larger numbers of smaller sized of the arsenic-containing species. Therefore, XRD detection may still be difficult, especially with the large amount of unreacted covellite that should still remain. Leaching at 115°C may yield larger

crystals of the As-species and lower amounts of unreacted covellite should be present. Therefore, selective pH dissolution followed by XRD analyses of the residue may be more revealing for the 115°C leach product.

• Application of alternative techniques for species identification other than XRD or SEM methods.

• Investigation of the effect of iron concentration. Grewal *et al.* [7] found that a low feed iron concentration produced a high viscosity BCS slurry. The role of iron must be further studied to assess whether or not ferric ions complex with arsenate ions prior to the precipitation of the problematic arsenic-containing species. If the precipitation of a ferric-arsenate compound precedes the precipitation of the problematic phase, then increasing ferric concentrations may negate the deleterious effect of high feed arsenic concentrations. A series of test should be done with increasing electrolyte iron concentrations concurrent with increasing electrolyte arsenic concentrations. These results should then be compared to the spiked As-electrolyte test results obtained in the current study.

In part II of the investigation, an assessment of the gas-liquid mass transfer performance of the Second Stage autoclave was made using a scaled model of the vessel. It was found that significant increases in the mass transfer rate were obtained by converting the upper impeller from the current 4-bladed (45° pitch) axial downdraft impeller to that of a 6-bladed radial disk impeller. Additional scale-up work should be done to ensure that these preliminary results are translatable to the full-scale system. Since a dual-axial impeller system was employed in the laboratory-scale leaches of part I, conversion to a radial disk system in the Parr autoclave system may reveal whether such a conversion would produce higher copper extraction rates for high temperature- high arsenic feed leaches. Additional tests on the scaled model should include:

• 3-phase studies to assess gas-liquid mass transfer performance concurrent with solid suspension performance.

• Heat transfer studies in the Second Stage leach autoclave to determine if adequate heat

distribution and temperature control is being achieved in all parts of the vessel. A dual-radial disk impeller system may improve heat distribution because of the increased fluid flow-cooling coil interaction produced by a radial disk-vertical cooling coil system (Section 5.1.2)

• Finally, the effect of recycled Dowfax surfactant in the spent electrolyte should be investigated for its effect on gas-liquid mass transfer rates

References

1. Berezowsky, R.M.G.S, Collins, M.J., Kerfoot, D.G.E. and Torres, N. "The commercial status of pressure leaching technology", *The Journal of Metals*, **43**, No. 2 (1991), pp. 9-15.

2. Natunen, H., Arias, H., Guasch, D., Mallory, J and Saarenpää, T. "Copper heap leaching-solvent extraction-electrowinning process at the Zaldivar mine., In Print, Copper 95-Cobre 95. (1995).

3. Peters, E. "Oxygen utilization in hydrometallurgy: Fundamental and practical issues". In: G. Kachaniwsky and C. Newman (Eds.), *Proceedings of the International Symposium on the Impact of Oxygen on the Productivity of Non-Ferrous Metallurgical Processes*. Pergamon Press, New York, NY, USA (1987), pp. 151-164.

4. Parker, E.G. "Oxidative pressure leaching of zinc concentrates", *CIM Bulletin*, **74**, No. 829 (1981), pp. 145-150.

5. Kuhn, M.C., Arbiter, N., Kling, H. "Anaconda's Arbiter process for copper", *CIM Bulletin*, **67**, No. 742 (1974), pp. 62-73.

6. Tyroler, P.M., Sanmiya, T.S. and Hodkin, E.W. "Hydrometallurgical processing of Inco's Pressure Carbonyl residue". In: G.P. Tyroler and C.A. Landolt (Eds.), *The Extractive Metallurgy of Nickel and Cobalt*. TMS, Warrendale, PA, USA (1988), pp. 391-401.

7. Grewal, I. Dreisinger, D.B., Krueger, D., Tyroler, P.M., Krause, E. and Nissen, N.C. "Total oxidative leaching of Cu_2S-containing residue at INCO Ltd.'s copper refinery: laboratory studies on the reaction pathways", In: W.C. Cooper and D.B. Dreisinger (Eds.), *Hydrometallurgy, Theory and Practice-Part A*. Elsevier, Amsterdam, Netherlands (1992), pp. 335-356.

8. Grewal, I. *Oxidative Pressure Leaching of Chalcocite in Sulphuric Acid*, MASc. Thesis, The University of British Columbia (1991).

9. Dreisinger, D.B. and Peters, E. "The mathematical modelling of the Inco CRED Second Stage leach". Report prepared for Inco (1989).

10. Clément, C., Tyroler, P.M., Krause, E. and Nissen, N.C. "Total oxidative leaching of Cu_2S-containing residue at Inco Ltd.'s copper refinery: the effect of morphology and viscosity of basic copper sulfate on the leaching of cupric sulphide". In: W.C. Cooer and D.B. Dreisinger (Eds.), *Hydrometallurgy, Theory and Practice-Part A*. Elsevier, Amsterdam, Netherlands (1992), pp. 335-356.

11. Pourbaix, M.J.N., *Atlas of Electrochemical Equilibria in Aqueous Solutions at 25 °C*, Pergamon Press, Oxford, England (1966).

12. Pollard, A.M., Thomas, R.G., and Williams, P.A. "The stabilities of antlerite and $Cu_3SO_4(OH)_4 \cdot 2H_2O$: their formation and relationships to other copper(II) sulfate minerals". *Mineralogical Magazine*, **56** (1992), pp. 359-365.

13. Burstorff, A., and van Muylder, J. "Comportement électrochimique du cuivre en solutions sulfuriques. Diagrammes d'équilibres tension-pH du système Cu-$SO_4H_2OH_2$ à 25°C". *Electrochemica Acta*, **9** (1964), pp. 607-612.

14. Kametani, H., and Aoki, A. "Potential-pH diagram of the Cu-SO_4-H_2O and Cu-Cl-H_2O suspension systems at 90°C". *Trans. Nat. Res. Inst. Japan*, **15**, No. 4 (1973), pp. 183-194.

15. Kwok, O.J., and Robins, R.G. "Thermal precipitation in aqueous solutions". In: D.J.I. Evans and R.S. Shoemaker (Eds.), *International Symposium on Hydrometallurgy*. AIME, New York, NY, USA (1973), pp 1033-1080.

16. Criss, C.M., and Cobble J.W. "The thermodynamic properties of high temperature aqueous solutions", IV and V. *J. Am. Chem. Soc.*, **86** (1964), pp. 5385-5393.

17. F. Letowski. "The solid products of hydrolysis of $CuSO_4$ solutions at temperatures from 100 to 200°C" (Polish Translation by T. Trocyznski). *Pr. Nauk. Inst. Chem. Nieorg. Pwr.*, **10** (1972), pp. 31-41.

18. King, E.G., Mah, A.D., and Pankratz, L.B. *Thermodynamic Properties of Copper and its Inorganic Compounds*, INCRA, New York, NY, USA (1973).

19. Klein, C., and Hurlbut, Jr., C.S. *Manual of Mineralogy, 20th Ed.*, John Wiley & Sons, New York, NY, USA (1985).

20. *Powder Diffraction File PDF-2 Database Sets 1-41*, International Centre for Diffraction Data, Swarthmore, PA, USA (1991).

21. Corey, R.B. "Adsorption vs. precipitation". In: M.A. Anderson and A.J. Rubin (Eds.), *Adsorption of Inorganics at Solid-Liquid Interfaces*, Ann Arbor Science, Michigan, USA (1981), pp. 161-182.

22. Stumm, W. and Morgan, J.J. *Aquatic Chemistry*, John Wiley & Sons, New York, NY, USA (1981).

23. Khamskii, E.V. *Crystallization from Solutions*, Consultants Bureau, New York, NY, USA (1969).

24. Randolph, A.D. and Larson, M.A. *Theory of Particulate Processes: Analysis and Techniques of Continuous Crystallization*, Academic Press, Orlando, FL, USA (1988).

25. Burkhart, L. and Voigt, J. "Aqueous precipitation in hydrometallurgy". In: R.G. Bautista, R.J. Wesely and G.W. Warren (Eds.), *Hydrometallurgical Reactor Design and Kinetics*, TMS, Warrendale, PA, USA (1986), pp. 441-457.

26. Furedi-Milhofer, H. and Walton, A.G. "Principles of precipitation of fine particles". In: G.D. Parfitt (Ed.), *Dispersion of Powders in Liquids*, Applied Science Publishers, London, England (1981), pp. 203-271.

27. Newkirk, J.B. and Turnbull, D. "Nucleation of ammonium iodide crystals from aqueous solutions". *J. Appl. Phys.* **26**, (1955) pp. 579-583.

28. Mullin, J.W. *Crystallization*, Butterworth-Heinemann Ltd, Oxford (1993).

29. Dutrizac, J.E, Jambor, J.L. and Chen, T.T. "The behaviour of arsenic during jarosite precipitation: Reactions at 150 °C and the mechanism of arsenic precipitation". *Canadian Metallurgical Quarterly.* **26**, No. 2, (1987) pp. 103-115.

30. Ugarte, F.J.G., and Monhemius, A.J. "Characterisation of high-temperature arsenic-containing residues from hydrometallurgical processes". In: W.C. Cooper and D.B. Dreisinger (Eds.), *Hydrometallurgy, Theory and Practice-Part B*. Elsevier, Amsterdam (1992), pp. 69-86.

31. Griffin, R.A. and Jurinak, J.J. "The interaction of phosphate with calcite". *Soil Sci. Soc. Amer. Proc.*, **37** (1973) pp. 847-850.

32. Söhnel, O. and Garside, J. *Precipitation*, Butterworth-Heinemann Ltd, Oxford, England (1992).

33. Philpotts, A.R. *Principles of Igneous and Metamorphic Petrology*. Prentice Hall, New Jersey, NY, USA (1990).

34. Ring, T.A. "Kinetic effects on particle morphology and size distribution during batch precipitation". *Powder Technol*, 65, (1991) pp. 195-206.

35. Walton, A.G. *The Formation and Properties of Precipitates*, Wiley-Interscience, New York, NY, USA (1967).

36. Larson, M.A. "Secondary nucleation: an analysis" . In: S.J. Jançic and E.J. de Jong (Eds.), *Industrial Crystallization 81*, North-Holland Publishing Company, Amsterdam, Netherlands (1982), p. 55.

37. Demopoulos, G.P. "Impurity removal and disposal by aqueous precipitation - The crystallization approach - Short Course Notes". In: B. Harris and E. Krause (Eds.), *The 24th Annual CIM Hydrometallurgical Meeting: Impurity Control and Disposal in Hydrometallurgical Processes, August 19-20, 1994*.

38. Sears, G.W. "Recent developments in nucleation theory", In: C. Klingsberg (Ed.), *Physics and chemistry of ceramics*, Gordon and Breach, New York, NY, USA (1963), pp. 311-324.

39. Nissen, N.C. "CRED: Selective pH dissolution of BCS from 2nd Stage leach test# S20T135". *INCO Ltd. Internal Report - Project # 95-2846* (1993).

40. Gonzales, V.L.E., and Monhemius, A.J. "The mineralogy of arsenates relating to arsenic impurity control". In: J.L Hendrix and P.B. Queneau (Eds.), *Arsenic Metallurgy-Fundamentals and Applications*. TMS-AIME, Warrendale, PA, USA (1987), pp. 405-453.

41. Robins, R.G. "The aqueous chemistry of arsenic in relation to hydrometallurgical processes". In: A.J. Oliver (Ed.), *The Proceedings of the 15th Annual Hydrometallurgical Meeting, Impurity Control and Disposal*. paper 1, CIM, Montreal, PQ, Canada (1985).

42. Krause,E., and Ettel, V.A. "Ferric arsenate compounds: are they environmentally safe? Solubilities of basic ferric arsenates". In: A.J. Oliver (Ed.), *The Proceedings of the 15th Annual Hydrometallurgical Meeting, Impurity Control and Disposal*. paper 5, CIM, Montreal, PQ, Canada (1985).

43. Robins, R.G., Huang, J.C.Y., Nishimura, T., and Khoe, G.H. "The adsorption of arsenate ion by ferric hydroxide". In: J.L Hendrix and P.B. Queneau (Editors), *Arsenic Metallurgy-Fundamentals and Applications*. TMS-AIME, Warrendale, PA, USA (1987), pp. 99-112.

44. Nishimura, T., and Tozawa, K. "Removal of arsenic from waste water by addition of calcium hydroxide and stabilization of arsenic-bearing precipitates by calcination". In: A.J. Oliver (Ed.), *The Proceedings of the 15th Annual Hydrometallurgical Meeting, Impurity Control and Disposal*. paper 3, CIM, Montreal, PQ, Canada (1985).

45. Mirza, A.H., Tahija, D., Chen, K. and Haung, H.H. "Formation and stability studies of iron-arsenic and copper-arsenic compounds from copper electrorefining sludge". In: J.L. Hendrix and P.B. Queneau (Editors), *Arsenic Metallurgy-Fundamentals and Applications*. TMS-AIME, Warrendale, PA, USA (1987), pp. 37-58.

46. Harris, G.B. and Monette, S. "The stability of arsenic-bearing residues". In: J.L Hendrix and P.B. Queneau (Eds.), *Arsenic Metallurgy-Fundamentals and Applications*. TMS-AIME, Warrendale, PA, USA (1987), pp. 469-488.

47. Stewart, C.L., Budac, J., Wrana, D., Krause, E. and Laundry, S.W. "Development of a copper arsenate process for Inco's Manitoba Division". In: B. Harris and E.Krause (Eds.), *Impurity Control and Disposal in Hydrometallurgical Processes: 24th Annual Hydrometallurgical Meeting*. TMS-CIM, Warrendale, PA, USA (1994), pp 17-30.

48. Droppert, D. Private communication, McGill University, Montreal, PQ, Canada (March 17, 1995).

49. Warren, J.H. "A study of the acid pressure leaching of $CuFeS_2$, Cu_2S and CuS", *Australian Journal of Applied Science*, **9** (1958), pp. 36-51.

50. Stanczyk, M.H., and Rampacek, C. "Oxidation leaching of copper sulfides in acidic pulps at elevated temperatures and pressures", *U.S. Bureau of Mines - Report 6193* (1963).

51. Mao, M.H., and Peters, E. "Acid pressure leaching of chalcocite", In: K. Osseo-Asare and J.D. Miller (Eds.), *Hydrometallurgy Research, Development and Plant Practice*, TMS-AIME, Warrendale, PA, USA (1983), pp. 243-270.

52. Habashi, F. "Precipitation in hydrometallurgy", *18th International Mineral Processing Congress, Sydney, Australia, 1993*. The Australasian Institute of Mining and Metallurgy, Parkville, NSW, Australia (1993), pp. 1323-1328.

53. Oldshue, J.Y. *Fluid Mixing Technology*, Chemical Engineering-McGraw-Hill, Inc., New York, NY (1983).

54. Garrison, C.M. "How to design and scale mixing pilot-plants". *Chemical Engineering*, **90**, No. 2 (1983), pp. 63-70.

55. Shah, Y. "Design parameters for mechanically agitated reactors". In: J. Wei (Ed.), *Advances in Chemical Engineering, Vol. 17*. Academic Press, Inc., New York, NY (1992).

56. Kubera, P.M., and Oldshue, J.Y. "Advanced impeller technologies match mixing performance to process needs", Randol Gold Conference, Vancouver, BC, Canada (1992), pp. 279-285.

57. Litz, L.M. "A novel gas-liquid stirred tank reactor". Chemical Engineering Progress, **81**, No. 11 (1985), pp. 36-39.

58. Tatterson, G.B. *Fluid Mixing and Gas Dispersion in Agitated Tanks*, McGraw-Hill, Inc., New York, NY, USA (1991).

59. Treybal, R.E. *Mass Transfer Operations*, McGraw-Hill, Inc., New York, NY, USA (1987).

60. Hackl, R.P. "Operation of a commercial scale bioleach reactor at the Congress gold property". In: M.C. Fuerstenau and J.L. Hendrix (Eds.), *Advances in Gold and Silver Processing*. Soc. Min. Metall. Explor., Littleton, Colo., USA (1990), pp. 131-142.

61. Edwards, M.F., and Baker, M.R. "Mixing of liquids in stirred tanks". In: N. Harnby, M.F. Edwards, A.W. Nienow (Eds.), *Mixing in the Process Industries*, Butterworth-Heinemann, Ltd., Oxford, England (1992), pp. 137-158.

62. Smith, J.M. "Physical aspects of water aeration". *Prog. Wat. Tech.*, **11**, No. 3, Permagon Press, England (1979), pp. 1-8.

63. McLaughlin, J.D., Quinn, P., Agar, G.E., Cloutiér, J.Y., Dubé, G., and LeClerc, A. "Oxygen mass transfer rate measurements under different hydrodynamic regimes". In: *18th International Mineral Processing Congress, Volume 5, Sydney, Australia, 1993.* The Australasian Institute of Mining and Metallurgy, Parkville, NSW, Australia (1993), pp. 1153-1159.

64. Chapman, C.M., Nienow, A.W., Cooke, M., and Middleton, J.C. "Particle-gas-liquid mixing in stirred vessels - part II: gas-liquid mixing". *Chem. Eng. Res. Des.,* **61**, No. 3 (1983), pp. 82-95.

65. Chain, E.B., Paldino, S., Callow, D.S., Ugolini, F., and van der Sluis, J. "Studies on aeration - I". *Bull. World Hlth Org.,* 6, No. 1-2 (1952), pp.73-97.

66. Middleton, J.C. "Gas-liquid dispersion and mixing". In: N. Harnby, M.F. Edwards, A.W. Nienow (Eds.), *Mixing in the Process Industries,* Butterworth-Heinemann, Ltd., Oxford, England (1992), pp. 322-363.

67. van't Riet, K., and Smith, J.M. "The behaviour of gas-liquid mixtures near Rushton turbine blades". *Chem. Engng Sci.,* **28**, No. 8 (1983), pp. 1031-1037.

68. Warmoeskerken, M.M.C.G., and Smith, J.M. "Flooding of disc turbines in gas-liquid dispersions: a new description of the phenomenon". *Chem. Engng Sci.* **40**, No. 11. (1985), pp. 2063-2071.

69. Nienow, A.W., and Wisdom, D.J. 'Flow over disc turbine blades", *Chem. Engng Sci.,* **29**, No. 9 (1974), pp. 1994-1996.

70. Boerma, H., and Lankester, J.H. "The occurrence of minimum stirring rates in gas-liquid reactors". *Chem. Engng. Sci.,* **23**, No. 7 (1968), pp. 799-801.

71. Clark, M.W. and Vermeulen, T. "Incipient vortex formation in baffled vessels". *AIChE J.,* **10**, No. 3, (1964), pp. 420-422.

72. Greaves, M., and Kobbacy, K.A.H. "Surface aeration in agitated vessels". *Fluid Mixing. IChemE Symp. Series No. 64* (1981), pp. H1-H22.

73. Veljković, V.B., Bicok, K.M., and Simonović, D.M. "Mechanism, onset and intensity of surface aeration in geometrically-similar sparged, agitated vessels", *The Canadian Journal of Chemical Engineering,* **69** (1991), pp. 916-926.

74. Degraaf, K. *An Investigation of Gas-Liquid Mass Transfer in Mechanically Agitated Pressure Leaching Systems,* MASc. Thesis, The University of British Columbia (1984).

75. Swiniarski, R.P. *Rates and Efficiencies of Oxygen Transfer by Gas Pumping Agitators in Gas-Liquid Mixing Systems,* MASc. Thesis, The University of British Columbia (1991).

76. Dawson-Amoah, J. *Gas-Liquid Mass Transfer by Gas Pumping Agitators in Oxygen Pressure Leaching Systems,* MASc. Thesis, The University of British Columbia (1991).

77. Brennan, D.J. "Vortex geometry in unbaffled vessels with impeller agitation". *Trans. Instn Chem. Engrs,* **54,** No. 4 (1976), pp. 209-217.

79. Joshi, J.B., and Sharma, M.M. "Mass transfer and hydrodynamic characteristics of gas inducing type of agitated contactors". *The Canadian Journal of Chemical Engineering,* **55** (1977), pp. 683-689.

80. van't Riet, K. "Review of measuring methods and results in nonviscous gas-liquid mass transfer in stirred vessels". *Ind. Eng. Chem. Process Dev.,* **18,** No. 3 (1979), pp. 357-363.

81. Charpentier, J.C. "Mass-transfer rates in gas-liquid absorbers and reactors". In: T.B. Drew, G.R. Cokelet, J.W. Hoopes, Jr, and T. Vermeulen (Eds.), *Advances in Chemical Engineering Vol. 11,* Academic Press, New York, NY, USA (1981), pp. 1-133.

82. Bassett, J., Denney, R.C., Jeffery, G.H., and Mendham, J. *Vogel's Textbook of Quantitative Inorganic Analysis, Fourth Edition,* Longman Group Ltd., London, England (1978).

83. Linek, V., and Vacek, V. "Chemical engineering use of catalyzed sulfite oxidation kinetics for the determination of mass transfer characteristics of gas-liquid contactors", *Chem. Engng Sci.,* **36,** No. 11 (1981), pp. 1747-1768.

84. Krause, E. *The Oxidation of Ferrous Sulfate Solutions by Sulfur Dioxide and Oxygen,* PhD. Thesis, The University of Waterloo (1986).

85. Dunn, I.J, and Einsel, A. "Oxygen transfer coefficients by the dynamic method". *J. appl. Chem. Biotechnol,* **25** (1975), pp. 707-720.

86. Grewal, I. *Unpublished report prepared for Praxair* (1993).

87. Latimer, W.M. *The Oxidation States of the Elements and their Potentials in Aqueous Solutions,* Prentice-Hall, Inc., Englewood Cliffs, NJ, USA (1938), pp. 359-369.

88. Rao, Y.K. *Stoichiometry and Thermodynamics of Metallurgical Processes,* Cambridge University Press, Cambridge, England (1985).

Appendices

Table I-A1: Standard Gibbs Free Energy of Formation, Entropy and Heat Capacity Data

Species	$\Delta G°_f$ (cal/mole)	$S°$ (cal/mole K)	$C_p°$ (cal/mole K)
H^+	0	0	28
H_2O	-56 687	16.71	18.1
HSO_4^-	-180 690	31.5	-35
SO_4^{2-}	-177 970	4.8	-115
$H_2S_{(a)}$	-6660	29	----
HS^-	2880	15	----
S^{2-}	20 500	-3.5	----
$S_{(c)}$	0	7.6	----
$S_{(l)}$	71	8.2	----
Cu^{2+}	15 660	-23.8	----
Cu^+	11 950	9.7	----
$HCuO_2^-$	-61 800	10	----
CuO_2^{2-}	-43 900	-33	----
$Cu_{(c)}$	0	7.923	5.84
CuO	-31 000	10.19	10.11
Cu_2O	-34 900	22.26	15.21
CuS	-12 800	15.9	11.43
Cu_2S	-20 600	28.9	18.24
$CuSO_4 \cdot 5H_2O$	-449 344	71.8	67
$CuSO_4 \cdot 3H_2O$	-334 650	52.9	49
$CuSO_4 \cdot H_2O$	-219 460	34.9	32
$CuSO_4 \cdot 2Cu(OH)_2$	-345 800	52	64.6
$CuSO_4 \cdot 3Cu(OH)_2$	-434 500	71	84.8
$H_2AsO_4^-$	-180 040	28.0	----
H_3AsO_4	-183 030	44.0	----
Cu_2AsO_4OH	-201 300	36.1[†]	----

[†] Latimer's Method [87]

Table I-A2: Elevated Temperature Heat Capacity and Gibb's Free Energy of Formation Data

Species	$\overline{C_p^o}\vert_{298}^{388}$ (cal/mole K)	$\Delta G^\circ_{f(388)}$ (cal/mole)	$\overline{C_p^o}\vert_{298}^{408}$ (cal/mole K)	$\Delta G^\circ_{f(408)}$ (cal/mole)
H^+	31.65	0	32.32	0
H_2O	18.1	-53 269	18.1	-52 532
HSO_4^-	6.648	-171 340	3.133	-169 246
SO_4^{2-}	-104.772	-165 228	-103.65	-162 235
$H_2S_{(a)}$	41.82	-6126	39.04	-6048
HS^-	-58.97	5531	-60.39	6253
S^{2-}	-58.970	24 422	-60.06	25 314
$S_{(l)}$	6.615	0	6.331	0
Cu^{2+}	64.847	15 674	65.65	15 679
Cu^+	43.1	10 274	43.21	9885
$HCuO_2^-$	-78.123	-54 943	-81.41	-51 945
CuO_2^{2-}	-182.050	-31 275	-178.72	-28 133
$Cu_{(c)}$	5.925	0	5.94	0
CuO	-----	-28 587	-----	-28 148
Cu_2O	-----	-33 712	-----	-33 349
CuS	-----	-12 760	-----	-12 740
Cu_2S	-----	-21 339	-----	-21 470
$CuSO_4 \cdot 3H_2O$	-----	-313 326	-----	-308 789
$CuSO_4 \cdot 2Cu(OH)_2$	65.3	-324 373	65.7	-319 616
$CuSO_4 \cdot 3Cu(OH)_2$	85.3	-406 848	85.7	-400 707
$H_2AsO_4^-$	-7.2	-----	-10.7	-----
H_3AsO_4	36.2	-----	32.6	-----
Cu_2AsO_4OH	43.2	-----	43.5	-----

I-A3: Elevated Heat Capacity Data - $\overline{C_p^o}\big|_{298}^{T}$

I) *Aqueous Ionic Species*

The empirical method of Criss and Cobble [16] was employed:

$$\overline{C_p^o}\Big|_{298}^{T} = \frac{a_T - (S_{298}^o)_{abs}[1.000 - b_T]}{\ln(T/298)}$$

where *a* and *b* are empirical coefficients, and $(S_{298}^o)_{abs} = (S_{298}^o)_{conv} - 5.0Z$, with Z being the sign and magnitude of the charge on the species.

II) *Non-ionic Species*

Elevated heat capacity data for non-ionic (aqueous undissociated species or condensed phases) were determined by one of four methods:

1. Interpolation of values quoted in literature [15].

2. Numerical average of $C_p^o(T)$ function data found in literature according to:

$$\overline{C_p^o}\Big|_{298}^{T} = \frac{1}{(T-298)}\int_{298}^{T} C_p^o(T)\ dT$$

where $C_p^o(T)$ is in the form: $a + bT + cT^{-2} + dT^5$. $C_p^o(T)$ functions were found in Rao [88] and in the HSC data base.

3. Kellogg's Method which assumes that the heat capacity of a multi-component species is approximately equal to the sum of the heat capacities of its component parts.

eg. $Cu_3(AsO_4)_2 + Cu(OH)_2 = 2Cu_2(AsO_4)OH$

Species	$C_p^o(T)$ (cal/(mole K))
$Cu_3(AsO_4)_2$	$66.35 + 1.72 \times 10^{-2}T - 8.68 \times 10^5 T^{-2}$
$Cu(OH)_2$	$20.79 + 5.56 \times 10^{-3}T - 1.29 \times 10^5 T^{-2}$
$Cu_2(AsO_4)OH$	$(87.14 + 2.28 \times 10^{-2}T - 9.97 \times 10^5 T^{-2})/2$

4. Criss and Cobble method [16], assuming species such as H_3AsO_4(aq) have the same a and b coefficients as an acid oxyanionic species such as $H_2AsO_4^-$(aq)

I-A4: Elevated Temperature Free Energy Data

Quoted values of free energies of formation at elevated temperature were obtained by interpolation of literature sources [18] or by employing the following relationship:

$$\Delta G_{f,T}^{o} = \Delta G_{f,298}^{o} + (\overline{\Delta C_p^{o}|_{298}^{T}}) \Delta T - (\Delta S_{298}^{o})_{abs} - T(\overline{\Delta C_p^{o}|_{298}^{T}}) \ln(T/298)$$

The reaction written involved elements in their standard states and charges were balanced with H^+. For antlerite at 115°C (388 K):

$$3Cu + S + 4O_2 + 2H_2 = CuSO_4 \cdot 2Cu(OH)_2$$
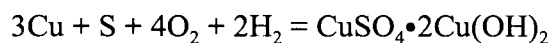
(in cal)	Cu	S	O_2	H_2	H+	$CuSO_4 \cdot 2Cu(OH)_2$	Δ
$\Delta G^{o}_{f\,(298)}$	0	0	0	0	0	-345 800	----
$(S^{o}_{298})_{abs}$	3(7.9)	7.6	4(49.0)	2(31.2)	0	52	-237.9
$\overline{C_p^{o}|_{298}^{T}}$	3(5.9)	6.6	4(7.2)	2(6.9)	0	65.3	-1.5

$\Delta G^{o}_{f\,(388)}(CuSO_4 \cdot 2Cu(OH)_2) = -324\,373$ cal

Appendix I-B   Thermodynamic Analysis for Basic Copper Arsenate Formation

A thermodynamic analysis comparing the precipitation pH values of basic copper arsenate and basic copper sulfate under operating conditions will be presented to determine the relative stability of these two compounds as a function of pH. This will determine whether the BCS catalyzing mechanism of basic copper arsenate substrates that has been proposed is thermodynamically sound. The thermodynamic data used are found above and the analysis is as follows:

1) $HSO_4^- = SO_4^{2-} + H^+$
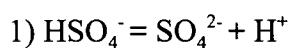
Temp(K)	$\Delta G^\circ_{T(rxn)}$(cal/mole)	a (HSO$_4^-$)	a (SO$_4^{2-}$)	pH
298	2720	1	1	1.99
388	6112	1	1	3.44
408	7011	1	1	3.76

2) $3Cu^{2+} + HSO_4^- + 4H_2O = CuSO_4 \cdot 2Cu(OH)_2 + 5H^+$
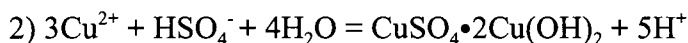
Temp(K)	$\Delta G^\circ_{T(rxn)}$(cal/mole)	a (Cu^{2+})	a (HSO$_4^-$)	pH
298	14 658	1	1	2.15*
		1.24	1.43	2.06*
388	13 023	1	1	1.47
		1.24	1.43	1.38
408	12 723	1	1	1.36
		1.24	1.43	1.28

* Clearly, the reaction should be written with SO_4^{2-} at 298 K as bisulfate is not stable above pH = 2 at this temperature. The equilibrium pH of reaction (2) using sulfate at 298 K is 2.19 and 2.08 for the two different activities.

3) $H_3AsO_4 = H_2AsO_4^- + H^+$
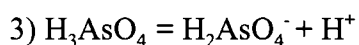
Temp(K)	$\Delta G^\circ_{T(rxn)}$ (cal/mole)	a (H_3AsO_4)	a ($H_2AsO_4^-$)	pH
298	3040	1	1	2.23
388	4627	1	1	2.60
408	5001	1	1	2.68

4) $2Cu^{2+} + H_3AsO_4 + H_2O = Cu_2AsO_4(OH) + 4H^+$
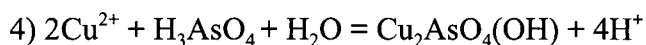
Temp(K)	$\Delta G^\circ_{T(rxn)}$ (cal/mole)	a (Cu^{2+})	a (H_3AsO_4)	pH
298	7147	1	1	1.31
		1.24	0.0394	1.61
		1.24	0.0729	1.55
		1.24	0.106	1.51
388	6731	1	1	0.95
		1.24	0.0394	1.25
		1.24	0.0729	1.19
		1.24	0.106	1.14
408	6380	1	1	0.85
		1.24	0.0394	1.16
		1.24	0.0729	1.09
		1.24	0.106	1.05

The solution composition used in the calculations is taken from the arsenic-in-electrolyte test and is as follows:

- Solution volume = 1L

- $[Cu^{2+}]$ = Based on Grewal's observation that maximum solution copper concentration
  achieved = 79.1 g (@ 5% O_2 consumption)[ ] = 1.24 mol/L

- $[SO_4^{2-}]$ = Based on initial electrolyte composition
  = (1.02 mol H_2SO_4 + 0.315 mol $CuSO_4 \cdot 5H_2O$ + 0.09 mol $FeSO_4 \cdot 7H_2O$)
  = 1.42 mol/L

- •   [As]   = Based on initial electrolyte and feed solids composition(cake#11 - 0.579% As), assuming full extraction at point of basic copper arsenate precipitation.

             = 2.95 g As/74.92 g/mole + electrolyte As concentration

Assumptions:

     Unit activity coefficients

     Unit activities for H_2O and solid species

Appendix I-C Tabulated Results

Table I-C1: Effect of Temperature on Leaching Behaviour

Feed #	Leach Temp. (°C)	Filter Cake Wt.-Dry (g)	Unleached Residue Wt.-Dry (g)	[†] BCS Wt.-Dry (g)	pH(T)	E_h (T) (V_{SHE})	[††] Visc. @4.9 s^{-1}	% Cu Extract.
1	100	523.6	43.8	479.8	2.50	648.0	147	94.1
	115	505.9	11.5	494.4	2.28	740.0	101	99.8
	125	495.3	12.0	483.3	2.32	702.6	30	99.7
	135	494.1	14.8	479.3	2.46	675.7	30	99.3
2	115	424.2	10.9	413.3	2.29	648.0	10	99.4
	135	426.6	16.9	409.7	2.34	621.0	14	98.6
3	100	490.1	47.1	443.0	2.41	646.0	25	93.6
	115	461.5	7.6	453.9	2.33	724.1	12	99.9
	125	464.1	9.5	454.6	2.43	774.1	9	99.8
	135	461.3	9.8	451.5	2.38	742.8	14	99.8
	135	472.6	10.6	462.0	2.24	707.1	18	99.7
4	100	495.1	31.3	463.8	2.26	646.4	21	95.8
	115	475.6	8.2	467.4	2.21	691.9	18	99.6
	115	n/a	n/a	n/a	2.30	642.0	19	99.6
	125	476.6	8.8	467.8	2.19	723.0	40	99.5
	135	473.5	8.9	464.6	2.15	656.0	99	99.5
	135	477.4	13.1	464.3	2.34	604.8	87	98.7
5	100	455.5	58.3	397.2	2.43	644.5	23	93.5
	115	424.1	19.7	404.4	2.29	720.5	9	99.6
	125	428.0	17.8	410.2	2.21	765.8	9	99.5
	135	427.2	17.7	409.5	2.35	691.4	17	99.1
6	100	510.4	51.4	459.0	2.62	640.8	29	93.4
	115	482.3	24.7	457.6	2.48	607.3	19	97.7
	125	481.3	23.4	457.9	2.32	607.8	36	97.8
	135	529.6	93.7	435.9	2.52	593.8	n/a	85.9
	135	506.6	106.5	400.1	2.66	592.0	3500(LV3)	83.2

[†] Weight of BCS includes all acid soluble values down to pH 0.5
[††] Unless otherwise indicated, all quoted viscosities were obtained with the ULA-type spindle

Table I-C2: Effect of Electrolyte Arsenic Level on Leaching of Feed #2

[As] (g/L)	Leach Temp. (°C)	Filter Cake Wt.-Dry (g)	Unleached Residue Wt.-Dry (g)	[†] BCS Wt.-Dry (g)	pH(T)	E_h (T) (V_{SHE})	[††] Visc. @4.9 s^{-1}	% Cu Extract.
+0	115	424.2	10.9	413.3	2.29	648.0	12.3	99.4
+5		440.4	18.8	421.6	2.40	611.3	25.5	98.1
+10		433.8	8.3	425.5	2.48	665.0	41.4	99.8
+0	135	426.6	409.7	16.9	2.34	621.0	19.5	98.6
+5		433.6	413.4	20.2	2.44	614.3	850(LV3)	97.8
+10		473.0	334.2	138.8	2.65	602.1	1500(LV3)	76.6

[†] Weight of BCS includes all acid soluble values down to pH 0.5
[††] Unless otherwise indicated, all quoted viscosities were obtained with the ULA-type spindle

Table I-C3: CRED Plant CRMT# Equivalents to Feed Code# used in Study

Feed #	CRMT #	Feed #	CRMT #
1	3003	4	2399
2	11	5	3017
3	1107	6	3090

CRMT #(Copper-Residue-Mix-Tank Number)

Appendix I-D   X-Ray Diffraction Data: Selective pH Leach Residue
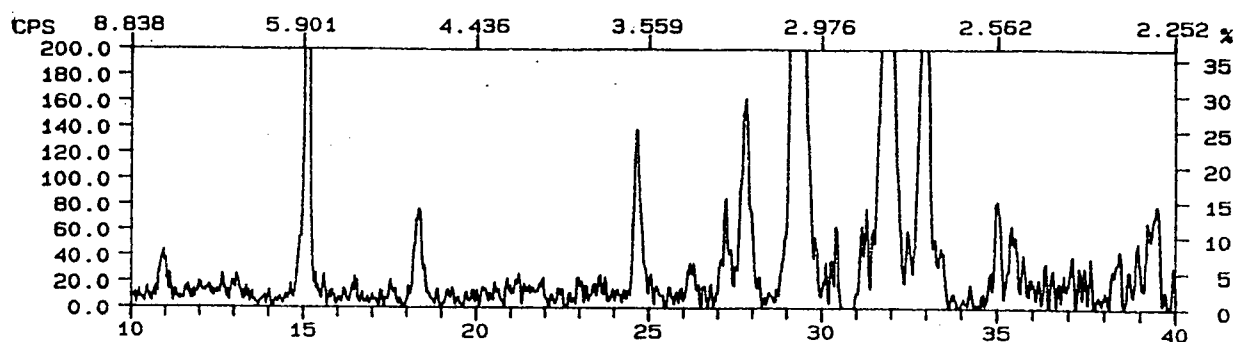
Figure I-D1   X-Ray diffraction pattern of pH 1.86 residue

COPPER SULFIDE / COVELLITE. SYN

06-0464

CU S
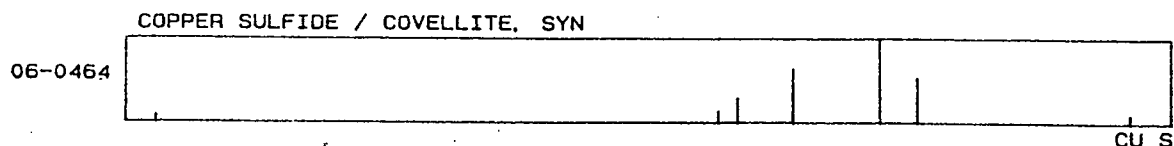
Figure I-D2   X-Ray diffraction of Covellite - CuS

COPPER SULFATE HYDROXIDE / ANTLERITE. SYN

07-0407
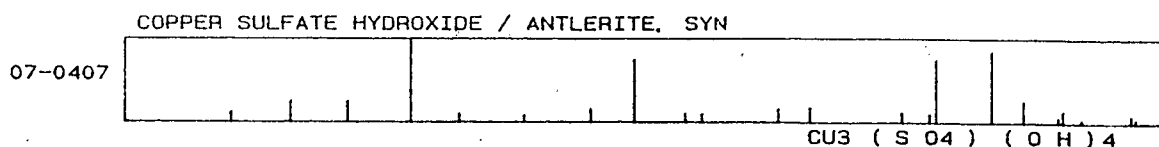
CU3 (S O4) (O H)4

Figure I-D3   X-Ray diffraction of Antlerite - $CuSO_4 \cdot 2Cu(OH)_2$

LEAD COPPER IRON SULFATE HYDROXIDE / BEAVERITE

17-0476
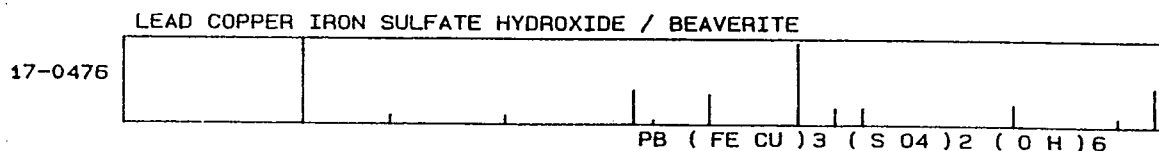
PB (FE CU)3 (S O4)2 (O H)6

Figure I-D4   X-Ray diffraction of Beaverite - $Pb[Fe,Cu]_3(SO_4)_2(OH)_6$

LEAD IRON ARSENATE SULFATE HYDROXIDE / BEUDANTITE

19-0689
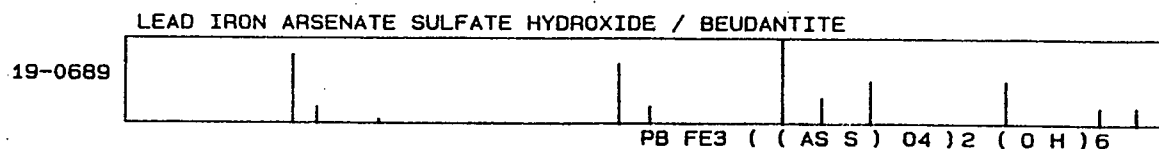
PB FE3 ((AS S) O4)2 (O H)6

Figure I-D5   X-Ray diffraction of Beudantite - $PbFe_3([As,S]O_4)_2(OH)_6$

COPPER ARSENATE HYDROXIDE / OLIVENITE

42-1353
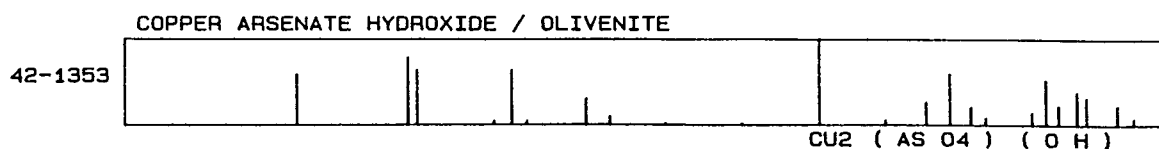
CU2 (AS O4) (O H)

Figure I-D6   X-Ray diffraction of Olivinite - $Cu_2(AsO_4)(OH)$

Compound	Chemical Formula	Crystal System	U.C. Dimen. $(a / b / c)$ [Å]	3 Strongest Peaks (dÅ/I)	PDF #
Antlerite (BCS)	$Cu_3SO_4(OH)_4$	Orthorh.	8.25 12.01 6.04	4.86/100 2.57/85 2.68/75	7-407
Olivinite (BCAs)	$Cu_2AsO_4(OH)$	Orthorh.	8.22 8.64 5.95	2.98/100 4.82/90 5.91/70	4-657
Scorodite	$FeAsO_4 \cdot 2H_2O$	Orthorh.	8.95 10.33 10.04	4.47/100 3.18/90 5.61/80	37-468
Beudantite	$PbFe_3[(As,S)O_4]_2(OH)_6$	Hexag.	7.32 ----- 17.02	3.08/100 5.99/80 3.67/70	19-689
Beaverite	$Pb(Fe,Cu)_3(SO_4)_2(OH)_6$	Hexag.	5.85 ----- 16.94	5.85/100 3.03/100 2.28/50	17-476
Chalcocite	Cu_2S	Monocl.	15.24 11.88 13.50	1.88/100 2.40/70 1.97/70	32-490
Djurleite	$Cu_{1.96}S$	Tetrag.	4.00 ----- 11.29	2.47/100 2.30/80 1.88/40	29-578
Digenite	$Cu_{1.8}S$	Hexag.	3.92 ----- 48.8	1.97/100 2.78/50 3.21/40	23-962
Covellite	CuS	Hexag.	3.79 ----- 16.34	2.81/100 1.90/80 3.05/70	6-464

APPENDIX I-F   Physical Characteristics of Crystals

Crystals by definition are characterized by three dimensional periodicity of which the unit cell is the smallest repeating unit.   Unit cells are categorized into 7 separate systems based on their axial and dimensional symmetry.   These are shown below.

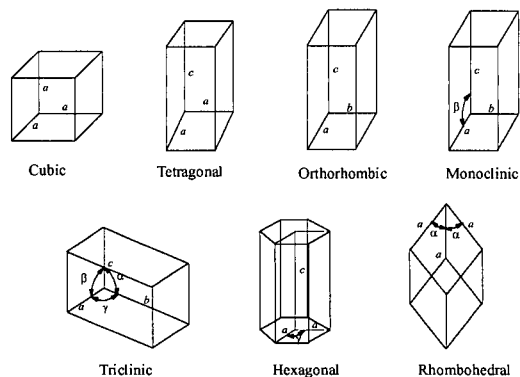| System	Axes	Axial Angles
Cubic	$a = b = c$	$\alpha = \beta = \gamma = 90°$
Tetragonal	$a = b \neq c$	$\alpha = \beta = \gamma = 90°$
Orthorhombic	$a \neq b \neq c$	$\alpha = \beta = \gamma = 90°$
Monoclinic	$a \neq b \neq c$	$\alpha = \gamma = 90° \neq \beta$
Triclinic	$a \neq b \neq c$	$\alpha \neq \beta \neq \gamma \neq 90°$
Hexagonal	$a = a \neq c$	$\alpha = \beta = 90°$; $\gamma = 120°$
Rhombohedral	$a = b = c$	$\alpha = \beta = \gamma \neq 90°$

Figure I-F1   Crystal Systems [19].

APPENDIX II - A   SUMMARY OF GAS-LIQUID MASS TRANSFER RESULTS

CONDITIONS	IMPELLER SYSTEM	N (RPM)	% O2 GAS	T (C)	C* (ppm)	RO2 (T) (mol O2/m3/sec)	K1A (1/sec)	RO2 (25 C) (mol O2/m3/sec)	Pavg (W)	Mol/Energy (25 C) (mol/J x 10e-3)
1) COOLING COILS - EFFECT OF RPM	AD	121	93.9	22.5	31.9	0.005	0.005	0.005	17.9	0.034
		171	92.4	27.3	28.8	0.147	0.164	0.166	53.2	0.390
		221	89.3	28.0	27.5	0.236	0.275	0.279	114.6	0.304
		221	89.5	28.2	27.5	0.254	0.295	0.300	113.8	0.329
		221	88.8	28.5	27.1	0.267	0.315	0.320	113.1	0.353
		221	89.5	31.4	26.0	0.246	0.303	0.307	114.5	0.336
		221 (avg)	89.6	28.5	27.3		0.297	0.301	114.0	0.331
		271				0.370	0.434	0.440	193.8	0.284
	RR	121	92.7	27.8	28.7	0.081	0.091	0.092	54.4	0.212
		171	93.0	26.1	29.6	0.221	0.239	0.242	133.1	0.228
		221	93.6	25.5	30.1	0.371	0.394	0.400	277.4	0.180
		221	86.7	28.3	26.6	0.336	0.404	0.410	277.7	0.185
		221	89.1	25.0	28.9	0.386	0.427	0.433	284.1	0.190
		221 (avg)	85.8	26.5	27.1		0.408	0.414	279.7	0.185
		271				0.413	0.487	0.494	493.1	0.125
	RA	121	94.3	24.9	30.7	0.096	0.100	0.102	33.5	0.380
		171	93.8	27.5	29.1	0.253	0.278	0.282	74.1	0.475
		221	93.3	27.5	29.0	0.409	0.452	0.459	139.9	0.410
		221	85.9	29.3	25.9	0.374	0.462	0.469	144.6	0.405
		221	87.7	26.5	27.7	0.428	0.494	0.502	143.5	0.437
		221 (avg)	84.3	28.5	25.7		0.470	0.476	142.7	0.417
		246				0.442	0.550	0.558	191.7	0.364

CONDITIONS	IMPELLER SYSTEM	FILL HT. (%)	% O2 GAS	T (C)	C* (ppm)	RO2 (T) (mol O2/m3/sec)	K1A (1/sec)	RO2 (25 C) (mol O2/m3/sec)	Pavg (W)	Mol/Energy (25 C) (mol/J x 10e-3)
2) COOLING COILS - FILL HEIGHT - @ 221 RPM	AD	-10%	92.8	25.5	29.9	0.129	0.138	0.140	89.9	0.173
		-5%	92.2	25.0	29.9	0.299	0.319	0.324	109.5	0.349
		+5%	95.8	23.5	32.0	0.062	0.062	0.063	137.4	0.061
		+10%	94.2	23.5	31.4	0.047	0.048	0.048	143.0	0.047
	RR	-10%	82.5	25.0	26.8	0.268	0.320	0.324	248.9	0.144
		-5%	85.3	25.8	27.3	0.368	0.431	0.438	270.5	0.179
		+5%	87.5	28.5	26.7	0.334	0.400	0.406	292.6	0.154
		+10%	89.2	28.5	27.2	0.196	0.230	0.234	336.5	0.077
	RA	-10%	94.2	27.3	29.4	0.294	0.321	0.325	108.3	0.333
		-5%	84.2	27.0	26.4	0.413	0.501	0.508	130.3	0.432
		+5%	85.8	25.8	27.5	0.396	0.461	0.468	175.3	0.296
		+10%	91.5	27.0	28.7	0.228	0.255	0.258	235.8	0.122

APPENDIX II - A   SUMMARY OF GAS-LIQUID MASS TRANSFER RESULTS (...CONT)

CONDITIONS	IMPELLER SYSTEM	N (RPM)	% O2 GAS	T (C)	C* (ppm)	RO2 (T) (mol O2/m3/sec)	KIA (1/sec)	RO2 (25 C) (mol O2/m3/sec)	Pavg (W)	Mol/Energy (25 C) (mol/J x 10e-3)
3) UNBAFFLED - EFFECT OF RPM	AD	121	94.1	24.0	31.1	0.011	0.011	0.011	5.2	0.275
		171	91.4	28.8	27.8	0.021	0.025	0.025	16.9	0.186
		221	94.2	25.8	30.2	0.040	0.043	0.044	43.7	0.125
		271	93.5	28.5	28.5	0.086	0.096	0.098	71.4	0.171
	RR	121	93.6	23.0	31.5	0.012	0.012	0.012	14.7	0.106
		171	93.4	27.5	29.0	0.020	0.022	0.022	34.7	0.079
		221	92.8	24.8	30.3	0.053	0.056	0.057	76.8	0.093
		271	92.7	29.5	27.8	0.143	0.165	0.167	143.8	0.145
	RA	121	93.2	24.3	30.7	0.015	0.016	0.016	8.9	0.226
		171	92.5	31.0	27.0	0.042	0.050	0.050	23.8	0.265
		221	93.6	25.8	30.0	0.106	0.113	0.115	49.6	0.289
		246	93.5	24.8	30.5	0.136	0.143	0.145	66.0	0.274
		271	93.8	26.8	29.5	0.162	0.175	0.178	86.0	0.259

CONDITIONS	IMPELLER SYSTEM	N (RPM)	% O2 GAS	T (C)	C* (ppm)	RO2 (T) (mol O2/m3/sec)	KIA (1/sec)	RO2 (25 C) (mol O2/m3/sec)	Pavg (W)	Mol/Energy (25 C) (mol/J x 10e-3)
4) 4-BAFFLED - EFFECT OF RPM	AD	121	93.8	24.8	30.6	0.029	0.030	0.031	23.7	0.162
		171	91.7	26.1	29.2	0.123	0.135	0.137	66.9	0.256
		221	92.2	30.8	27.0	0.190	0.225	0.229	133.2	0.215
		271	91.3	30.3	27.0	0.290	0.343	0.348	237.5	0.183
	RR	121	93.3	26.8	29.4	0.098	0.107	0.108	70.5	0.192
		171	90.3	26.5	28.5	0.250	0.280	0.284	174.8	0.203
		221	89.8	27.0	28.1	0.360	0.409	0.415	428.2	0.121
		271	87.6	25.8	28.1	0.422	0.481	0.488	754.3	0.081
	RA	121	94.2	28.3	28.9	0.104	0.115	0.117	39.4	0.371
		171	82.2	29.3	24.7	0.250	0.323	0.328	98.2	0.417
		221	90.1	26.3	28.6	0.249	0.279	0.283	297.7	0.119
		246	89.2	26.8	28.1	0.325	0.370	0.376	414.2	0.113
		271	92.1	27.3	28.7	0.417	0.464	0.471	513.1	0.115